國立彰化師範大學物理研究所

碩士論文

指導教授：郭艷光博士

# 紫藍光氮化銦鎵量子井雷射之模擬與分析

# Simulation of Violet-Blue InGaN Quantum-Well Lasers

研究生：張詒安撰

中華民國九十二年六月

國立彰化師範大學物理研究所

碩士論文

研究生：張詒安

# 紫藍光氮化銦鎵量子井雷射之模擬與分析

# Simulation of Violet-Blue InGaN Quantum-Well Lasers

本論文業經審查及口試合格特此證明

論文考試委員會主席：_____

委員：_____ _____ _____

指導教授：郭艷光教授_____

所長：徐力行主任_____

中華民國九十二年六月

# 博碩士論文電子檔案上網授權書

(提供授權人裝釘於紙本論文書名頁之次頁用)

本授權書所授權之論文為授權人在彰化師範大學物理系 91 學年度第二學期取得碩士學位之論文。

**論文題目：紫藍光氮化銦鎵量子井雷射之模擬與分析**
**指導教授：郭艷光**

茲同意將授權人擁有著作權之上列論文全文（含摘要），非專屬、無償授權國家圖書館及本人畢業學校圖書館，不限地域、時間與次數，以微縮、光碟或其他各種數位化方式將上列論文重製，並得將數位化之上列論文及論文電子檔以上載網路方式，提供讀者基於個人非營利性質之線上檢索、閱覽、下載或列印。

讀者基於非營利性質之線上檢索、閱覽、下載或列印上列論文，應依著作權法相關規定辦理。

**授權人：張詒安**

**簽名：_____** 中 華 民 國 92 年 7 月 4 日

To my father, my mother, my family members,

my girlfriend and her family members, and all my dear friends.

## Acknowledgment

I would like to offer my sincere appreciation to my academic advisor, Professor Yen-Kuang Kuo, whom is friendly and easy to get along with. From his guidance, I have received much knowledge and experience in professional optoelectronics, and even in my graduate student's daily life. He always tells us that a man must be responsible for himself, honest and try his best in doing anything, just like he demands himself. By the way, he is also an expert and a good partner in playing volleyball and basketball, and we always play with fun.

Besides, I would like to thank Dr. Bo-Ting Liou for being the chairman of my thesis committee, and Professors Man-Fang Huang and Yu-Tai Shih for serving in my thesis committee. Especially, I am deeply grateful to my parents and all my family members for loving and caring me from childhood. I also would like to express my heartfelt gratitude to my girlfriend, Jessica Tsai and her parents, who help me go through all the difficulties and take care of my life in Changhau. I really wish to share this achievement with them.

Finally, I would like to thanks my dear friends, Jih-Yuan Chang, Wen-Wai Lin, Yuni Chang, Chih-Kang Chang, Sheng-Horng Yen, Yu-Hua Wu, Cheng-Yang Lin, Tsai-meng-lun, Han-Yi Chu, Shang-Wei Hsieh, Sheng-Joue Young, Pei-Hsuan Wu, Hsiu-Fen Chen, Man-Lin Tu, and other

members in our laboratory. Without them, I really don't know what I can do.

A drama shall need a protagonist. I am the protagonist in the drama of my graduate student's life. Everyone who lives surround me is the director. Some of them encourage me to look at the bright side of the occurrences. Others guide me to act perfectly. Thanks for everyone I ever met in Changhua. These will be put in my deep mind forever.

**~ I can't see exactly what will happen in the future, but I can learn in everyday ~**

**~ Yi-An Chang, 2003 ~**

**Table of Contents**

## List of Figures

## List of Tables

# 中文摘要

本文以理論模擬方式探討紫藍光氮化銦鎵量子井半導體雷射量子井個數最佳設計分析以得到較小之臨界電流值，以及對 405-nm 氮化銦鎵雙量子井雷射之電子溢流與雷射特性做一分析探討。模擬過程中，主要利用加拿大 Crosslight 公司所提供之 LASTIP 商用模擬軟體來得到以三五族氮化物為材料所成長之側射型半導體雷射的各項光電特性與雷射性能。在文章一開始，首先對三五族氮化物半導體材料發展歷史做一簡短回顧，以及對此一材料之相關重要參數如能帶間隙、能隙補償差值、以及折射率等做一總整。

S. Nakamura 等人於實驗上發現當量子井個數設計為兩個時，發光波長在 390 nm 與 420 nm 間之氮化銦鎵量子井雷射可以有最低的臨界電流值，而當波長在 435 nm 以上時，卻以單量子井雷射有最低之臨界電流值；他們認為要得到較長發光波長之氮化銦鎵量子井雷射，量子井之銦含量勢必要提高，然而較高之銦含量往往導致成長第二層以上之量子井時，產生晶格錯位而造成晶體缺陷，因此發光波長越長時以設計單量子井為最佳。基於此一構想，於文章主體部分首先分析在期望得到較小臨界電流值的情況下，發光波長在 396.1 nm 至 479.3 nm 間紫藍光氮化銦鎵量子井雷射之量子井個數的最佳設計與分析。由模擬結果得知，當波長越長時確實以單量子井雷射有最低之臨界電流值，

其主要原因在於價電帶之能隙補償差值較大且電洞有效質量較大而影響其移動速率，因而造成活性區域中電洞不均勻分布於量子井中。然而當發光波長趨向於較短波長時，量子井旁之井障的銦濃度以及氮化銦鎵量子井的厚度決定了量子井個數的最佳設計。另外由模擬結果亦發現，發光波長為 415.7 nm 或 436.9 nm 之氮化銦鎵單量子井與雙量子井雷射有相同之最佳雷射輸出效能。

隨著下一代高密度儲存容量之光資訊儲存系統即將問世，以發光波長在 400 nm 至 410 nm 間高性能的半導體雷射做為雷射讀取頭逐漸受到重視，尤其以波長為 405 nm 之半導體雷射更是許多學者研究的方針。因此在本文章主體的另一部份將針對 405-nm 氮化銦鎵雙量子井雷射之電子溢流與雷射特性做結構設計上的改善與探討。模擬結果發現當厚度為 20 奈米之氮化鋁鎵電子溢流阻礙層中鋁濃度為 16%時，大部分的電子已被有效地侷限在活性區域中而幾乎無電子溢流產生；相對地雷射效能也在此時達到最佳，而當元件寬度縮短為 2 μm 時可以得到類似單模的高功率 405-nm 氮化銦鎵半導體雷射。

## Abstract

In this thesis, the optimization design of the number of InGaN well layers in violet-blue InGaN/InGaN laser diodes for obtaining lowest threshold current is studied. Moreover, the electronic current overflow and laser characteristics of a 405-nm InGaN laser diode are discussed. The LASTIP simulation program purchased from the Crosslight Incorporation is used to do the simulation of III-nitride based edge-emitting laser diodes and to obtain the laser performance in optical and electrical characteristics. First of all, the development of III-nitride semiconductor materials, and some important parameters such as bandgap energy, band-offset ratio, refractive index, and so on of III-nitride materials are investigated and summarized.

For the main portion of this thesis, the optimization study of III-nitride laser diodes with emission wavelength from 396.1 nm to 479.3 nm as a function of the number of InGaN well layers for obtaining lowest threshold current density is discussed. This idea is inspired by the experimental results demonstrated by Nakamura *et al.* that when the emission wavelength of InGaN laser diodes is in a range from 390 nm to 420 nm, the lowest threshold current density can be obtained when the number of well layers is two. When the emission wavelength is increased beyond 435 nm, the lowest threshold current density can be obtained when the number of well layers is one. Nakamura *et al.* believed that the reason was due mainly

to the first InGaN well layer could be dissociated during the growth of the second or the third well layer, and the internal loss was increased due to poor crystal quality. Numerical simulation results suggest that when the emission wavelength is increased, the lowest threshold current can generally be obtained when the number of InGaN well layer is one. Nevertheless, when the emission wavelength is decreased, the optimization design of the number of InGaN well layers for obtaining lowest threshold current is associated with the indium composition in InGaN barriers and the thickness of InGaN well layers. In addition to the dissociation of InGaN well layers at a high growth temperature during crystal growth, the cause of the above phenomenon is attributed to the relatively high valence band-offset and the large hole effective mass that the holes in the valence band are difficult to transport to the n-side active layers. Specifically, when the emission wavelengths are 415.7 nm or 436.9 nm, single-quantum-well and double-quantum-well laser diodes have similar laser performances.

Recently, remarkable progress has been made in the development of violet-blue LDs with an emission wavelength 400 – 410 nm. The 405-nm LDs receive most attention for the application in the optical storage system. Thus, the electronic current overflow and laser characteristics of a 405-nm double-quantum-well laser diode is studied in another main portion of this thesis. It is observed that most electrons can be confined in quantum well layers effectively and good laser performance can be obtained when the Al composition in AlGaN blocking layer is equal to 16%.

# Chapter 1. Introduction

In the past few years, several significant evolvements had occurred in our daily life. Among these, the largest transformation is that the traditional light sources such as bulbs, lamps, and so on are going to be replaced by new technical products – laser diodes (LDs) and light-emitting diodes (LEDs), covering the entire range of emission wavelengths to which the human eye is sensitive. Moreover, LDs and LEDs can emit ultraviolet and infrared wavelength of the optical spectrum. LDs are fascinating due to their coherency and small divergent angle that make them become unique light sources for optical storage system, fiber communications, etc. LEDs can provide sufficient brightness, which is even higher than the traditional light sources, and the electric consumption is also relatively small due to their high output efficiency. It is favorable for full-color displays and especially for traffic lights to reduce energy consumption.

Laser action in semiconductors was demonstrated in 1962 by several groups [1]-[5]. A forward-biased gallium arsenide (GaAs) p-n junction was performed and the optical gain was provided by the recombination of electrons and holes in the depletion region of the p-n junction. The polished facets perpendicular to the junction plane forming a resonant cavity provided the optical feedback. Several direct-bandgap materials such as indium arsenide (InAs), indium phosphide (InP), gallium arsenide phosphide (GaAsP), gallium indium arsenide (GaInAs), and indium

arsenide phosphide (InAsP) were also used to obtain p-n semiconductor lasers for the purpose of obtaining various emission wavelengths. A schematic p-n junction (homostructure) semiconductor laser is shown in Fig. 1.1(a). However, these earlier devices exhibited a very high threshold current density ($J_{th} \geq 50$ kA/cm$^2$). To reduce the threshold current density, the p-n junction semiconductor lasers were converted to heterostructure lasers, which consist of a layer of one material sandwiched between two cladding layers of another wider bandgap material. Heterostructure lasers can be further categorized as single-heterostructure or double-heterostructure devices, depending on whether the active region is surrounded on one or both sides by a higher bandgap cladding layer.

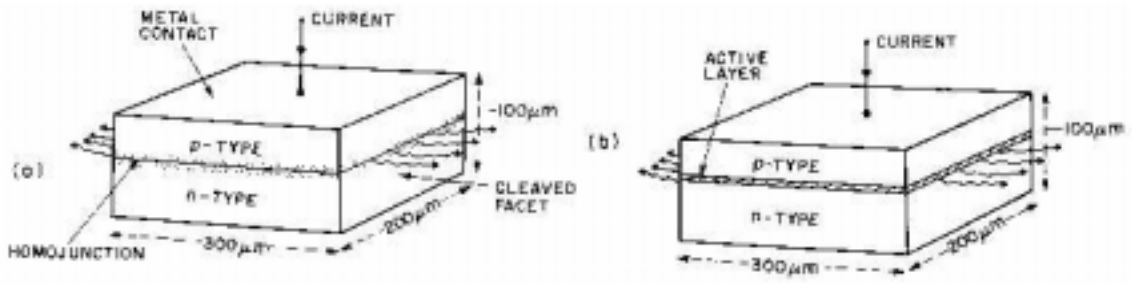


Fig. 1.1. Schematic illustration of (a) p-n junction, and (b) heterostructure lasers with their typical physical dimensions. (After Ref. 1)

A schematic heterostructure laser is shown in Fig. 1.1(b). The first room-temperature operation of a heterostructure laser ($GaAs/Al_xGa_{1-x}As$) was demonstrated by Kressel [6], Hayashi [7], Alferov [8], etc. with the technique of liquid-phase epitaxial (LPE) in 1969. However, these lasers

could only operate in pulse mode, due to device heating. By 1975 the threshold current density was reduced by using 0.1 μm thin active layers to two orders of magnitude over the first-made simple homostructure lasers in 1962. These efforts made the semiconductor laser to become a useful, practical, compact, coherent light source. Notice that the emission wavelength of early GaAs lasers usually operated in the wavelength range 0.8–0.9 μm. Long wavelength semiconductor lasers operating at the wavelengths of 1.31 and 1.55 μm are especially fascinating in optical fiber communication. Quaternary aluminum gallium indium phosphide (InGaAsP) alloys turned out to be the most suitable material on the basis of lattice matching to InP substrate. Room-temperature (RT) operation InGaAsP semiconductor lasers for the requirement of commercialization were demonstrated in 1980s [9]-[12].

The search for semiconductor materials emitting in the visible region of the spectrum can be traced in the early 1960s as well. On that time, the well-developed group IV elemental semiconductors germanium (Ge) and silicon (Si) had been expected, but unfortunately they were unsuitable due to that their small bandgap energies could only create infrared (IR) photons and their bandgap type are indirect. Therefore, semiconductor lasers made by these materials always had poor conversion efficiency [13], [14]. For this reason, several researchers turned to study group III-V and II-VI compound semiconductor materials. Some properties for several common semiconductor materials are listed in Table 1.1 [15]. The bandgap energy of

gallium phosphide (GaP) is 2.26 eV, which can provide green photons for visible LEDs, and several direct-bandgap III-V compound semiconductors like indium antimonide (InSb), InAs, InP, GaAs, etc. can be the materials as well. However, the band structure of GaP is still indirect, and the bulk growth techniques for semiconductor materials are also in their early stage. Therefore, there were no efficient LEDs can be found at that time.

Table 1.1. Properties of common semiconductor materials.

| Material | Bandgap (eV) | $\varepsilon_r$ | $\mu_e$ ($cm^2$/V-sec) | $\mu_h$ ($cm^2$/V-sec) | $m_e^*/m_0$ | Lattice (Å) |
|---|---|---|---|---|---|---|
| C(i) | 5.47 | 5.7 | 1800 | 1200 | 0.2 | 3.5668 |
| GaP(i) | 2.26 | 11.1 | 1600 | 100 | 0.82 | 5.4512 |
| AlAs(i) | 2.16 | 10.9 | 180 | — | — | 5.6605 |
| GaAs(d) | 1.43 | 13.2 | 8500 | 400 | 0.067 | 5.6533 |
| InP(d) | 1.35 | 12.4 | 4600 | 150 | 0.077 | 5.8686 |
| Si(i) | 1.12 | 11.9 | 1500 | 450 | 1.1 | 5.4309 |
| GaSb(d) | 0.72 | 15.7 | 5000 | 850 | 0.042 | 6.0957 |
| InAs(d) | 0.36 | 14.6 | 33,000 | 460 | 0.023 | 6.0584 |
| InSb(d) | 0.17 | 17.7 | 80,000 | 1250 | 0.0145 | 6.4794 |

The first visible LEDs were red LEDs made of direct-bandgap GaAsP materials; however, its lattice constant differs from that of GaAs substrate appreciably, resulting in very high defect densities. As indicated above, it can be found that red, yellow, orange LEDs can be achieved by the combination of GaAs with AlAs as AlGaAs ternary alloys. Even though the bandgap type of AlGaAs semiconductor switches from direct to indirect when the AlAs composition is beyond about 0.45, which prevents the

AlGaAs materials from being used to make efficient orange and yellow LEDs, highly efficient red LEDs can be fabricated with these materials. It is noteworthy that, quaternary AlGaInP alloy is an important material for visible LEDs. When grown on GaAs substrate, the lattice matched $(Al_xGa_{1-x})_{0.5}In_{0.5}P$ alloy has a direct bandgap energy from 1.9 to 2.26 eV, corresponding to the emission wavelength from red to green wavelength of the visible spectrum. However, this material cannot be grown by conventional growth technique such as LPE and hydride vapor-phase epitaxy (VPE), until the processes of organometallic vapor-phase epitaxy (OMVPE or MOCVD) and molecular beam epitaxy (MBE) growth techniques had been well controlled in the late 1980s. Significant advances in the performance of LEDs have been demonstrated with the emission wavelength from 560 to 680 nm by AlGaInP materials as well [13].

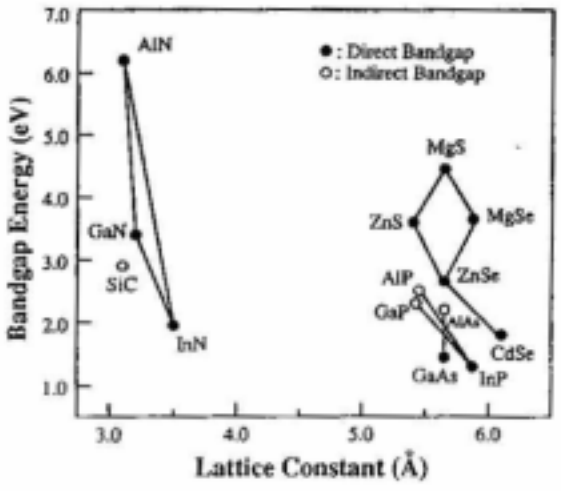


Fig. 1.2. Bandgap energies of different semiconductor materials as a function of lattice constants. (After Ref. 13)

Early works suggest that the red, orange, yellow LEDs have been successfully demonstrated and available for commercialization. However, the development of blue LEDs was still lagging far behind until the middle 1990s. As indicated in Fig. 1.2, silicon carbide (SiC), zinc selinide (ZnSe), and gallium nitride (GaN) can be the materials of blue LEDs. In the history of blue LEDs, the first commercialized blue LEDs are made up by SiC alloys although its bandgap type is indirect, contrary to the direct-bandgap type of ZnSe and GaN materials. The binary alloy of ZnSe belongs to the II-VI group materials and the blue LEDs made up by such material exist high distrustful reliability due to their low operation lifetime. The research of III-nitride materials for the same purpose of obtaining high efficient blue LEDs was still on their step simultaneously [13].

In the history of III-nitride materials, GaN binary alloy was first synthesized by Juza and Hahn by passing ammonia over hot gallium, and produced small needles and platelets for the purpose of studying its crystal structure and lattice constant. In 1958, small crystals of GaN were produced with the same technique by Grimmeiss and Koelmans to measure their photoluminescence (PL) spectra. After ten years, a large layer of GaN grown on sapphire ($Al_2O_3$) substrate by using chemical vapor deposition technique was demonstrated by Maruska and Tietjen [16]. Even the sapphire can be the substrate for growing III-nitride materials, the noticeable lattice mismatch between sapphire and III-nitride alloys, which results in the poor crystal quality, obstructs the development of III-nitride

LEDs.

Major purposes of wide-bandgap III-V semiconductor materials have evolved into the commercial production of high performance LEDs and LDs for printing, communications, full-color displays and sensors. RT continuous-wave (CW) operation and long operation lifetime of LEDs and LDs are required for commercialized availability. As red, orange, yellow LEDs have been commercialized for several years, blue and green LEDs are still in the early stage of finding suitable, reliable materials. Until about ten years ago, III-nitride blue and green LEDs had been demonstrated successfully. Gradually, this material system has become the unique choice in the development of high-brightness violet, blue, green LEDs and high-performance violet-blue LDs.

In the following subsections, a historical review of the development of III-nitride LEDs and LDs, and some important parameters such as bandgap energies, band-offset ratios, refractive indexes and so on of III-nitride alloys are mentioned and summaried.

## 1.1 Introduction to Nitride Based Materials

The bandgap energies of III-nitride materials, indium nitride (InN), GaN, and aluminum nitride (AlN) are 1.89 eV, 3.50 eV, and 6.28 eV, respectively [13]. The bandgap types of these wurtzite alloys are direct. Theoretically, when GaN is alloyed with InN and AlN, the III-nitrides can provide a wide continuous emission wavelength of the spectrum, covering a wide region from near ultraviolet (UV) to red by tuning the material composition in these alloys. The III-nitride compounds have received great attention from several research groups since a couple of decades ago. One of the reasons may be that these optoelectronic devices such as LEDs and LDs not only are capable of making full color display, high density optical storage technologies (>20 Gb) come true, but also reduce the consumption of about 10-20% of power energy. Notably, although red (650 nm) and yellow emitters based on AlGaInP material had been demonstrated successfully [17]-[23], and 630/650-nm LDs have been commercialized for digital versatile disk (DVD) systems, the shortest wavelength available from this material system is restricted to about 560 nm. In spite of II-VI semiconductor material like ZnSe based lasers are capable of emitting green and blue wavelengths of the spectrum, these laser diodes widespreadly exist disappointed operation lifetime. They indirectly enhance III-nitride material system to act unique emitters on violet, blue, green wavelengths of the spectrum undoubtedly. However, several

bottlenecks in the growth techniques of growing III-nitride materials such as poor crystalline quality, lattice mismatch substrate, and low-resistivity p-type doping claddings still need to be broken through.

The research of III-nitride semiconductor materials has been continued for a couple of decades. The earliest difficulty for growing nitride compounds is the lack of lattice-matched substrate. As a result, the crystalline quality was poor at early stage. This problem was not solved until 1983 when Dr. Yoshida improved the crystal quality of GaN films with the use of AlN-coated sapphire ($Al_2O_3$) substrate [23]. Later, high-quality optically flat surfaces of GaN thin films had been successfully grown by using AlN buffer layer with OMVPE technique by Prof. Akasaki *et. al.* [24]. In 1991, S. Nakamura changed AlN thin films with low-temperature growing amorphous GaN thin films as buffer layer, and mirror-flat GaN thin films were obtained under high-temperature growing [25].

At present, sapphire has become the most commonly used substrate for the growth of III-nitride materials. This substrate has several advantages such as high hardness, high heat-resistance, and free of absorption for green and blue photons. Most importantly, it is cheap! However, despite these advantages, there are still some disadvantages; e.g., the interface between GaN and sapphire substrate exists a large lattice mismatch of 15% [26], [27], resulting in a very high dislocation density. Besides, sapphire is a dielectric material, so that both n and p contacts shall be on top of the

devices, and etching techniques are inevitably required.

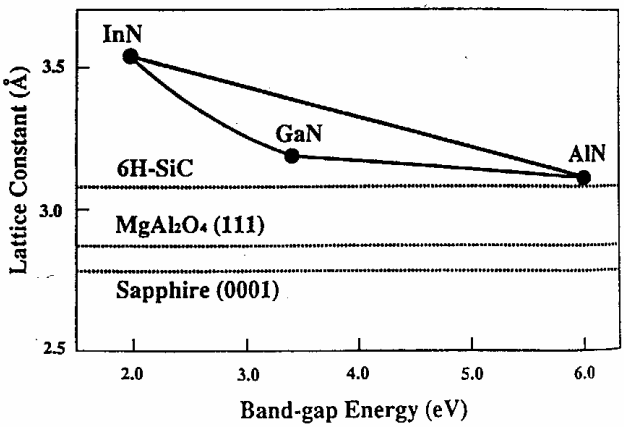


Fig. 1.3. Lattice constant of III-nitride materials as a function of their bandgap energy. (After Ref. 16)

As indicated in Fig. 1.3, GaN can be grown on alternative substrates such as 6H-SiC, which has only 3.5% lattice mismatch with GaN [16]. It is undoubted that better lattice match can apparently reduce the dislocation density [28], [29]. Another important extra advantages are that this material has high conductive property, and its thermal expansion coefficient is close to that of GaN. The 6H-SiC can be doped as either n-type or p-type substrate to make it conducting. This will simplify the device structure. However, the cost of 6H-SiC is much more expensive than that of sapphire. Other substrate such as spinel ($MgAl_2O_4$) can also be the substrate for the growth of III-nitride materials; however, the lattice mismatch between spinel and GaN is 9.5%, which is larger than that between 6H-SiC and GaN. Besides, the cost of this substrate material is still too expensive for commercial applications.

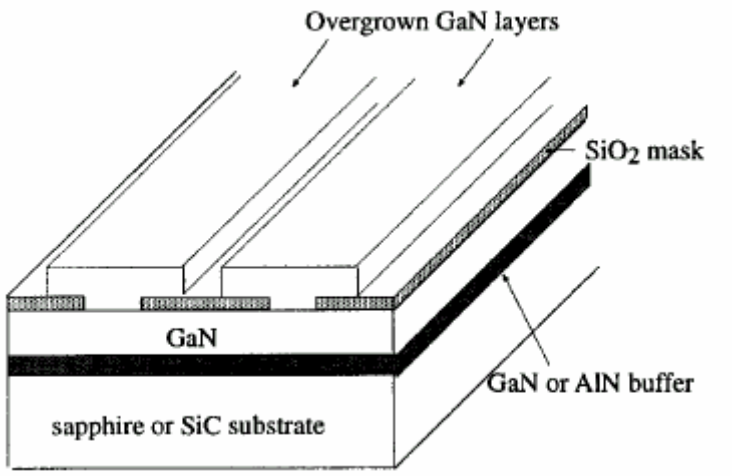


Fig. 1.4. Schematic plot of ELOG substrate.

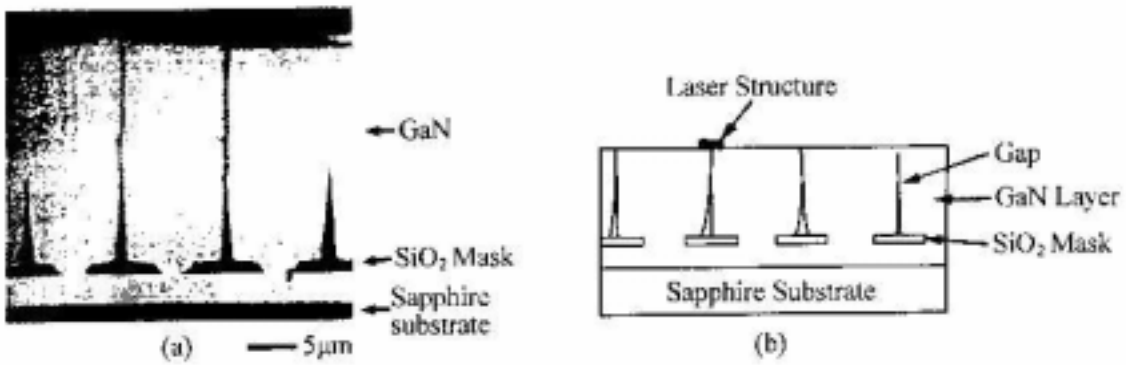


Fig. 1.5. (a) Cross section of the device fabricated on the ELOG substrate, and (b) is the schematic of (a). (After Ref. 31)

To reduce the dislocation density, epitaxially lateral overgrown GaN (ELOG) substrate was developed [30]. Figure 1.4 shows a schematic plot of ELOG substrate. The selective growth of GaN is performed on a 2-μm-thick GaN layer grown on sapphire or SiC substrates. The 1-μm-thick silicon dioxide ($SiO_2$) mask is patterned to form 5-μm-wide

stripe windows with a periodicity of 10 μm. After 10-μm-thick GaN was grown on the $SiO_2$ mask pattern, the coalescence of the selectively grown GaN made it possible to obtain a flat GaN surface over the entire substrate.

As shown in Fig. 1.5, the number of threading dislocations was reduced in the GaN grown on a $SiO_2$ stripe [31]. The threading dislocation density can be reduced to about $2\times10^7$ $cm^{-2}$ in the region of stripe window. However, the dislocation density is almost zero in the region of $SiO_2$ stripe. The dislocation density is $10^2$–$10^4$ times lower than that ($1–10\times10^{10}$ $cm^{-2}$) in prior high-efficient III-nitride LEDs and LDs, which are grown directly on the sapphire substrate without $SiO_2$ mask patterns [32].

Another approach to improve the GaN film quality is to obtain high-quality, low-resistivity n-type and p-type GaN. Previously, n-type GaN films were obtained under unintentional doping due to background nitrogen vacancies [13]. With the step of reduction in background doping, intentionally doping n-type GaN was achieved by S. Nakamura *et al.* who used Si and Ge as n dopant atoms for the growth of GaN by MOVPE [33]. The electron concentraction of GaN doped with Si were in the range of $1\times10^{17}$–$2\times10^{19}$ $cm^{-3}$.

As many conformation of semiconductor devices, a p-n junction is always required, and various types of acceptor atoms including Mg and C were tried for forming p-type layers. Unfortunately, these efforts only led to compensated high resistivity material, until Akasaki *et al.* [34] demonstrated that compensated Mg-doped GaN could be converted into

conducting p-type material by low energy electron beam irradiation (LEEBI) treatment. The hole concentration and lowest resistivity were $1\times10^{17}$ and 12 Ω·cm respectively. These values were insufficient for high-power blue LDs and high-brightness blue LEDs. In 1991, hole concentration as high as $3\times10^{18}$ $cm^{-3}$ and resistivity as low as 0.2 Ω·cm were obtained by S. Nakamura by utilizing LEEBI treatment and thermal annealing technique [35]-[37].

Up to now, the bottlenecks in growth techniques for III-nitride materials seem to be broken through. ELOG sapphire substrate has been used to reduce the dislocation density and obtain high-quality crystalline GaN films. Highly doped n- and p-type, low-resistivity GaN films had also been achieved. Though these major difficulties ever suppressed III-nitride semiconductors to become the leading materials in the UV and blue region of the spectrum, the continued efforts contributed by numerous researchers cast the model of III-nitride LEDs and LDs. In the following subsections, some important parameters for III-nitride materials are summerized.

### 1.1.1 Bandgap Energies of III-nitride Alloys

Unlike III-V arsenide and phosphide semiconductor materials, the physics related to III-nitride alloys has not been well developed. For optoelectronic semiconductor devices, the bandgap energy of each semiconductor material is undoubtedly one of the most important

parameters. The bandgap energies of GaN, AlN, InN and other binary alloys at temperature T can be expressed by the *Varshni* formula [38]:

$$E_g(\mathrm{T}) = E_g(0) - \frac{\alpha \mathrm{T}^2}{\mathrm{T} + \beta}, \tag{1.1}$$

where $E_g$(T) is the bandgap energy at temperature T, $E_g$(0) is the bandgap energy at 0 K, $\alpha$ and $\beta$ are material-related constants. The value of $\beta$ is approximately equal to the Debye temperature at 0 K. Several kinds of measurements such as optical absorption, photoreflectance, photoluminescence (PL) are employed to determine these constants. Morkoc [39], [40], Maruska [41] *et al.* suggested that RT bandgap energy of wurtzite GaN on sapphire substrate is 3.42 eV. The bandgap energies of GaN reported by several other researchers are listed in Table 1.2.

Table 1.2. Bandgap energy of wurtzite GaN

| Reference | $E_g$(0) (eV) | $\alpha$ (meV/K) | $\beta$ (K) | Annotation (O:optical absorption; P:PL) |
|---|---|---|---|---|
| [42] | 3.48 | 0.939 | 772 | MBE, epitaxial layer (O) |
| [42] | 3.57 | 1.08 | 745 | MBE, Bulk (O) |
| [43] | 3.512 | 0.566 | 737.9 | OMVPE (O) |
| [43] | 3.458 | 1.156 | 1187.4 | MBE (O) |
| [44] | 3.503 | 0.508 | 996 | VPE (P) |
| [45] | 3.510 | 0.856 | 700 | MBE (P) |
| [46] | 3.489 | 0.732 | 700 | ~ |

The bandgap energies of wurtzite AlN and InN binary alloys described with *Varshni* formula by Guo and Yoshida [47]-[49] are listed in Table 1.3.

It is worth to mention that AlN, GaN, InN normally crystallizes in the wurtzite (hexagonal) structure when they are grown on sapphire substrate. The zincblende form is rare and is accompanied with the wurtzite polytype [52]. Thin film growth and characterization of InN have received less attraction than GaN and AlN, probably due to the fact that high quality and stability of InN is difficult to obtain. However, recent studies demonstrated that high crystal quality of InN could be obtained and a bandgap energy of as low as 0.75 eV was reported [50], [51].

Table 1.3. Bandgap energies of wurtzite AlN and InN

| Reference | $E_g$(300 K) (eV) | $\alpha$ (meV/K) | $\beta$ (K) | Annotation |
|---|---|---|---|---|
| AlN [47] | 6.026 | 1.799 | 1462 | ~ |
| AlN [48] | 6.2 | ~ | ~ | ~ |
| AlN [49] | 6.2 | ~ | ~ | ~ |
| InN [47] | 1.970 | 0.245 | 624 | ~ |
| InN [50] | 0.76 | ~ | ~ | OMVPE (P) |
| InN [51] | 0.75 | ~ | ~ | OMVPE (P) |

For $Al_xGa_{1-x}N$ ternary alloys, Yoshida *et al.* observed that the band gap energy of AlGaN deviates upwards with increase in AlN composition [53]. Hagen *et al.* and Koide *et al.* observed that the bandgap energy of $Al_xGa_{1-x}N$ deviated downward with the increase of AlN composition [54], [55]. They all believed that the bandgap energy could be described with linear combination of AlN and GaN binary alloys, and a second-order correction by

$$E_{AlGaN}(x) = x \cdot E_g(AlN) + (1-x) \cdot E_g(GaN) - b \cdot x \cdot (1-x), \quad (1.2)$$

where $E_g(AlN)$ = 6.20 eV, $E_g(GaN)$ = 3.39 eV, $x$ is the Al composition, and $b$ is the so-called bowing parameter, which is equal to 1.0 ± 0.3 eV. It is noteworthy that, several studies [56], [57] also suggest that this ternary bandgap energy can be described by a linear relationship with AlN composition, which means that the bowing parameter $b$ = 0. However, several different bowing parameters of AlGaN ternary alloys can be found as well, which are listed in Table 1.4 for better references.

Due to the smaller bandgap energy of InGaN material than that of GaN, InGaN ternary alloy can be used as a promising active heterostructrue or quantum well (QW) material to emit in the violet and blue region of the spectrum. In 1990, there has been significant process in the growth and characterization of this material [63]-[65]. The bandgap energy of InGaN measured by Osamura *et al.* [66] across the entire compositional range has a smooth variation with some bowing represented by

$$E_{InGaN}(y) = y \cdot E_g(InN) + (1-y) \cdot E_g(GaN) - b \cdot y \cdot (1-y), \quad (1.3)$$

where $E_g$(InN) = 2.07 eV, $E_g$(GaN) = 3.4 eV, $y$ is In composition, and $b$ = 1.0 eV. The bandgap energy dependent on the In more fraction of $In_yGa_{1-y}N$ has also been widely investigated by a number of researchers [67]-[69]. Among the research of InGaN ternary alloys, the bowing parameter of InGaN is still widely studied. Table 1.5 lists the bowing parameters of InGaN ternary alloy derived from several researchers. It can

be found that the published data on the composition dependence of the bandgap energy of InGaN ternary alloy show significant scatter, with the values of bowing parameter ranging from 1.0 to 4.11 eV [67]-[75].

Table 1.4. Bowing parameter of AlGaN ternary alloy

| Reference | Bowing parameter | Reference | Bowing parameter |
|---|---|---|---|
| [58] | 0.62 ± 0.45 | [61] | 1.3 |
| [59] | 0.53 | [62] | 1.3 ± 0.2 |
| [60] | 0.6 | | |

Table 1.5. Bowing parameter of InGaN ternary alloy

| Reference | Bowing parameter | Reference | Bowing parameter |
|---|---|---|---|
| [70] | 2.39 | [73] | 3.35 |
| [71] | 2.65 | [74] | 3.8 |
| [72] | 3.2 | [75] | 4.11 |

### 1.1.2 Band-Offset Value of III-nitride Alloys

The value of band-offset is quite significant for the design of heterostructure devices. This value also plays a very important role in the analysis of energy band diagram. Band offset is also called band discontinuity in some textbooks. It is obvious that when two different materials are grown next to each other, both the conduction and the valence bands of the two materials will possess discontinuities at the interface. Quality and even feasibility of heterojunction device concepts often depend crucially on values of these band offsets. Several researchers determined

the band-offset values of II-VI and III-V heterostructures experimentally by growth techniques such as MBE and MOCVD. Theoretical calculation indicated that the electronic structure in each layer of a heterojunction became nearly bulklike even a single atomic layer away from the interface, lending credence to the idealized notion of an abrupt band edge discontinuity.

To determine band-offset values of semiconductor materials, X-ray photoelectron spectroscopy (XPS) and ultraviolet photoelectron spectroscopy (UPS) are primarily used by means of electron core level energies. Optical techniques, such as excitation PL and reflectivity, also present a more accurate tool to determine band-offset values. The theoretical calculations of semiconductor heterojunction discontinuities can be divided into three main categories:

(i) empirical rules such as electron affinity rule and common anion rules,
(ii) pseudopotential and linear combinations of atomic orbitals (LCAO) approximations theorem,
(iii) self-consistent calculations for specific interfaces using a super sell geometry.

However, the devotion of the determination of the band-offset values in semiconductor heterojunction from experimental measurements and theoretical calculations exist large discrepancies. This large discrepancy may be related to different factors, among them are:

(i) technical difficulty and often indirect nature of measurements,

(ii) possible dependence of band discontinuity on detailed conditions of interface preparation,

(iii) strain dependence of band discontinuity.

Various types of band alignments can arise in semiconductor interfaces depending on the relative adjustment of energy bands with respect to each other. For semiconductor heterojunctions, there are two most common types of alignments, which are shown in Fig. 1.6. Type I alignment shows that the bandgap of one semiconductor lies completely within the bandgap of the other. This type is the most useful one for optoelectronic devices because one can well imagine that if one material with smaller bandgap energy is sandwiched between another material with larger bandgap energy, the carriers will be confined in the smaller bandgap region and then contribute to light emitting. Type II alignment is the bandgaps of two materials overlap but not completely covering the other. II-VI ZnSe/ZnTe heterojunctions have been used to overcome the difficulities in performing p-ohimc contact for blue ZnSe based lasers.

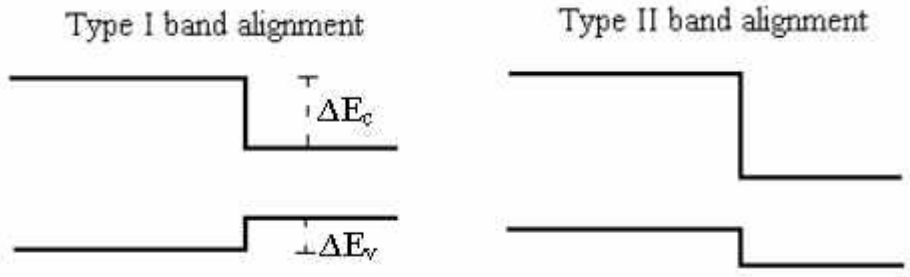


Fig. 1.6. Schematic designation of type I and type II band alignments. (After Ref. 16)

For III-nitride binary alloys, there can be six different kinds of heterojunction combination, such as AlN/GaN, InN/GaN, GaN/AlN, InN/AlN, AlN/InN, and GaN/InN (A/B represents that A thin film is grown on top of B material). The thickness of A thin film is usually 5 ~ 20 Å, and B is always thick enough for the purpose of relaxing strain produced by lattice mismatch between substrate and layers. Fortunately, III-nitride binary alloys all belong to type I, which means that III-nitride materials can be effective optoelectronic semiconductor materials. Table 1.6 lists some band-offset values of wurtzite nitride binary alloys reported by Martin *et al.*

Table 1.6. Valence band-offset values of wurtzite nitride binary alloys (Unit: eV).

| Reference | AlN/GaN | InN/GaN | GaN/AlN | InN/AlN | AlN/InN | GaN/InN |
|---|---|---|---|---|---|---|
| [76] | 0.8±0.3 | ~ | 0.8±0.3 | ~ | ~ | ~ |
| [77] | 0.57±0.22 | 0.93±0.25 | 0.60±0.24 | 1.71±0.20 | 1.32±0.14 | 0.59±0.24 |
| [78] | ~ | ~ | 0.5±0.5 | ~ | ~ | ~ |
| [79] | 1.36±0.07 | ~ | ~ | ~ | ~ | ~ |
| [80] | 0.81 | 0.48 | 0.81 | 1.25 | 1.25 | 0.48 |
| [81] | 0.84 | 0.26 | 0.84 | 1.04 | 1.04 | 0.26 |

As shown in Table 1.6, InN/GaN–GaN/InN and InN/AlN–AlN/InN heterojunctions show a significant forward-backward asymmetry. AlN/GaN–GaN/AlN heterojunctions give almost identical values. The asymmetric nature may be provided by strain induced piezoelectric fields [82] due to that the lattice constant of InN alloy is much larger than those of AlN and GaN, and the lattice mismatch between AlN and GaN is relative

smaller than that between GaN and InN. The III-nitrides are piezoelectric materials, so the strain induced static electric fields via the piezoelectric effect. Figure 1.7 shows how a strain induced piezoelectric field changes the valence band-offset value. It is obvious that strain induced piezoelectric fields always tend to decrease valence band-offset value.

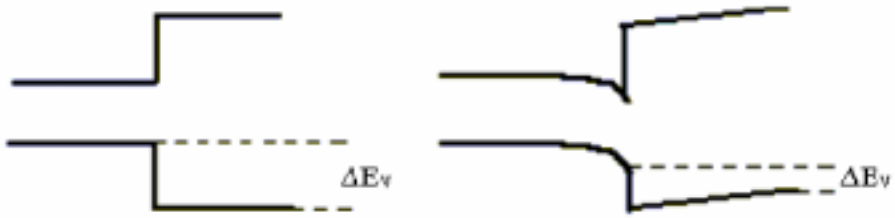


Fig. 1.7. Schematic representation of how piezoelectric effects alter the measured band discontinuities. (After Ref. 16)

Table 1.7. Valence band-offset values after piezoelectric correction

| Heterojunction | InN-GaN | GaN-AlN | InN-AlN |
|---|---|---|---|
| $\Delta E_v$ (eV) | 1.05±0.25 | 0.7±0.24 | 1.81±0.20 |

When InN is at the bottom, there exist much strong piezoelectric fields. Large fraction of InN will practically contain defects and indeed these defects will relax some strain. Hence, larger valence band-offset vlaue can be obtained after some rough corrections for small strain induced piezoelectric fields, and the asymmetry of InN/GaN–GaN/InN and InN/AlN–AlN/InN heterojunctions will disappear. Table 1.7 lists the valence band-offset values after piezoelectric correction.

After some calculations, the ratios of conduction band discontinuities

to valence band discontinuities ($\Delta E_c$ : $\Delta E_v$) are roughly 30 : 70 for InN-GaN, 75 : 25 for GaN-AlN, and 60 : 40 for InN-AlN respectively [82].

### 1.1.3 Lattice Constant of III-nitride Alloys

Lattice constants of semiconductor materials are important in the growth processes because the difference in lattice constants of two neighboring layers is desirous to obtain. Especially, not only the recent commonly used substrates for the growth of III-nitride alloys are lattice mismatch to III-nitride materials, but ternary AlGaN, InGaN and binary GaN alloys are lattice mismatched with each other. Unlike the AlGaAs ternary alloys, which can be obtained by the combination of AlAs and GaAs without considering any lattice mismatch problem as indicated in Fig. 1.2, Fig. 1.8 shows that the dependence of coherency of the growth of AlGaN and InGaN ternary alloys on thick GaN as a function of alloy composition [16]. The solid lines in both figures are estimated from the equilibrium theory by Matthews and Blakeslee in 1974, and Fisher *et al.* in 1994, respectively. As shown in Fig. 1.8, though the experimental results exceed calculated critical layer thickness, it shows coherent growth. Note that, the critical layer thickness for $In_yGa_{1-y}N$ ternary alloy is about 40 nm in experimental demonstration. It indirectly indicates that the crystal of InGaN alloy in prior InGaN/GaN double-heterostructure LDs is so poor that their performance is disappointed, until the QW LEDs and LDs is

fabricated to prevent the crack of InGaN active layer.

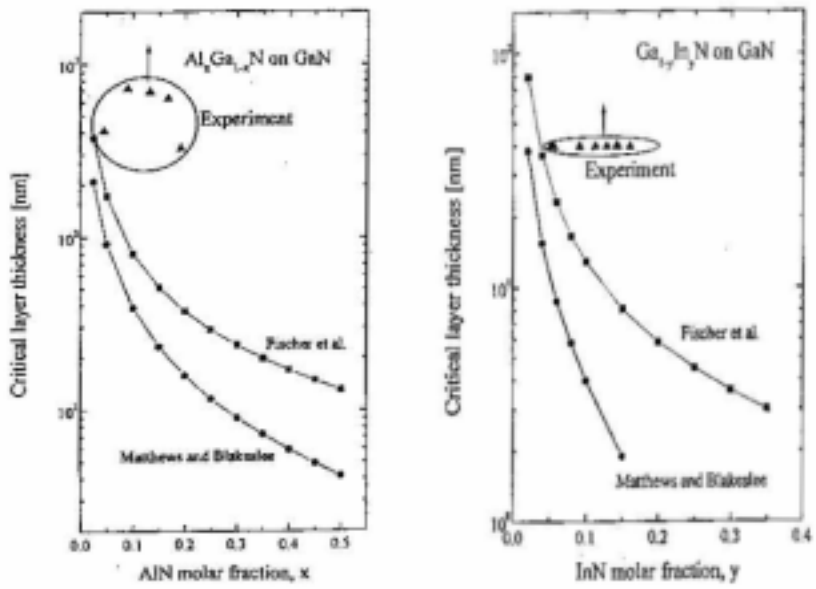


Fig. 1.8. Dependence of coherency of the growth of AlGaN and InGaN ternary alloys on thick GaN as a function of alloy composition. (After Ref 16)

Table 1.8 summarizes the lattice constants of binary AlN, GaN and InN obtained from several references. It is noteworthy that, III-nitride materials are usually grown on c-face sapphire substrates. For ternary AlGaN and InGaN, the lattice constants can be described by Vegard's Law, which linearly combines the lattice constants of two binary alloys and obtains the lattice constants of ternary alloys. For example, the lattice constant of $In_yGa_{1-y}N$ can be obtained by

$$a_{InGaN}(y) = a_{GaN} \cdot (1-y) + a_{InN} \cdot y\,, \tag{1.4}$$

$$c_{InGaN}(y) = c_{GaN} \cdot (1-y) + c_{InN} \cdot y\,, \tag{1.5}$$

where $a_{InGaN}(y)$ and $c_{InGaN}(y)$ represent the lattice constant of InGaN material of $y$ indium composition, $a_{GaN}$, $a_{InN}$, and $c_{GaN}$, $c_{InN}$ are binary GaN and InN lattice constants.

Table 1.8. Lattice constants of binary AlN, GaN, InN alloys

| Reference | a-lattice constant (Å) | | | c-lattice constant (Å) | | |
|---|---|---|---|---|---|---|
| | AlN | GaN | InN | AlN | GaN | InN |
| [16] | 3.112 | 3.188 | 3.533<br>3.548 | 4.982 | 5.185 | 1. 963<br>5.760 |
| [83] | 3.112 | 3.188 | 3.542 | 4.982 | 5.185 | 5.72 |
| [13] | 3.112 | 3.189 | 3.54 | 4.982 | 5.185 | 5.70 |
| [84] | 3.091 | 3.174 | 3.538 | 4.954 | 5.169 | 5.707 |
| [85] | 3.111 | 3.189 | 3.544 | 4.978 | 5.185 | 5.718 |
| [86] | 3.112 | 3.210 | ~ | 4.995 | 5.237 | ~ |
| [87] | 3.112 | 3.188 | ~ | 4.982 | 5.185 | ~ |
| [88] | 3.06 | 3.17 | 3.53 | 4.91 | 5.13 | 5.54 |
| [89] | ~ | 3.162 | ~ | ~ | 5.142 | ~ |
| [90] | 3.10 | 3.22 | 3.59 | 4.97 | 5.26 | 5.81 |
| [91] | 3.144 | 3.146 | ~ | 5.046 | 5.125 | ~ |

### 1.1.4 Effective Masses of III-nitride Alloys

In the analysis of energy band diagram and some characteristics such as carrier mobility of semiconductor materials, the effective masses of electron and hole are relatively significant. In general, the effective mass can be defined by

$$\frac{1}{m^*} = \frac{1}{\hbar}\frac{d^2E(k)}{dk^2}, \tag{1.6}$$

which relates the effective mass of a carrier directly to the local curvature of the energy band at the specified $k$ vector. Figure 1.9 shows a schematic energy band diagram. The curvature of the conduction band is normally smaller than that of the valence band when the energy band diagram is under the situation of tensile or compressive strain.

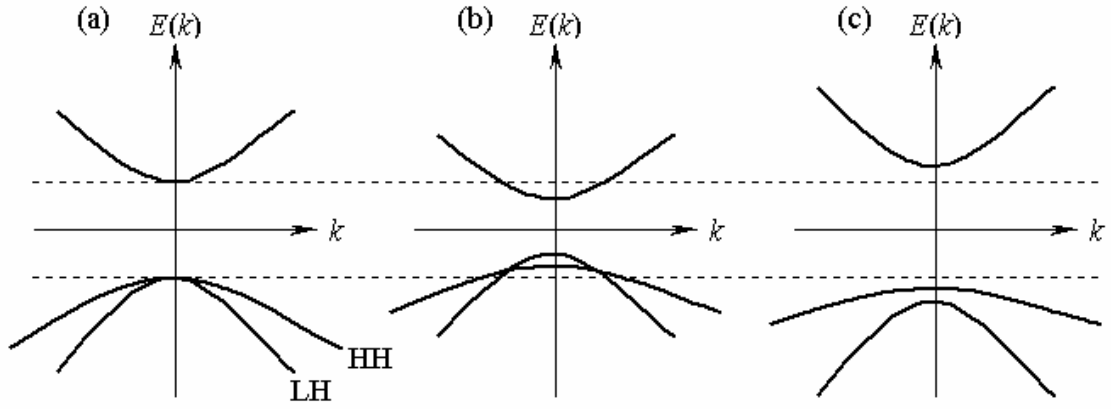


Fig. 1.9. Schematic illustration of energy band diagrams under different kind of strain, (a) no strain, (b) tensile strain, (c) compressive strain.

When a material is under tensile strain, as shown in Fig. 1.9(b), the bandgap energy becomes smaller than that without any strain. The conduction band drops down when both light hole (LH) and heavy hole (HH) valence bands rise up. Moreover, the LH and HH valence bands will split off at a specific $k$ value, and the LH valence band becomes closer to the conduction band. The anti-symmetry energy band diagram can be observed when a material is under compressive strain, which indicates that the bandgap energy becomes larger than that without strain, the conduction band rises up when both LH and HH valence bands drop down, and the HH

valence band becomes closer to the conduction band.

Table 1.9. Effective mass of III-nitride binary alloys (Unit: $\times m_0$)

| Reference | Alloy | $m_e^{//}$ | $m_e^{\perp}$ | $m_{HH}^{//}$ | $m_{LH}^{\perp}$ | $m_{LH}^{//}$ | $m_{LH}^{\perp}$ |
|---|---|---|---|---|---|---|---|
| [92] | AlN | 0.33 | 0.25 | 3.70 | 6.25 | 3.7 | 0.25 |
| [14] | GaN | 0.2 | | | 0.8 | | |
| [93] | | 0.2±0.06 | | | 0.2±0.02 | | |
| [92],[94] | | 0.20 | 0.18 | 1.10 | 1.64 | 1.10 | 0.15 |
| [95] | | 0.19 | 0.17 | 1.76 | 1.69 | 1.76 | 0.14 |
| | | | | 1.96 | 1.87 | 1.96 | 0.14 |
| [14] | InN | 0.11 | | | 0.16 | | |
| [96] | | 0.12 | | 0.5 | | 0.17 | |
| [95] | | 0.11 | 0.10 | 1.56 | 1.68 | 1.56 | 0.11 |
| | | | | 1.67 | 1.67 | 1.61 | 0.11 |

Several values of electron and hole effective masses for AlN, GaN, and InN binary alloys are listed in Table 1.9, in which $m_e$, $m_{LH}$, and $m_{HH}$ represent the effective masses of electron, light hole, and heavy hole respectively. Besides, $m_e^{//}$ and $m_e^{\perp}$ are the electron effective masses parallel to the junction plane and perpendicular to the junction plane, respectively. For ternary nitride alloys, the effective masses can be obtained by linear combination (Vegard's Law) of two binary alloys.

### 1.1.5 MBE and OMVPE Growth Techniques

Growth of III-V semiconductor materials by several techniques was well established for producing high-quality crystalline thin films. Even

though well-developed diffusion and ion implantation techniques can provide n-type and p-type materials for the production of field effect and bipolar transistors in early stage, high performance heterojunction and QW emitters can not be produced by this kind of growth technique due to the complex structure of heterostructures and QW devices. Hence, the materials used for optoelectronic devices must be produced by epitaxial growth techniques. Vapor processes using either hydrides or the volatile group V halides are the earliest epitaxial techniques. However, these vapor-phase epitaxial (VPE) techniques were only capable of producing early GaAsP and other materials used for LEDs. They are also awkward for producing high performance emitters.

The other early epitaxial technique for the production of III-V optoelectronic devices is liquide-phase epitaxial (LPE) growth technique, which is simple and capable of producing high-quality materials for emitters even for the production of heterostructures. Unfortunately, LPE is unsuitable for the growth of quarternary AlGaInP and III-nitride materials. Moreover, it is awkward for the production of QW structures and superlattice layers. MBE and OMVPE growth techniques can provide QW structures and superlattice layers to fabricate recent red AlGaInP and violet, blue, green high-brightness LEDs and high-performance III-nitride LDs.

*A. Molecular Beam Epitaxy (MBE)*

MBE growth technique, which is the most powerful technique for the

production of superlattice and QW structures, was developed in the late 1960s and early 1970s [13]. Basically, this growth technique is a highly refined, ultrahigh-vacuum (UHV) evaporation process. This technique has several advantages such as crystallization with low-temperature growth, ease of layer thickness control, and externally *in situ* measuring the characteristics of materials in the processes of growing crystals. This technique is also useful for growing III-nitride materials. Presently, there are many research organizations and academic laboratories using MBE for the production of optoelectronic materials.

In the processes of growing III-nitride materials in MBE facilities, the raw materials of Al, Ga, and In atoms are all metals. These raw materials are put in effusion cell, and are spurted intermixing with nitride atoms after heating. As for the providing of nitrogen (N) atoms to combine with group III atoms, there are three major approaches, as shown in Fig. 1.10. One of these methods is using $NH_3$ gas as raw material to produce N atoms as shown in Fig. 1.10(a). The second method is to use electron cyclotron resonance (ECR) and radio frequency (RF) methods to make $N_2$ gas become plasma, as shown in Fig. 1.10(b) and Fig. 1.10(c) [97]. Sapphire, 6H-SiC, and GaAs are usually used as substrates. AlN or GaN may be used as buffer layer. And, the dopants for n-type and p-type layers are usually silicon (Si) and magnesium (Mg) atoms.

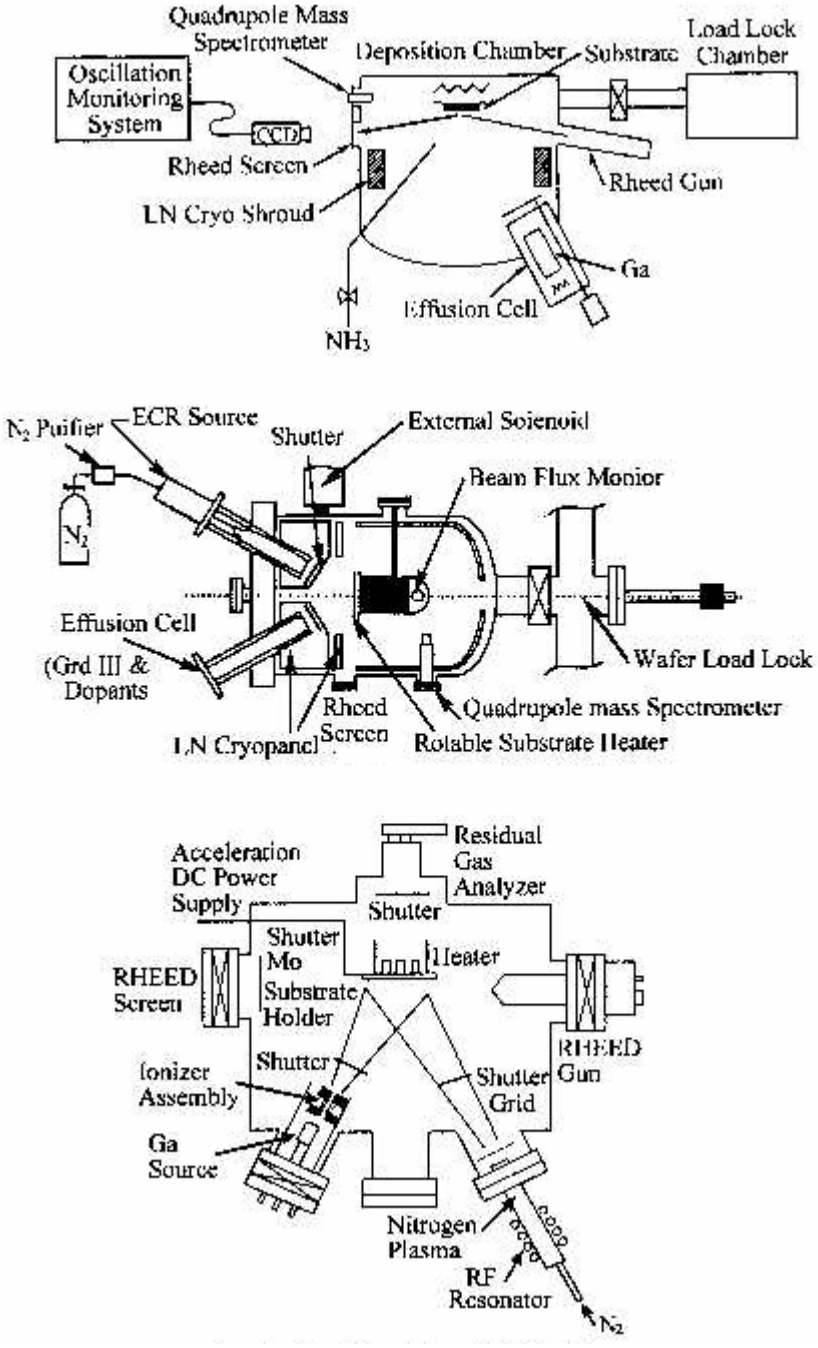


Fig. 1.10. MBE systems using (a) $NH_3$, (b) ECR, (c) Rf as nitride sources. (After Ref. 97)

*B. Organometallic Vapor-phase Epitaxy (OMVPE)*

Organometallic vapor-phase epitaxial growth technique, which is also known as metalorganic chemical vapor deposition (MOCVD), for the growth of III-nitride materials has received much attention recently, since super-bright III-nitrides blue LEDs have been commercialized with the use of this technique in 1994 [13]. With the technique of OMVPE, the III-nitride blue and green direct bandgap LEDs and AlGaInP yellow and red LEDs have made full-color display become realistic. Besides, another improved technique, the two-flow MOCVD presented by Nakamura *et al.* [25], [98], has made blue, green LDs to be commercialized.

OMVPE is a nonequilibrium growth technique relying on vapor transport of the precursors. Subsequent reactions of group V hydrides and group III alkyls are in a heated zone. Unlike MBE technique growth, the sources of group III materials are metalorganisms such as trimethylaluminum (TMAl), trimethylgallium (TMGa), and trimethylindium (TMIn). These metalorganisms are stored in bubblers through which a carrier (hydrogen typically) flows. Most commonly, the sources of Group V are gaseous hydrides such as $NH_3$ for nitrides. Metal organic precursors (diethylzinc DEZn), cyclopenta dienyl magnesium ($Cp_2Mg$) or hydrides (silane or disilane $Si_2H_6$) are usually used as dopants for p-type and n-type materials.

The pioneers of the achievement of high-brightness blue LEDs are Nakamura, Mukai, Senoh *et al.* in Nichia Chemical Industries [63]-[65],

[99]. They have employed a novel two-flow MOCVD that yielded high-quality films. As shown in Fig. 1.11, the reactor sources are carried from a horizontal inlet. A vertical subflow, which was found to improve crystal quality and increase growth rate, drives the reactants to the growing film surface.

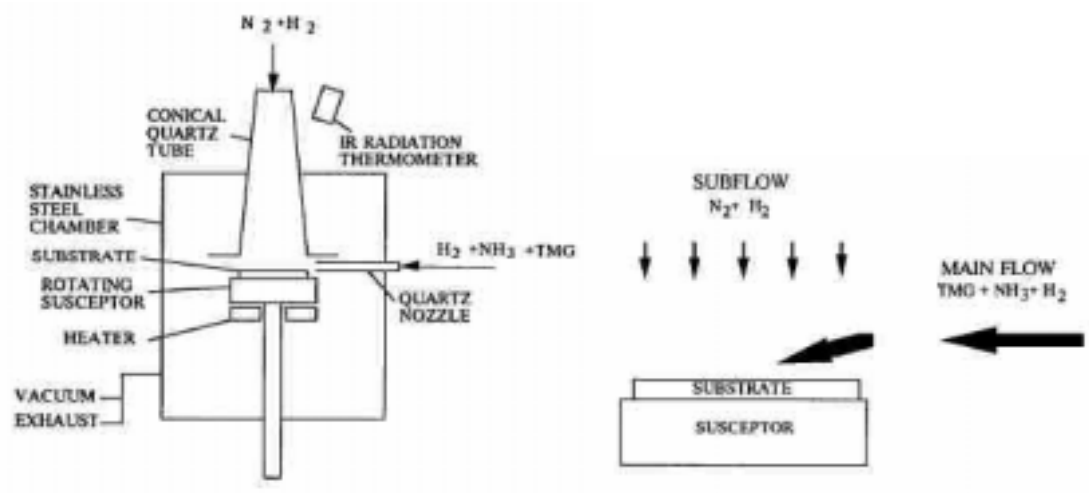


Fig. 1.11. Two-flow MOCVD approach. (After Ref. 32)

## 1.2 Introduction to Nitride Based LEDs

The bandgap type of III-nitride materials with wurtzite crystal structure is direct, and its bandgap energy can be varied from 1.89 to 6.28 eV approximately. Therefore, fabrication of highly efficient ultraviolet to red emitters is feasible by using this kind of materials. As mentioned in section 1.1, sapphire and 6H-SiC have been used as substrates for the epitaxial growth of III-nitride materials. Even though the lattice between substrate and epitaxial layers is still mismatched, thin AlN or GaN buffer layers grown at low temperature evidently improve the quality of GaN films grown at high temperature. The achievement of high-quality and low-resistivity p-type GaN layers is also an important breakthrough for the fabrication of high-performance III-nitride LEDs and LDs. In this section, a brief history of development of III-nitride LEDs and recent commercialized III-nitride LED structures are intoduced.

Despite the fact that the blue LEDs made up by SiC material has been commercialized for several years, its brightness was only several decade minicandela (mcd). Since the first candela-class blue LEDs were fabricated in 1994 [13], the market of blue LEDs has almost been dominated by III-nitride materials. As shown in Fig. 1.12, the achievement of III-nitride LEDs is rapidly increased since 1994, and recently super high-brightness LEDs has also been fabricated [100].

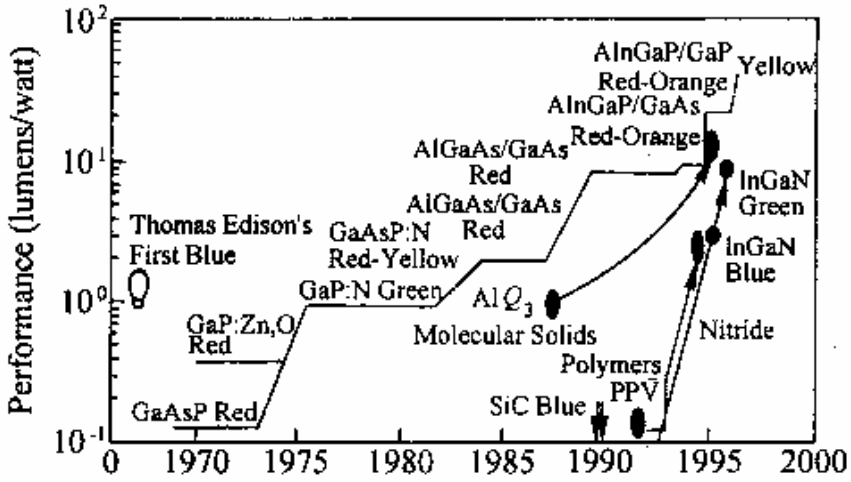


Fig. 1.12. A review of the historical revolution of LEDs. (After Ref. 97)

For green LEDs, the performance of conventional GaP LEDs is poor due to the nature of its indirect bandgap, even though this material can be doped with nitride isoelectronically to enhance its performance [101]-[103]. The emission wavelength of ioselectronical nitrogen doped GaP is 555 nm, which is yellowish green in color. AlGaInP is another material suitable for green LEDs; however, at present a maximum external quantum efficiency of about 1% may be obtained at an emission wavelength of 570 nm. If the emission wavelength is reduced to the green region, the performance will deteriorate markedly, because the bandgap type becomes indirect. Basically, green LEDs can also be fabricated with III-nitride materials by increasing the indium composition in InGaN active layers. Unfortunately, poor crystal quality of InGaN active layers, and hence reduced LED performance, is found due to large lattice mismatch between active layers and claddings.

Therefore, high-performance green LEDs were too difficult to be commercialized in early stage.

### 1.2.1 Blue and Green InGaN LEDs

Nakamura *et al.* fabricated blue InGaN/GaN double-heterostructure LEDs for the first time in 1993 with the use of two-flow MOCVD growth technique. For this device fabrication, the c-face (0001 orientation) sapphire was used as the substrate and the growth was conducted at atmospheric pressure. Firstly, the substrate was heated to 1050 ºC in a stream of hydrogen. Then the temperature was lowered down to 510 ºC for the growth of GaN buffer layer. Next, the substrate was reheated to 1020 ºC to grow 4-μm n-type GaN film, followed by the Si-doped InGaN film when the temperature was decreased to 800 ºC. The thickness of Si-doped InGaN active layer was approximately 200 Å. The temperature was then increased to 1020 ºC to grow p-type (Mg doped) GaN film. The total thickness was about 4.8 μm, and the surface of p-type GaN was partially etched until the n-type layer was exposed. Finally, a Ni–Au contact was evaporated onto the p-type GaN layer and a Ti–Al contact onto the n-type GaN layer. The peak wavelength was 440 nm with a full width at half maximum (FWHM) of 20 nm at forward current of 20 mA.

To obtain blue emission, the first candela-class blue LEDs were fabricated with the use of Si and Zn codoped InGaN active layer. Due to

higher indium composition in InGaN layer that might cause the decrease of luminescence intensity, relatively low indium composition in InGaN layer was used. Figure 1.13(a) shows the cross-section view of InGaN/AlGaN DH LEDs, which were also demonstrated by Nakamura *et al.* [13]. The thickness of InGaN active layer was 50 nm, and the active layer was sandwiched between two 150-nm-thick $Al_{0.15}Ga_{0.85}N$ cladding layers. Other layers and processes were almost the same as previous InGaN/GaN DH LEDs except that $N_2$ ambient thermal annealing was performed to obtain a highly p-doped GaN layer at a temperature of 700 ºC after the growth [32].

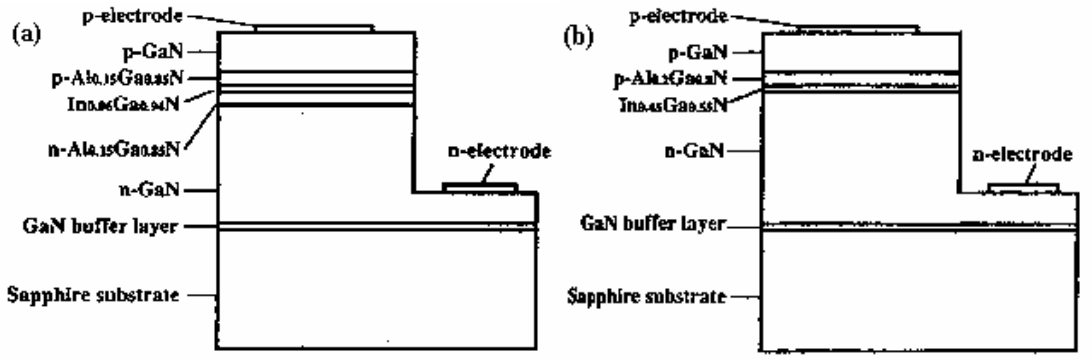


Fig. 1.13. Cross-section view of (a) InGaN/AlGaN DH LEDs, and (b) green SQW LEDs. (After Ref. 13 and 32)

The characteristics of InGaN/AlGaN DH LEDs were measured under dc-biased conditions at room temperature. The peak wavelength and FWHM were 450 nm and 70 nm respectively at forward current of 10 ~ 40 mA. The output power and external quantum efficiency at 20 mA were 1.5 mW and 2.7%. At present, the brightness of InGaN/AlGaN DH blue LEDs

is sufficient to be commercialized for the full-color LED display, especially for outdoor applications.

With the increase of the indium composition in InGaN active layer from 0.06 to 0.19, blue-green LEDs could be obtained for specific applications. Zn doped InGaN active layer was fabricated, and the longest wavelength of InGaN/AlGaN DH LEDs was 500 nm. The output power was 1.0 mW at forward current of 20 mA, which is sufficiently bright for outdoor applications such as displays and especially for traffic lights. But for pure green LEDs, emission wavelengths between 510 and 530 nm are required. To obtain green emission, the indium composition in InGaN active layers shall be increased. Unfortunately, poor crystal quality of InGaN active layer was observed. However, if the InGaN active layer becomes as thin as QW structure, the elastic strain will not be relieved by the formation of misfit dislocations, and the crystal quality of the InGaN active layer will be improved at the same time.

As depicted in Fig. 1.13(b), the single-quantum-well (SQW) green LED structure consists of a 30-nm-thick GaN buffer layer grown at 550 ºC, a 4-μm-thick Si-doped n-type GaN layer, a 3-nm-thick active layer of undoped $In_{0.45}Ga_{0.55}N$, a 100-nm-thick Mg-doped p-type $Al_{0.2}Ga_{0.8}N$ layer, and a 0.5-μm-thick Mg-doped p-ytpe GaN layer. The active layer consists of an $In_{0.45}Ga_{0.55}N$ SQW. The output powers of blue and green SQW LEDs are 5 mW and 3 mW, respectively. The performance of green SQW LEDs is relatively poor in comparison with that of blue ones, probably due to the

poor crystal quality of InGaN active layer. The peak wavelengths of the blue and green SWQ LEDs are 450 nm and 520 nm.

Blue and green LEDs with multi-quantum-well (MQW) structures were also fabricated [13], [104]. The structures are almost the same as those of SQW LEDs, except for the active region. The active region of blue MQW LEDs consists of six 3-nm-thick undoped $In_{0.27}Ga_{0.73}N$ wells and seven 15-nm-thick GaN barriers. The output powers of blue and green MQW LEDs are 11 mW and 8 mW respectively.

### 1.2.2 Amber and Ultraviolet InGaN LEDs

The research of amber InGaN LEDs can rarely be found [100], [105], [106], probably due to the difficulty of determining the exact indium composition in the InGaN active layer. Another possible cause is that the amber LEDs made by III-phosphide materials have been well developed much earlier than that by III-nitride materials. However, Mukai *et al.* showed that the performance of amber InGaN LEDs was superior to those of amber AlGaInP LEDs [100]. As shown in Fig. 1.14, the output power of amber InGaN is 1.4 mW at 25 ºC, which is almost twice as high as that of AlGaInP LEDs. In the mean time, the temperature dependence of amber InGaN LEDs is relatively less sensitive than that of AlGaInP LEDs, probably due to a small carrier overflow caused by a large band offset between the active layer and the cladding layers in InGaN system.

For the case of lighting, white light can be generated by several different methods [107]-[110]. Combining a phosphor wavelength converter with a blue III-nitride LED chip is the most commonly used method. The blue light emitted from the LED chip is absorbed by the yttrium aluminum garnet (YAG) phosphor and reemitted as yellow phosphorescence. Thus, white light can be generated by the combination of these two emission bands. However, there still exists some problems with such “blue + yellow” white LEDs [107]. To solve these problems, an ultraviolet (UV) LED chip can be used as the excitation source, which is similar to fluorescent light tube [111]. Unfortunately, high efficient UV LED chips are difficult to achieve due to low doping efficiency in AlGaN with a high Al composition resulting in low quantum efficiency.

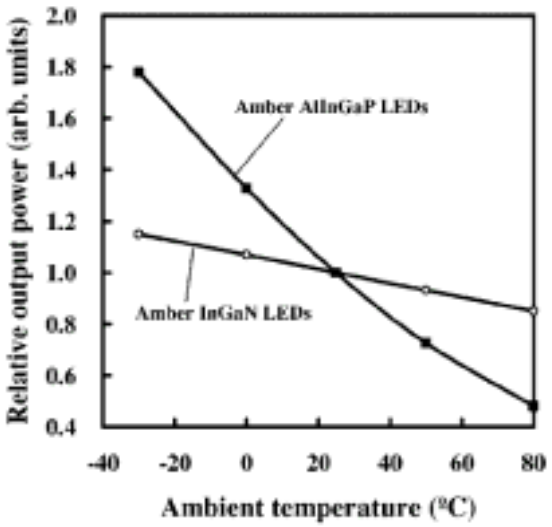


Fig. 1.14. Output performances of amber InGaN and AlGaInP LEDs as a function of ambient temperature. The output power of each LED is normalized to 1.0 at 25 ºC. (After Ref. 100)

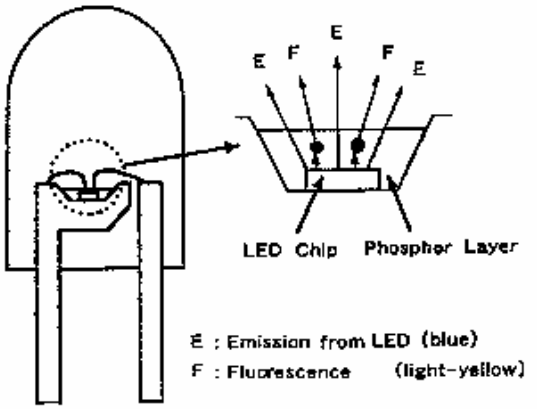


Fig. 1.15. A schematic structure of white LED. (After Ref. 14)

Since the bandgap energies of III-V arsenide and phosphide materials are relatively small, they cannot be applied to UV spectral region. In this respect, the III-nitride material is a better candidate. UV LEDs are important emitters for white LEDs, which are promising in backlighting for full-color liquid crystal displays (LCD) and replacement of conventional light bulbs or fluorescent lamps. A schematic white LED structure is shown in Fig. 1.15. The structure is almost the same as that of conventional QW LEDs, except for the phosphor layer additionally put on top of the blue or UV LED chip. When excited by blue or UV light, the phosphor can emit yellow fluorescence. Then, the mixture of the blue and yellow light results in white emission. Recently, white LEDs have been commericialized for illumination; nevertheless, the performance of recent white LEDs still need to be enhanced for the purpose of replacement of conventional light bulbs and fluorescence lamps.

## 1.3 Introduction to Nitride Based LDs

As mentioned above, the brightness of blue and green LEDs are sufficient for commercial applications. As a matter of fact, full-color displays for outdoor applications are now available. At present, the main focus on III-nitride materials is to fabricate the room-temperature (RT), continuous-wave (CW), high output power, and low threshold current density LDs. In the history of the development of III-nitride LDs, the first room-temperature pulse-operation LDs under pulse current injection was demonstrated by Nakamura *et al.* in 1996 [112]. The active region of the laser diode consists of seven periods of $In_{0.2}Ga_{0.8}N/In_{0.05}Ga_{0.95}N$ MQWs. The thickness of wells and barriers in active layers are 2.5 nm and 5.0 nm, respectively. A schematic laser diode structure is shown in Fig. 1.16.

Note that, a 20-nm-thick layer of p-type $Al_{0.2}Ga_{0.8}N$ is directly grown on top of the active region to prevent the indium from evaporating out of the active region at high temperature growth of p-type GaN. The ridge structure in this specific device was formed by reactive ion etching (RIE) technique. The emission wavelength is 417 nm, which is violet in color. The differential quantum efficiency per facet was estimated to be 17%, and the pulse output power was 57 mW at a current of 700 mA. The lasing emission lifetime was only a couple of nanoseconds. Despite this extremely short lifetime, it creates a possibility for the realization of violet and blue LDs of III-nitride materials.

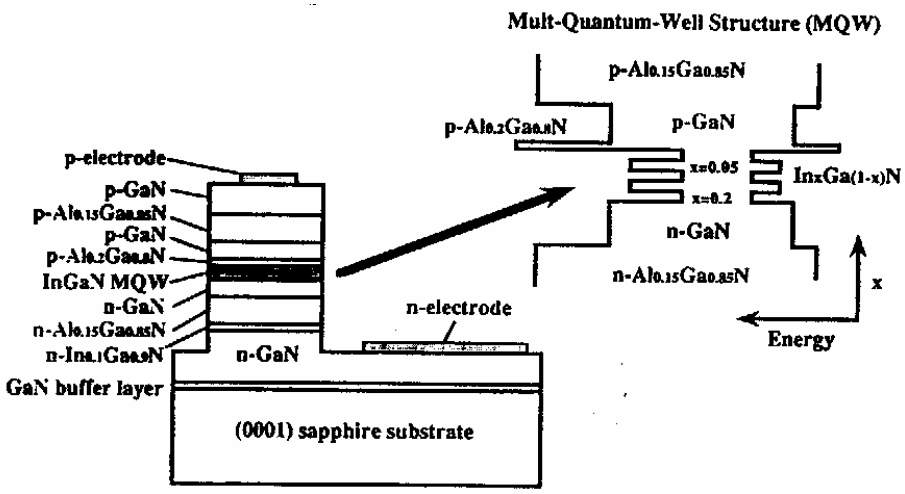


Fig. 1.16. Schematic cross-section view of the first III-nitride LD. (After Ref. 112)

The above violet LDs were operated only under pulsed current injection at room temperature. For CW operation, LDs of much better efficiency should be fabricated. In the mean time, the threshold current and operating voltage must be decreased because high threshold current and operating voltage may result in large amount of heat, which in turn reduces the laser emission lifetime. The first CW operation of InGaN MQW LD at 233 K was also fabricated by Nakamura *et al.*, and the threshold current density and operating voltage were reduced to 8.7 kA/cm$^2$ and 11 V by adjusting the growth, ohmic contact, and doping profile conditions [31], [112]-[116]. However, these efforts still could not make LDs to operate under RT CW condition.

The first RT CW InGaN MQW-structure LD was demonstrated by Nakamura *et al.* in 1996 [117]. However, the operation lifetime of those LDs was only 1 s due to large heat generation, and the threshold current

density was as high as 9 kA/cm$^2$. The lifetime of III-nitride LDs was increased to 27 hours, and the threshold current density was reduced to 3.6 kA/cm$^2$ in early 1997 [118], but the output power was only a couple of milli watts. A high power of 50 mW, high operating temperature of 100 ºC, and long lifetime of 300 hours operation LD was observed in 1997 as well [119]. The LDs existed relative low threshold current density of 4.2 kA/cm$^2$, and very low threshold voltage of 4.3 V, which were apparently improved when compared with previous LDs. However, the threshold current and voltage are still a little high, and the operation lifetime is too short to be commercialized. It is noteworthy that, the number of InGaN layers of these LDs was reduced to only three or four.

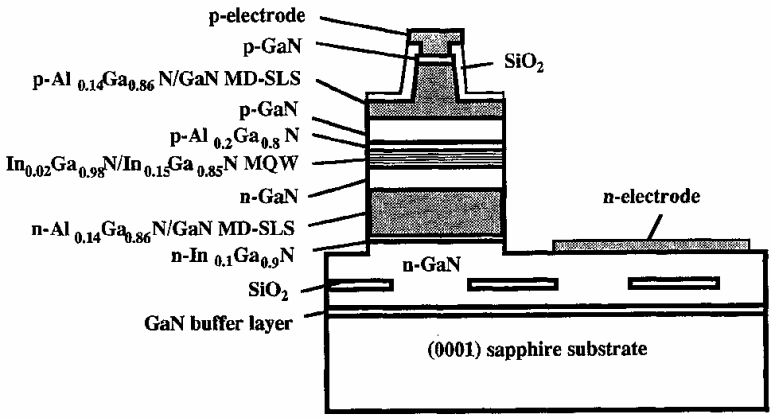


Fig. 1.17. A schematic structure with MD-SLSs grown on ELOG sapphire substrate. (After Ref. 120)

To enhance the performance of InGaN MWQ LDs and improve the operation lifetime, Nakamura *et al.* used ELOG substrate [13], [120], and

the conventional $Al_{0.15}Ga_{0.85}N$ cladding layers were changed by $Al_{0.14}Ga_{0.86}N$/GaN modulation doped strained-layer superlattice cladding layers (MD-SLSs) to prevent crack caused by the lattice mismatch between AlGaN and GaN layers, and reduce the threshold voltage. A schematic LD structure with MD-SLSs grown on ELOG sapphire substrate is shown in Fig. 1.17. An apparent improvement from this new progress was that the lifetime was more than 1,000 hours under RT CW operation. The threshold current density was 4 kA/cm$^2$ under RT CW operation. The operating voltage at the threshold current was only 5 V. By using the same techniques, the estimated lifetime of the InGaN LDs under RT CW operation had been further improved to more than 10,000 [121] and 15,000 hours [122]. Threshold current densities as low as 1.2 kA/cm$^2$ were achieved using $In_{0.15}Ga_{0.85}N$ QWs [123]. These results apparently lead to the commercialization of InGaN MQW LDs.

# Chapter 2. Optimization Study of the Number of InGaN Well Layers in Violet-Blue LDs

High-performance LDs for laser pick-up heads are important for the optical storage systems. Recently, the well-developed 650/630 nm AlGaInP based LDs have been commercialized for DVD system for several years, which can provide 4.7 Gb storage capacity in a disk. In general, the capacity of an optical disk is proportional to the square of the inverse of laser emission wavelength of laser pick-up heads. In other words, the storage capacity in a disk can be increased by shortening the laser emission wavelength of the pick-up heads. Hence, the laser pick-up heads with shorter emission wavelength in violet-blue region of the spectrum made up by III-nitride materials are desired, due to their unique high-performance emitters that can provide shorter wavelength of the spectrum for the next-generation high-density digital versatile disk (HD-DVD) system. It is expected that the HD-DVD can provide at least 18 Gb capacity in a disk.

In this chapter, a review of recent published nitride based violet and blue LDs is firstly discussed. It is mainly focused on the design of the number of quantum well layers in violet-blue InGaN LDs. Specifically, the optimization design of the number of InGaN layers in violet and blue LDs is studied by using the LASTIP (LASer Technology Integrated Program) simulation program. The electrical and optical properties of violet-blue LDs are discussed as well.

## 2.1 Recent Study of the Number of InGaN Well Layers in InGaN/InGaN LDs

For the design of III-nitride LDs structure to improve laser performance, several industrial companies had demonstrated variant kinds of LD structures. Among these companies, Nichia corporation industry plays the leading role of the development of III-nitride LDs. Their research is closely related to the history of the development of III-nitride LDs. In these LDs fabricated by Nichia Inc., the number of InGaN QW layers had been reduced to only three or four from twenty-six [97]. Nakamura, who used to be one of the researchers in that company, is the pioneer of the realization of III-nitride LDs. Based on their research, they concluded that when the emission wavelength was in a range from 390 to 420 nm, the lowest threshold current density could be obtained when the number of InGaN well layers was two. As depicted in Figure 2.1(a), the lowest threshold current density of InGaN MQW LDs with an emission wavelength of about 400 nm can be obtained when the number of well layers is two [123].

In 2000, Nakamura further demonstrated that when the emission wavelength was increased beyond 435 nm, the lowest threshold current density could be obtained when the number of InGaN well layers was one. Figure 2.1(b) shows the threshold current density of the LDs with an emission wavelength of 435 nm as a function of the number of InGaN well

layers [124]. Nakamura *et al.* believed that higher threshold current density of long emission wavelength MQW LDs with more In composition in InGaN well layers was related to the dislocation of InGaN well layers.

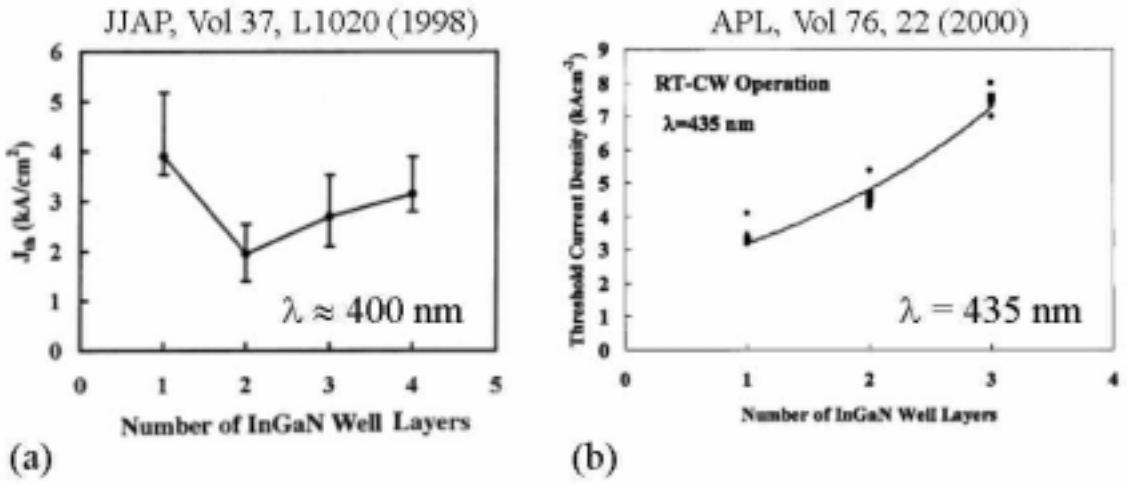


Fig. 2.1. Threshold current density of InGaN MQW LDs as a function of the number of InGaN well layers when the emission wavelength is (a) at 400 nm, (b) at 435 nm. (After Refs. 123 and 124)

In order to obtain a laser diode with long emission wavelength, the indium composition in InGaN well layers must be high. However, the dislocation density is increased respectively due to that the first InGaN well layer could be dissociated during the growth of the second or the third well layer. As a result, the crystal quality of the active layers is degraded. The threshold current density is increased with the increase of the number of well layers, due to an increase of the internal loss of the LD. Several researchers refer this as In-rich phenomenon, since the In atoms tend to gather with each other in the growth of InGaN LDs when the In

composition is increased to obtain long emission wavelength LDs. In fact, it is difficult to avoid the In-rich phenomenon in the growth of InGaN MQW LDs. As a result, the optimization of the number of well layers in InGaN MQW LDs varies from two to one when the emission wavelength is beyond 435 nm [124].

## 2.2 Structure and parameters of InGaN/InGaN LDs Under Study

In the simulation of InGaN/InGaN LDs, a LASTIP simulation program is used to study the optimization design of the number of InGaN well layers with emission wavelength in violet-blue region of the spectrum. A schematic diagram of the preliminary LD structure under study is shown in Fig. 2.2.

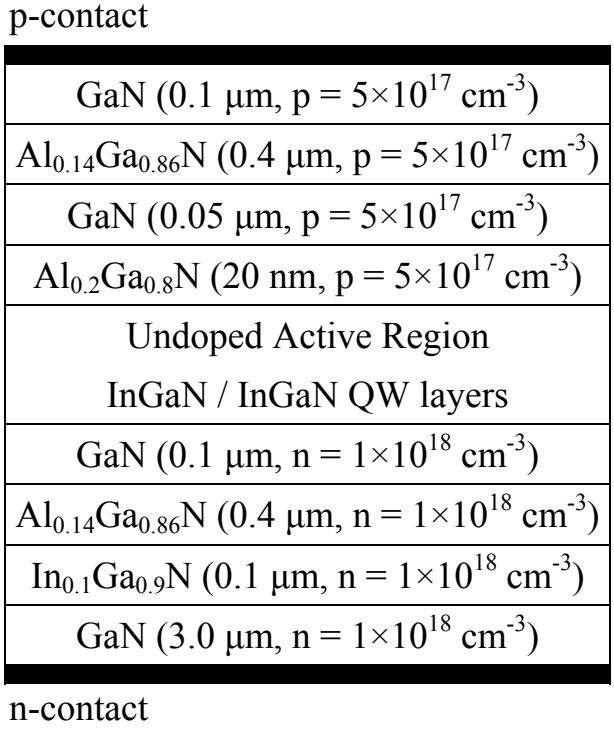


Fig. 2.2. A schematic diagram of the preliminary LD structure under study

The InGaN QW-structure LD device consists of a 3.0-μm-thick layer of n-type GaN, a 0.1-μm-thick layer of n-type $In_{0.1}Ga_{0.9}N$, a 0.4-μm-thick

cladding layer of n-type $Al_{0.14}Ga_{0.86}N$, a 0.1-μm-thick layer of n-type GaN, an $In_xGa_{1-x}N$ / $In_yGa_{1-y}N$ QW active region, a 20-nm-thick layer of p-type $Al_{0.2}Ga_{0.8}N$, a 0.05-μm-thick layer of p-type GaN, a p-type AlGaN cladding layer, and a 0.1-μm-thick layer of p-type GaN. The doping values of n- and p-type layers are all set at $1\times10^{18}$ $cm^{-3}$, and $5\times10^{17}$ $cm^{-3}$ respectively. The n- and p-contact are directly on the bottom and top of the LD structure, respectively. The width of the InGaN LD is 10 μm, and the cavity length is 500 μm. The reflectivity of each end facet can provide 30% reflectivity.

Several important parameters used in the simulation of InGaN/InGaN LD are as follows: the bandgap energies of AlN, GaN, and InN are set at 6.026 [47], 3.401 [42], and 1.970 eV [47] at room temperature, respectively. The bandgap energies of ternary AlGaN and InGaN alloys are:

$$E_{AlGaN}(x) = x \cdot E_g(AlN) + (1-x) \cdot E_g(GaN) - b \cdot x \cdot (1-x), \qquad (2.1)$$

$$E_{InGaN}(y) = y \cdot E_g(InN) + (1-y) \cdot E_g(GaN) - b \cdot y \cdot (1-y), \qquad (2.2)$$

where the bowing parameter of AlGaN and InGaN alloys are assumed to be 1.3 [61], [62] and 3.35 eV [73]. For AlGaN/GaN and InGaN/GaN, the band-offset ratios ($\Delta E_c/\Delta E_v$) of 0.67/0.33 [125] and 0.3/0.7 [16], [126] are used, respectively. The electron and hole effective masses of GaN are assumed to be $0.2\times m_0$ and $0.6\times m_0$, respectively [14], [93]. The electron effective masses of AlN and InN are $0.22\times m_0$ and $0.11\times m_0$ [14], and the hole effective masses are both $0.8\times m_0$ [14]. A uniform hole mobility of 2.0

$cm^2/Vs$ [127] is assumed which is only a rough estimate. The electron mobility values are 200 $cm^2/Vs$ for GaN, 100 $cm^2/Vs$ for InGaN, and 30 $cm^2/Vs$ for AlGaN [127]. The nonradiative recombination lifetime is assumed to be 1 ns for InGaN, and 0.1 ns for AlGaN [128]. The refractive indices of ternary AlGaN and InGaN alloys are

$$n\ (Al_xGa_{1-x}N) = 2.5067 - 0.43x, \tag{2.3}$$

$$n\ (In_yGa_{1-y}N) = 2.5067 + 0.91y, \tag{2.4}$$

when the Al and indium compositions in these two ternary alloys are below 0.3. The refractive index of GaN is 2.5067 [129], [130]. The lattice constants of AlN, GaN, and InN are 3.110 Å [85]-[87], 3.146 Å [91], and 3.544 Å [85], respectively.

## 2.3 Optimization Study of the Number of InGaN Well Layers in Violet-Blue LDs

As mentioned above, the optimization of the number of InGaN QW layers demonstrated by Nakamura *et al.* to obtain the lowest threshold current density is two when the emission wavelength is in a range from 390 to 420 nm, and becomes one when the emission wavelength is beyond 435 nm. However, Nakamura *et al.* only demonstrated the optimization design of the number of InGaN well layers when the emission wavelengths are in a range from 390 to 420 nm and beyond 435 nm. When the emission wavelength is between 420 nm and 435 nm, the optimization of the number of InGaN well layers has not been well documented. It is quite possible that either double-quantum-well (DQW) or SQW LDs can have the lowest threshold current density when the emission wavelength is between 420 nm and 435 nm. However, it is just a simple conjecture, and the study of the optimization of the number of InGaN well layers in a wider emission spectral range (396.1~479.3 nm) has not been well studied so far.

Consequently, the optimization of the number of InGaN well layers in violet-blue LDs is studied in this thesis. The energy band diagram, local gain and stimulated recombination rate in the active region, and electron and hole concentration distribution along the junction plane are also discussed in this section.

To study the optimization of the number of InGaN well layers as a

function of the emission wavelength, it needs to be mentioned that the emission wavelength is determined by varying the indium composition in InGaN well layers and barriers, and the thickness of InGaN well layers. By varying the indium composition in InGaN well layers from 0.10, 0.15 to 0.2, and that in InGaN barriers from 0.01 to 0.08 with a step of 0.01, the emission wavelength can be varied in a wide violet-blue region of the spectrum. Also, the thickness of InGaN well layers is varied from 1.5 to 4.5 nm and that of InGaN barriers is always fixed to twice the thickness of well layers for the purpose of obtaining a relatively small range of laser emission wavelength. The optimization of the number of InGaN well layers as a function of the emission wavelength is discussed in the following subsections. Three subsections when the indium composition in InGaN well layers is equal to 0.10, 0.15, and 0.20 are studied seperately.

### 2.3.1 $In_{0.1}Ga_{0.9}N/In_yGa_{1-y}N$ Design

First of all, the optimization of the number of $In_{0.1}Ga_{0.9}N$ well layers as a function of the emission wavelength is studied when the indium composition in InGaN barriers is varied from 0.01 to 0.04. In this study, a large value of the indium composition in InGaN barriers is not studied because the laser emission wavelength almost remains unchanged. As shown in Fig. 2.3, when the indium composition in InGaN barriers is fixed to 0.01, the emission wavelength can be varied from 396.1 to 414.7 nm

when the thickness of well layers is increased from 1.5 to 4.5 nm. When the indium composition in InGaN barriers is fixed to 0.04, it can be varied from 401.8 to 415.7 nm with increase of the thickness of InGaN well layers from 1.5 to 4.5 nm, respectively.

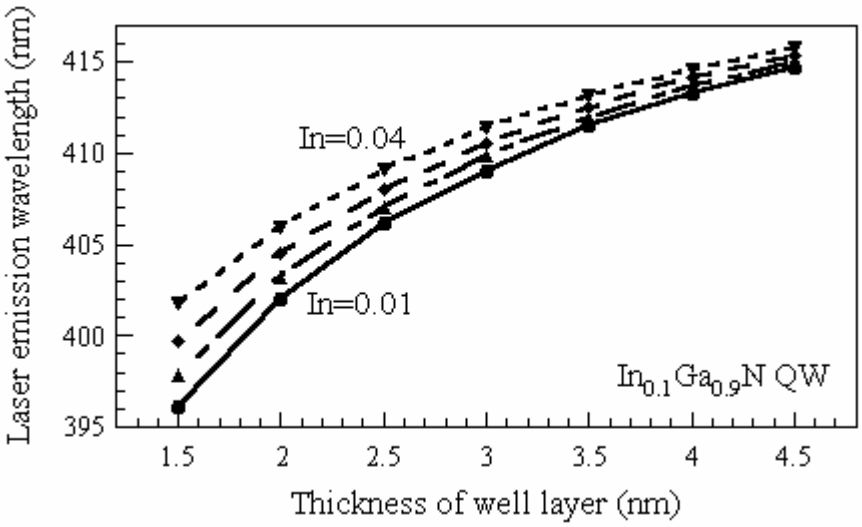


Fig. 2.3. Laser emission wavelength as a function of the thickness of $In_{0.1}Ga_{0.9}N$ well layers when the indium composition in InGaN barriers is at a range from 0.01 to 0.04.

When the thickness of $In_{0.1}Ga_{0.9}N$ well layers is fixed at 1.5 nm, the laser emission wavelengths are 396.1 nm, 397.9 nm, 399.7 nm, and 401.8 nm when the In mloe fraction of InGaN barriers is varied from 0.01 to 0.04, respectively. The laser performance as a function of the number of 1.5-nm-thick $In_{0.1}Ga_{0.9}N$ well layers with variant indium composition in 3.0-nm-thick InGaN barriers is shown in Fig. 2.4. It is found that the lowest threshold current can be obtained when the number of well layers is two. However, when the indium composition in InGaN barriers is beyond 0.03,

the lowest threshold current is obtained when the number of well layers is three.

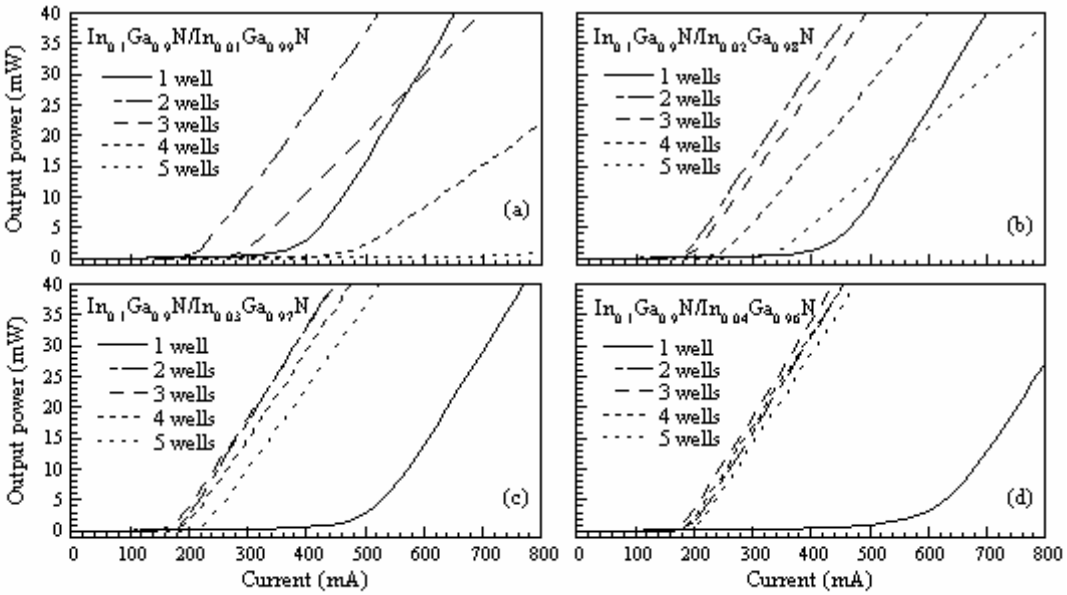


Fig. 2.4. Laser performance as a function of the number of well layers with variant indium composition in InGaN barriers.

The cause of this phenomenon may be due to that the thickness of well layers is narrow, and that when the indium composition in InGaN barriers is increased, the depth of $In_{0.1}Ga_{0.9}N$ well layers becomes too shallow to confine more carriers. In other words, more electrons can be confined in InGaN well layers with the increase of the number of InGaN well layers. The laser performance of SQW LD becomes worse when the indium composition in InGaN barrier increases, which may be due to that the amount of carriers confined in InGaN well layer is decreased. However, the slope efficiency of SQW LD is always higher than that of MQW LDs, and

the slope efficiency of DQW LD becomes the highest when compared with SQW and other MQW LDs if the indium composition in InGaN barriers is 0.04.

Table 2.1. Laser emission wavelength and optimization design of the number of well layers as functions of the thickness of $In_{0.1}Ga_{0.9}N$ well layers and the indium composition in InGaN barriers.

| $In_{0.1}Ga_{0.9}N$ / $In_yGa_{1-y}N$ | | y = 0.01 | y = 0.02 | y = 0.03 | y = 0.04 |
|---|---|---|---|---|---|
| Thickness of well layer (nm) | 1.5 | 396.1 nm (DQW) | 397.9 nm (DQW) | 399.7 nm (DQW) | 401.8 nm (TQW) |
| | 2.0 | 402.0 nm (SQW) | 403.2 nm (DQW) | 404.5 nm (DQW) | 406.0 nm (DQW) |
| | 2.5 | 406.1 nm (SQW) | 407.0 nm (SQW) | 408.0 nm (DQW) | 409.1 nm (DQW) |
| | 3.0 | 409.2 nm (SQW) | 409.8 nm (SQW) | 410.6 nm (DQW) | 411.4 nm (DQW) |
| | 3.5 | 411.5 nm (SQW) | 412.0 nm (SQW) | 412.5 nm (SQW) | 413.2 nm (DQW) |
| | 4.0 | 413.3 nm (SQW) | 413.7 nm (SQW) | 414.1 nm (SQW) | 414.6 nm (DQW) |
| | 4.5 | 414.7 nm (SQW) | 415.0 nm (SQW) | 415.3 nm (SQW) | 415.7 nm (S&DQW) |

By varying the thickness of $In_{0.1}Ga_{0.9}N$ well layers from 2.0 to 4.5 nm and the indium composition in InGaN barriers from 0.01 to 0.04, the laser emission wavelength can be obtained from 402.0 to 415.7 nm, which are listed in Table 2.1. It is noteworthy that, the laser emission wavelengths are all below 420 nm; hence the lowest threshold current should be obtained when the number of well layers is two according to the experimental

demonstration of Nakamura *et al*. However, when the thickness of InGaN well layers is varied from 2.0 to 4.5 nm while fixing the indium composition in InGaN barriers at 0.01, the lowest threshold current and the highest slope efficiency can be obtained when the number of well layers is one.

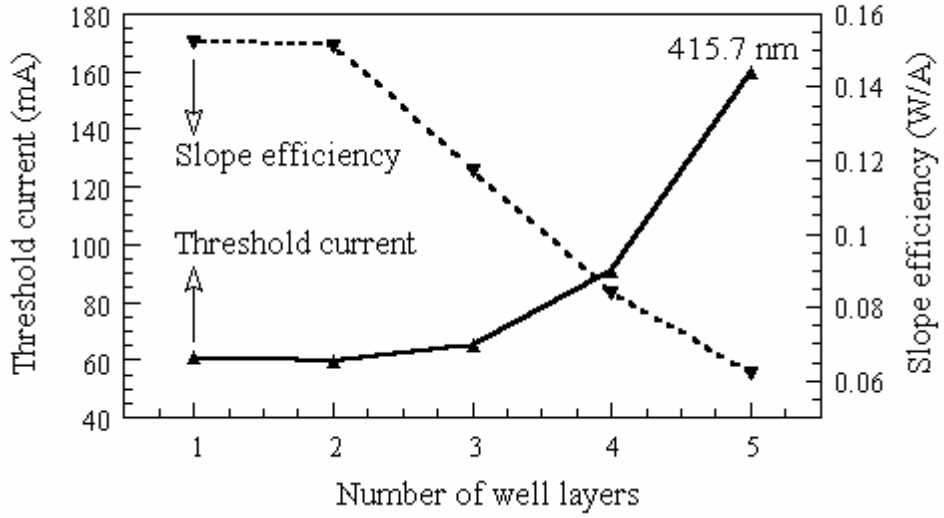


Fig. 2.5. Laser performance of 415.7-nm LD as a function of the number of well layers.

It is also noteworthy that, when the laser emission wavelength is 415.7 nm, which corresponds to the design of the active region containing 4.5-nm-thick $In_{0.1}Ga_{0.9}N$ well layers sandwiched between 9.0-nm-thick $In_{0.04}Ga_{0.96}N$ barriers, the lowest threshold current and highest slope efficiency can be obtained when the number of well layers is either one or two. Laser performance of 415.7-nm LD as a function of the number of well layers is shown in Fig. 2.5. A lowest threshold current of about 60 mA, which corresponds to the threshold current density of 1.2 kA/cm$^2$, and

highest slope efficiency of about 15.2% are obtained when the number of well layers is either one or two. When the number of well layers is increased, the laser performance decreases rapidly.

As indicated in Fig. 2.6, it is evident that the gain of n-side quantum wells becomes negative with increase of the number of InGaN well layers. Figure 2.7 shows the stimulated recombination rate for variant designs of the number of 4.5-nm-thick $In_{0.1}Ga_{0.9}N$ well layers sandwiched between 9.0-nm-thick $In_{0.04}Ga_{0.96}N$ barriers in 415.7-nm LD. The stimulated recombination rate of n-side quantum wells becomes negative when the number of $In_{0.1}Ga_{0.9}N$ well layers is increased beyond three. Negative stimulated recombination rate of quantum well layers indicates that it does not contribute to light emitting; it absorbs the photons created from p-side well layers instead. Therefore, one can imagine that the laser performance deteriorates when the number of well layers is increased.

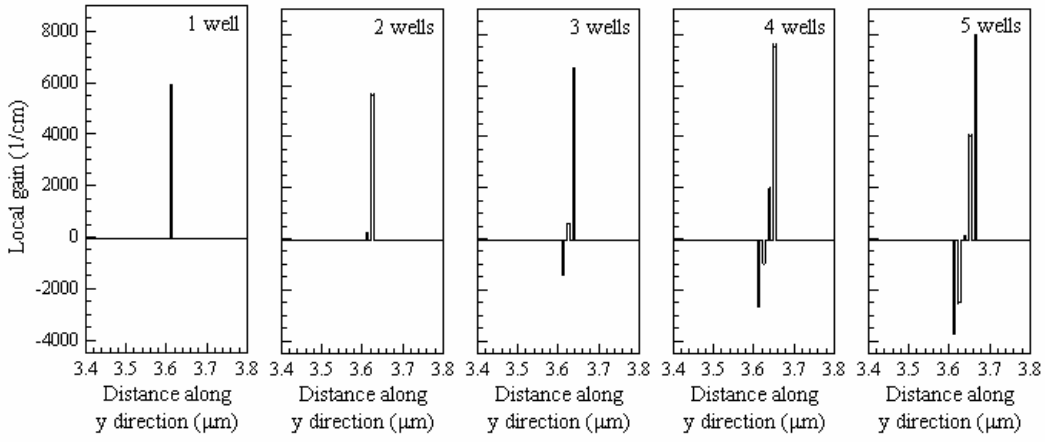


Fig. 2.6. Local gains for variant designs of the number of 4.5-nm-thick $In_{0.1}Ga_{0.9}N$ well layers sandwiched between 9.0-nm-thick $In_{0.04}Ga_{0.96}N$ barriers.

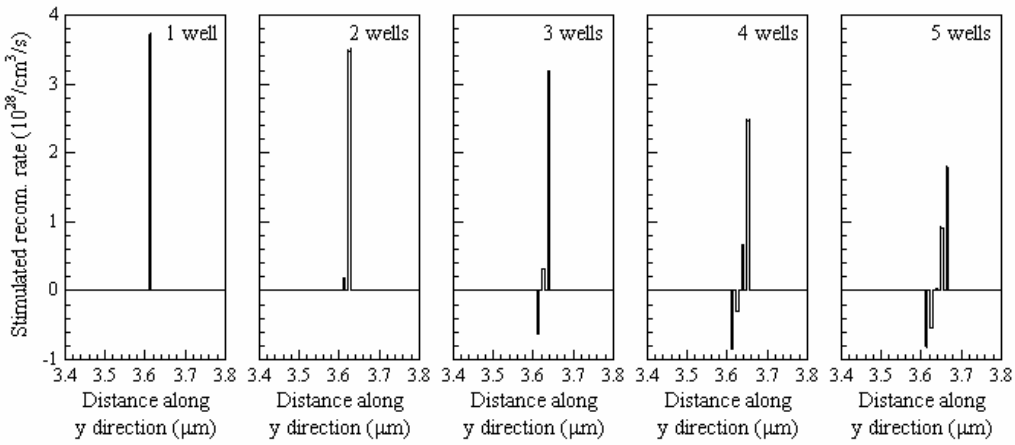


Fig. 2.7. Stimulated recombination rates for variant designs of the number of 4.5-nm-thick $In_{0.1}Ga_{0.9}N$ well layers sandwiched between 9.0-nm-thick $In_{0.04}Ga_{0.96}N$ barriers.

The above numerical simulation results seem different from the experimental results demonstrated by Nakamura *et al*. The optimization design of the number of $In_{0.1}Ga_{0.9}N$ well layers is choppy when the emission wavelength is in a range from 396.1 to 415.7 nm by varying the thickness of $In_{0.1}Ga_{0.9}N$ well layers and the indium composition in InGaN barriers. Nevertheless, there is a tendency that when the active region contains two quantum well layers, relatively low threshold current can be obtained when the thickness of well layers becomes narrower with increase of the indium composition in InGaN barriers.

In other words, when the thickness of $In_{0.1}Ga_{0.9}N$ well layers is increased and the indium composition in InGaN barriers is decreased, the lowest threshold current can be obtained when the number of well layers is one. The above simulation results may be due to that the conduction

band-offset value between InGaN and GaN heterolayers is small, while the valence band-offset value between InGaN and GaN heterolayers is large. Hence, it is difficult for holes to accumulate into the n-side quantum well layers. When the active region contains multiple quantum well layers, there are nearly no holes in n-side well layers to combine with electrons. Besides, since the hole effective mass is always larger than the electron effective mass, the hole mobility is relatively small. When holes travel from the p-side layers to the most p-side well layers, it is difficult for them to reach the n-side well layers. Therefore, it can be found that most holes are confined in the most p-side well layers when the active region of the LD is designed as MQW structure. This phenomenon can be regarded as "Inhomogeneous Hole Distribution".

The phenomenon of inhomogeneous hole distribution may become more serious when the thickness of $In_{0.1}Ga_{0.9}N$ well layers becomes wider, which is due to that the wider thickness of well layers, the more holes are confined in the most p-side well layer when injection current remains unchanged. Therefore, SQW LD can have better laser performance when the thickness of well layers becomes wider and the indium composition in InGaN barrier becomes larger. As an example, the laser performance of the 414.7-nm LD is discussed. The active region of 414.7-nm LD consists of 4.5-nm-thick $In_{0.1}Ga_{0.9}N$ wells and 9.0-nm-thick $In_{0.01}Ga_{0.99}N$ barriers.

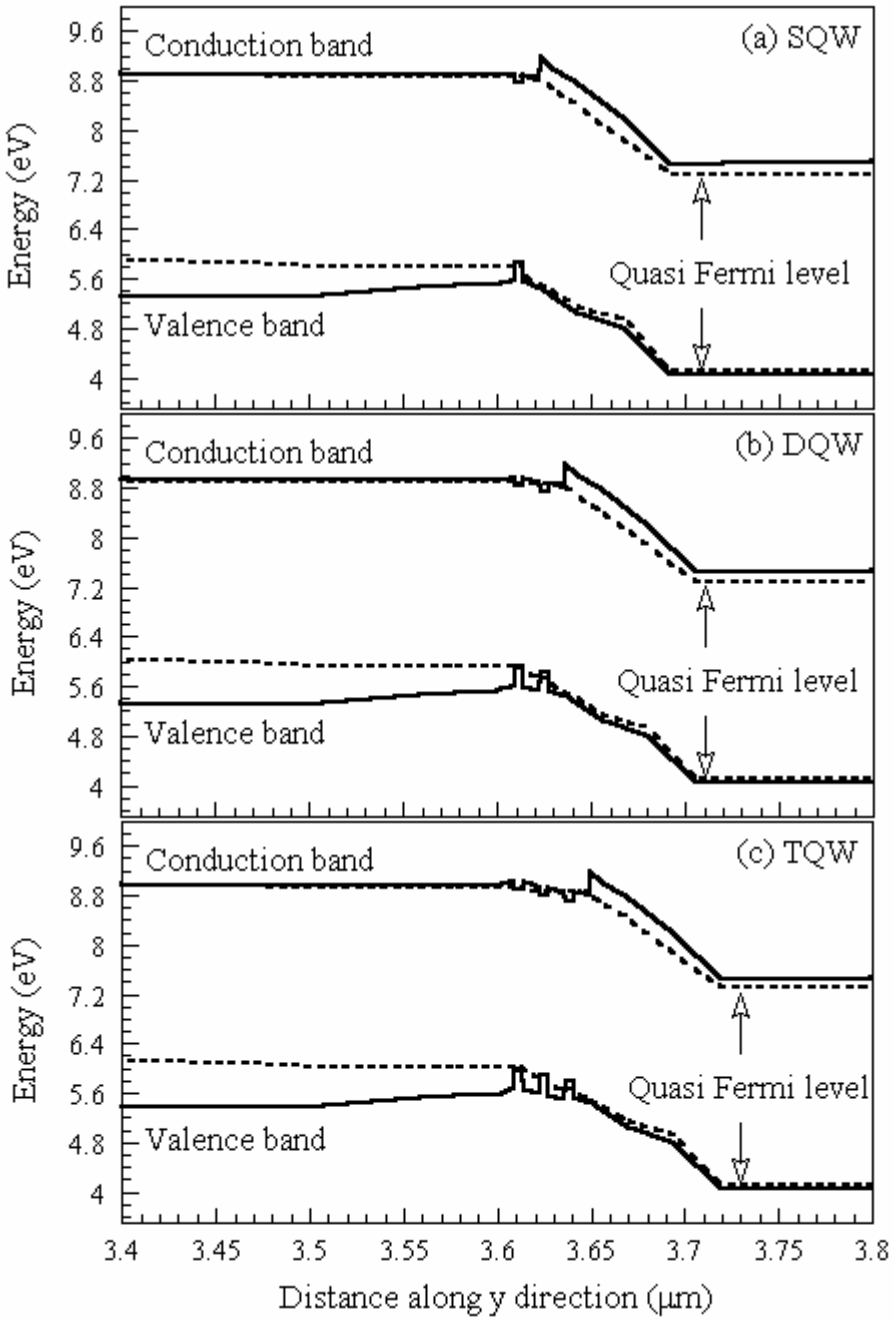


Fig. 2.8. Energy band diagrams for variant numbers of $In_{0.1}Ga_{0.9}N$ well layers.

Figure 2.8 shows the energy band diagrams of variant designs of the

number of $In_{0.1}Ga_{0.9}N$ well layers. As shown in the energy band diagram of 414.7-nm SQW LD, the upper quasi Fermi level is above the conduction band edge of quantum well layer, and the lower quasi Fermi level is under the valence band edge of well layers. It means that most electrons and holes are confined in the quantum well layer. However, the lower quasi Fermi level almost touches the valence band edge of n-side quantum well layers of DQW LDs, which indicates that there are few holes confined in the most n-side quantum well layers, and the lasing contribution of the most n-side quantum well layers may be inconspicuous.

As indicated in the energy band diagrams, a portion of the electrons may be confined in the dip, which is brought between the most p-side barrier and the $Al_{0.2}Ga_{0.8}N$ blocking layer, because the upper quasi Fermi level is a little above the conduction band. Even though the $Al_{0.2}Ga_{0.8}N$ layer can block most electrons to reduce the overflow to the p-side layers, more electrons are heaped in this dip. As shown in Fig. 2.8 (c), the lower quasi Fermi level is above the band edge of the most n-side quantum well layer. Hence, there are very few holes confined in the most n-side well layer. Evidently, the laser performance will become worse when the number of InGaN well layers is increased. The laser performance of 414.7-nm SQW, DQW, and TQW LDs are shown in Fig. 2.9. It is obvious that SQW LD has the best laser performance when compared with DQW and TQW LDs. When the active region contains four and five quantum wells, laser action cannot be activated at an injection current of 1000 mA,

which corresponds to a current density of 20 kA/cm$^2$.

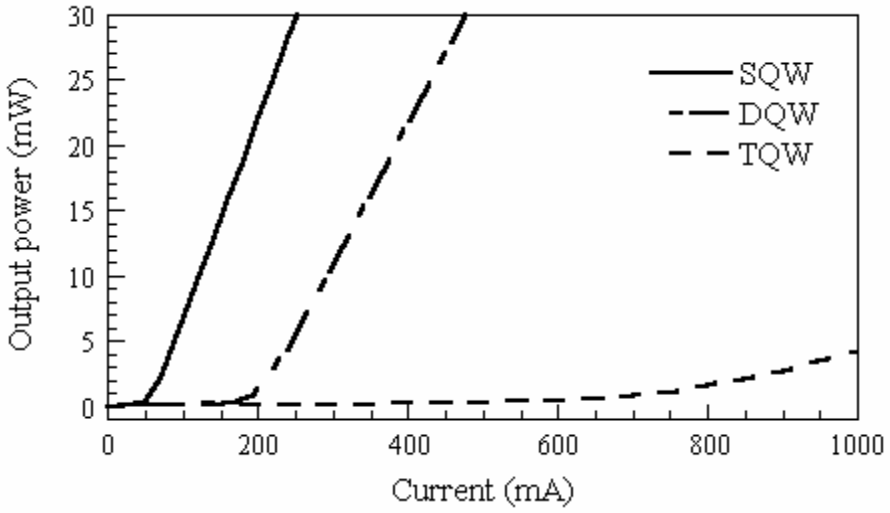


Fig. 2.9. Laser performance of 414.7-nm SQW, DQW, and TQW LDs.

### 2.3.2 $In_{0.15}Ga_{0.85}N/In_yGa_{1-y}N$ Design

Next, the optimization design of the number of $In_{0.15}Ga_{0.85}N$ well layers when the indium composition in InGaN barrier is varied from 0.01 to 0.06 is studied. When the indium composition in InGaN barriers is equal to 0.01 with the thickness of well layers varied from 1.5 to 4.5 nm, the lowest threshold current and highest slope efficiency can be obtained when the number of $In_{0.15}Ga_{0.85}N$ well layers is one. In the mean time, when the thickness of well layers is fixed at 1.5 nm, SQW LD can have the best laser performance when the indium composition in InGaN barriers is varied from 0.02 to 0.03.

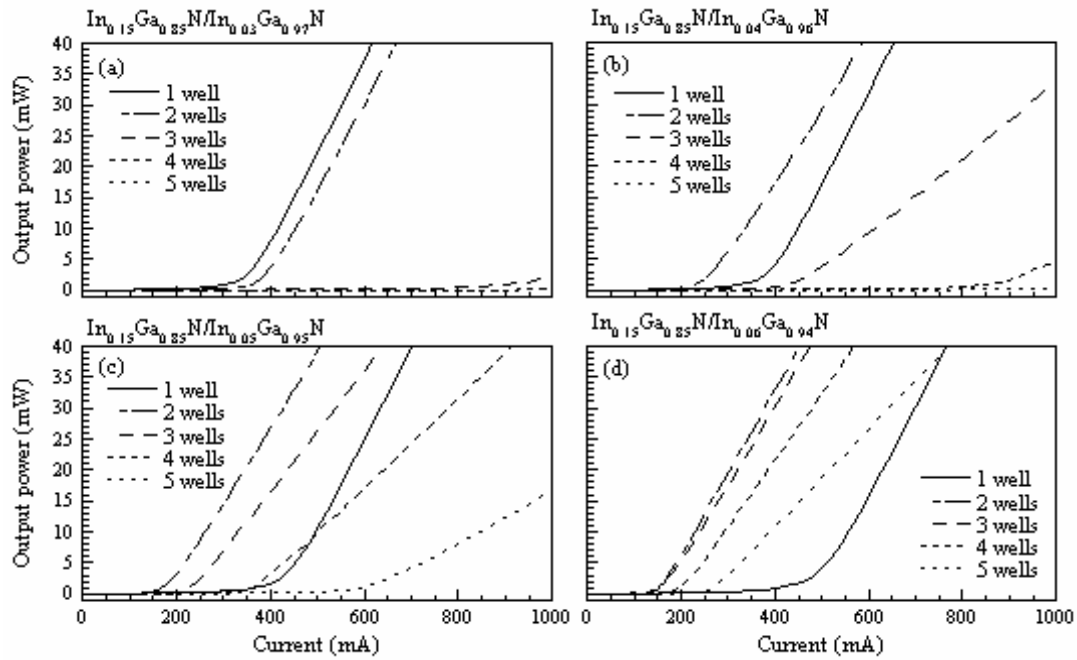


Fig. 2.10. Laser performance of $In_{0.15}Ga_{0.85}N$ well layers sandwiched between InGaN barriers, of which the In composition is varied from 0.03 to 0.06, as a function of the number of well layers.

Figure 2.10 shows the laser performance of 1.5-nm-thick $In_{0.15}Ga_{0.85}N$ well layers sandwiched between 3.0-nm-thick InGaN barriers, in which the indium composition is varied from 0.03 to 0.06, as a function of the number of well layers. Laser emission wavelengths under these four designs are 420.7, 422.3, 424.0, and 425.9 nm, respectively. The thickness of $In_{0.15}Ga_{0.85}N$ well layers is fixed at 1.5 nm for this specific study. When the indium composition in InGaN barriers is equal to 0.03, the lowest threshold current can be obtained when the number of well layers is one. However, it changes abruptly when the indium composition in InGaN barriers is beyond 0.04. It means that when the indium composition in

InGaN barriers is more than 0.04, the lowest threshold current can be obtained when the number of well layers is two.

Table 2.2. Laser emission wavelength and optimization design of the number of well layers as functions of the thickness of $In_{0.15}Ga_{0.85}N$ well layers and the indium composition in InGaN barriers.

| $In_{0.15}Ga_{0.85}N$ / $In_yGa_{1-y}N$ | | y = 0.02 | y = 0.03 | y = 0.04 | y = 0.05 | y = 0.06 |
|---|---|---|---|---|---|---|
| Thickness of well layer (nm) | 1.5 | 419.1 nm (SQW) | 420.7 nm (SQW) | 422.3 nm (DQW) | 424.0 nm (DQW) | 425.9 nm (DQW) |
| | 2.0 | 427.7 nm (SQW) | 428.7 nm (SQW) | 429.8 nm (SQW) | 431.0 nm (DQW) | 432.3 nm (DQW) |
| | 2.5 | 433.6 nm (SQW) | 434.3 nm (SQW) | 435.1 nm (SQW) | 436.0 nm (SQW) | 436.9 nm (S&DQW) |
| | 3.0 | 437.9 nm (SQW) | 438.4 nm (SQW) | 439.0 nm (SQW) | 440.0 nm (SQW) | 440.3 nm (SQW) |
| | 3.5 | 441.0 nm (SQW) | 441.4 nm (SQW) | 441.9 nm (SQW) | 442.3 nm (SQW) | 442.9 nm (SQW) |
| | 4.0 | 443.4 nm (SQW) | 443.7 nm (SQW) | 444.1 nm (SQW) | 444.4 nm (SQW) | 444.9 nm (SQW) |
| | 4.5 | 445.3 nm (SQW) | 445.5 nm (SQW) | 445.8 nm (SQW) | 446.1 nm (SQW) | 446.4 nm (SQW) |

Laser emission wavelength and optimization of the number of $In_{0.15}Ga_{0.85}N$ well layers to obtain the lowest threshold current as functions of the thickness of well layers and the indium composition in InGaN barriers are listed in Table 2.2. Laser emission wavelength can be obtained from 427.7 to 446.4 nm by varying the thickness of well layers from 1.5 to 4.5 nm and the indium composition in InGaN barriers from 0.02 to 0.06.

Similar to the tendency observed in the above subsection, when the indium composition in InGaN barriers is increased with the decrease of the thickness of InGaN well layers, the lowest threshold current can be obtained when the number of InGaN well layers is two. For example, when the thickness of $In_{0.15}Ga_{0.85}N$ well layers is fixed at 2.0 nm and the In compositions in InGaN barriers are set to be 0.05 and 0.06, which correspond to the laser emission wavelength of 431.0 and 432.3 nm, the lowest threshold current is obtained when the number of well layers is two. As indicated in Table 2.2, 436.9-nm SQW and DQW LDs, corresponding to the design of 2.5-nm-thick $In_{0.15}Ga_{0.85}N$ wells sandwiched between 5.0-nm-thick $In_{0.06}Ga_{0.94}N$ barriers, have similar threshold currents and slope efficiencies. The laser performance of 436.9-nm LDs as a function of the number of well layers is shown in Fig. 2.11.

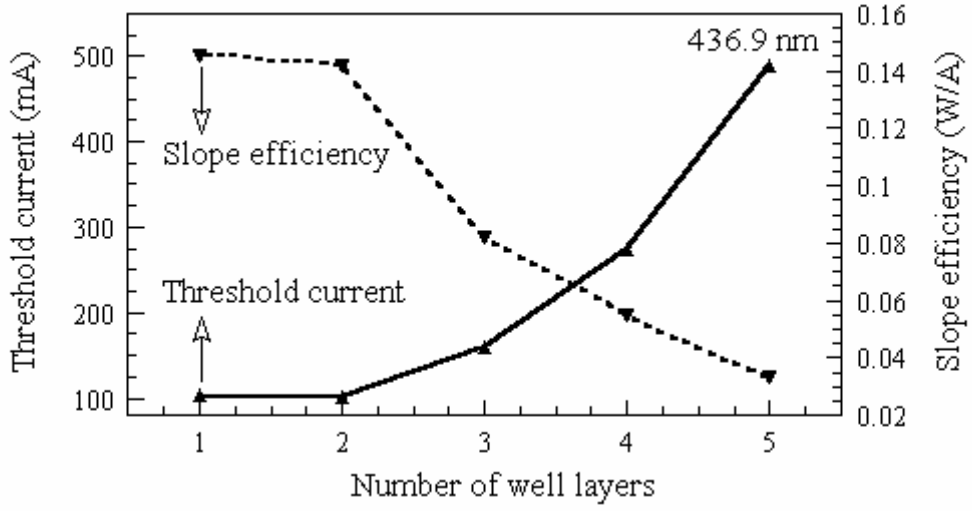


Fig. 2.11. Laser performance of 436.9-nm LDs as a function of the number of well layers.

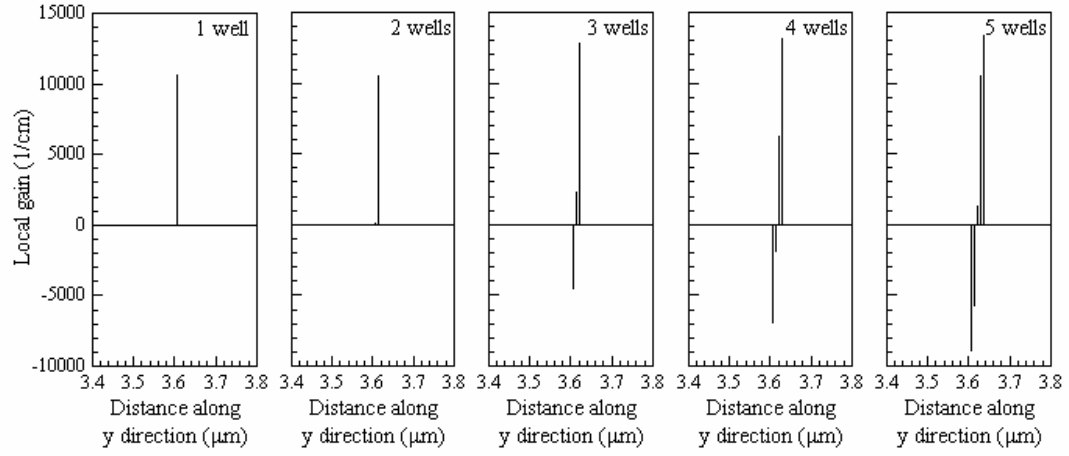


Fig. 2.12. Local gains for variant designs of the number of 2.5-nm-thick $In_{0.15}Ga_{0.85}N$ well layers sandwiched between 5.0-nm-thick $In_{0.06}Ga_{0.94}N$ barriers.

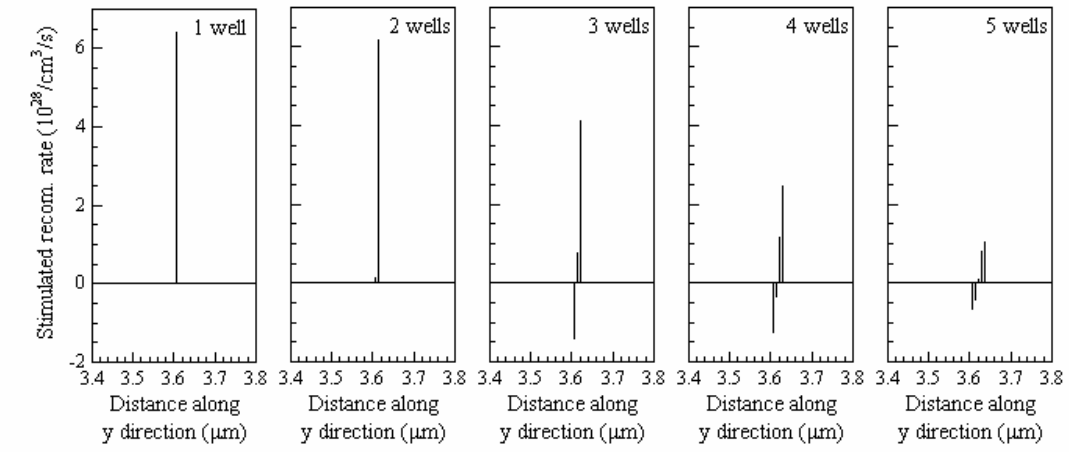


Fig. 2.13. Stimulated recombination rates of 436.9-nm LDs for variant designs of the number of 2.5-nm-thick $In_{0.15}Ga_{0.85}N$ well layers sandwiched between 5.0-nm-thick $In_{0.06}Ga_{0.94}N$ barriers.

Figure 2.12 shows the gain of the 436.9-nm LDs for variant designs of the number of 2.5-nm-thick $In_{0.15}Ga_{0.85}N$ well layers sandwiched between

5.0-nm-thick $In_{0.06}Ga_{0.94}N$ barriers. The gain of SQW LD is positive, so is DQW LD. However, the gain of n-side quantum well layer of DQW LD is relatively inconspicuous. When the number of well layers is more than three, it is evident that the gain provided by n-side quantum wells becomes negative. Figure 2.13 shows the stimulated recombination rate of the 436.9-nm LDs for variant designs of the number of 4.5-nm-thick $In_{0.15}Ga_{0.85}N$ well layers sandwiched between 5.0-nm-thick $In_{0.06}Ga_{0.94}N$ barriers. The stimulated recombination rate of the most p-side well layer drops vastly when the number of well layers is increased from one to five. Also, negative stimulated recombination rate appears in n-side quantum well layers when the number of well layers is more than three. The most n-side quantum well layer of TQW LD has the highest negative stimulated recombination rate when compared with the other MQW LDs. However, the positive stimulated recombination rate of p-side quantum well layers of TQW LD makes up for this negative effect. Therefore, the laser performance of the TQW LD is superior to those of the other MQW LDs. As mentioned in the above subsection, negative stimulated recombination rate indicates that the photons created from p-side quantum well layers will be absorbed. Therefore, it can be expected that SQW and DQW LDs still can have better laser performance.

The above numerical simulation results seem that they obey the experimental results demonstrated by Nakamura *et al.* in general direction. The optimization design of the number of $In_{0.15}Ga_{0.85}N$ well layers is one

when the emission wavelength is beyond 433.6 nm by varying the thickness of $In_{0.15}Ga_{0.85}N$ well layers and the indium composition in InGaN barriers from 2.5 to 4.5 nm and from 0.02 to 0.06, respectively. Nevertheless, when the thickness of well layers is 2.0 nm and the indium composition in InGaN barriers is set to be 0.05 and 0.06, corresponding to the emission wavelength of 431.0 and 432.3 nm, the lowest threshold current can be obtained when the number of well layers is two. Nevertheless, the SQW LD still has the highest slope efficiency under these two designs.

Prior $In_{0.1}Ga_{0.9}N/In_yGa_{1-y}N$ SQW LD can have the lowest threshold current when the thickness of well layers is wide and the indium composition in InGaN barrier is low. In the analysis of $In_{0.15}Ga_{0.85}N/In_yGa_{1-y}N$ designs, it is shown that when the thickness of $In_{0.15}Ga_{0.85}N$ well layers is narrow, and the indium composition in InGaN barriers is high, the DQW LDs still have relatively low threshold currents. However, most SQW LDs with variant emission wavelengths can have better laser performance. It is due mainly to the fact that the inhomogeneous hole distribution is more severe in $In_{0.15}Ga_{0.85}N/In_yGa_{1-y}N$ LDs. The effect of inhomogeneous hole distribution in 445.3-nm LD, which corresponds to the design of 4.5-nm-thick $In_{0.15}Ga_{0.85}N$ wells sandwiched between 9.0-nm-thick $In_{0.02}Ga_{0.98}N$ barriers, is discussed herein.

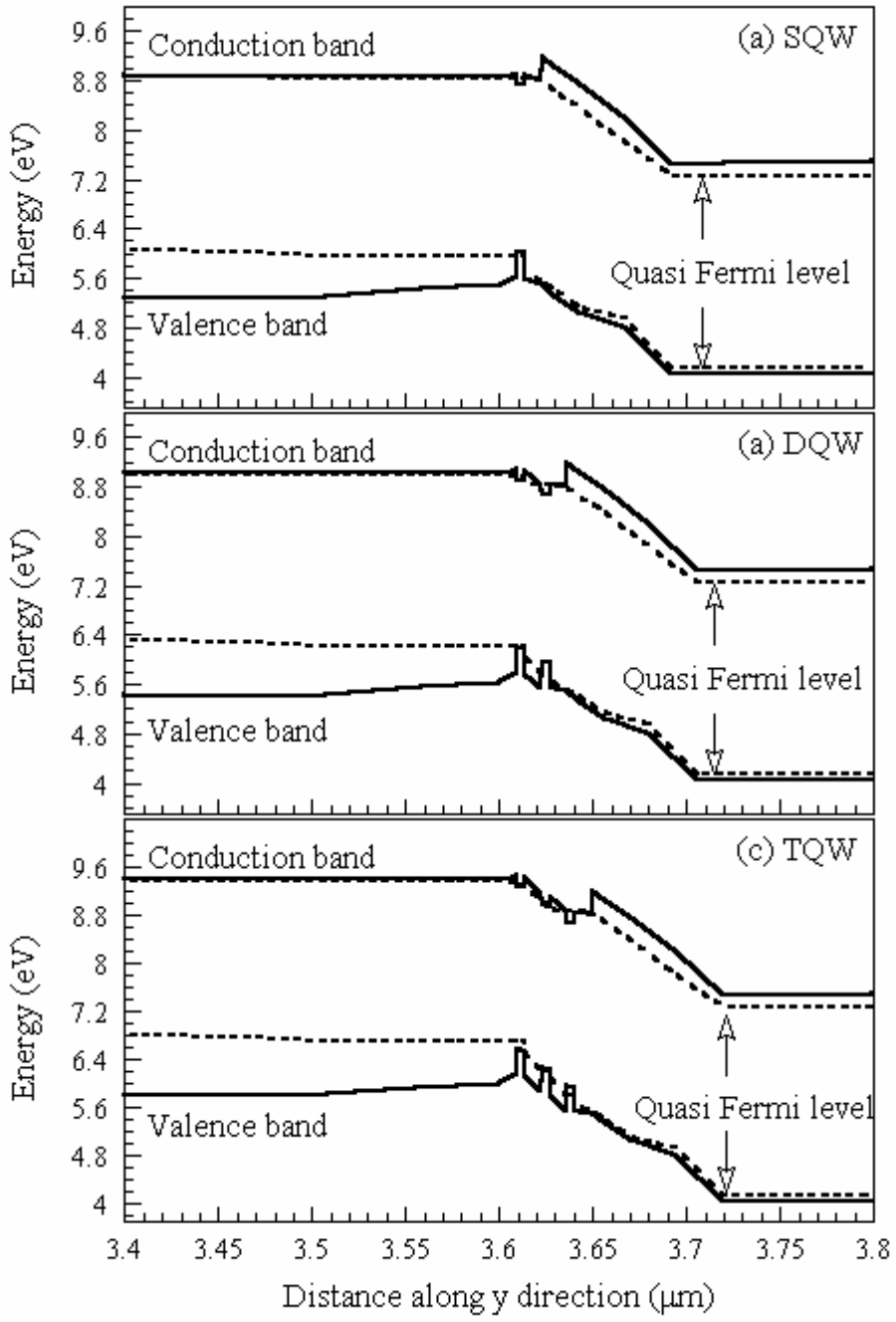


Fig. 2.14. Energy band diagrams of 445.3-nm SQW, DQW, and TQW LDs.

Figure 2.14 shows the energy band diagrams of 445.3-nm SQW, DQW,

and TQW LDs. Similar to the results shown in Fig.2.8, the upper quasi Fermi level is above the conduction band edge, and the lower quasi Fermi level is under the valence band edge for the situation of single quantum well layer. Most electrons and holes are confined in the quantum well layer. For DQW LD, the lower quasi Fermi level nearly touches the band edge of the n-side quantum well layer, which indicates that there are few holes confined in the n-side quantum well layer.

Comparing Fig. 2.8(c) with Fig. 2.14(c), both the lower quasi Fermi-levels are above the band edge of the most n-side quantum well layers. In other words, there are very few holes confined in the most n-side quantum well layers. Also, one can find that there is an apparent gap between the lower quasi Fermi level and the band edge of the most n-side quantum well in Fig. 2.14(c). It indicates that the phenomenon of inhomogeneous hole distribution is more serious in Fig. 2.14 than that in Fig. 2.8. In other words, the numerical simulation results indicate that the phenomenon of inhomogeneous hole distribution is more serious when the indium composition in InGaN well layers is increased to obtain long emission wavelength. Laser performance of the 445.3-nm SQW, DQW, and TQW LDs are shown in Fig. 2.15. SQW LD has the best laser performance when compared with MQW LDs as expected. Laser action is not observed for the TQW LD at the injection current of as high as 1000 mA.

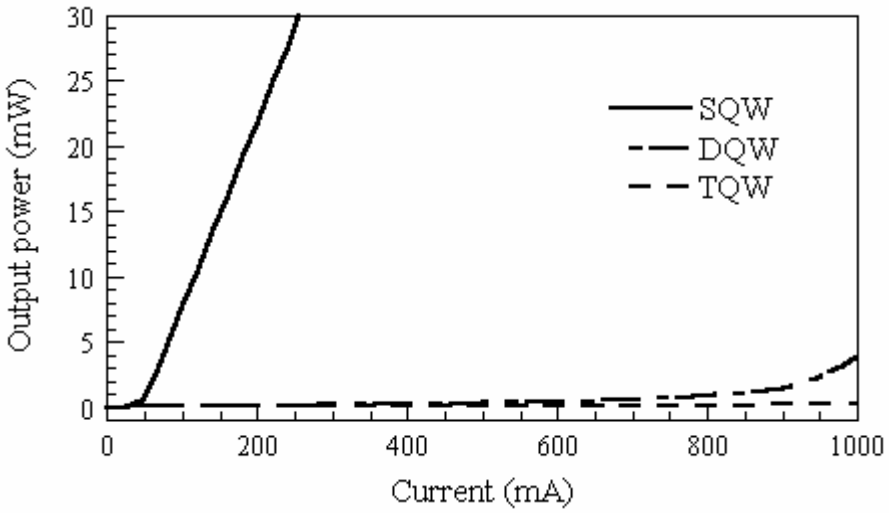


Fig. 2.15. Laser performance of 445.3-nm SQW, DQW, and TQW LDs.

### 2.3.3 $In_{0.2}Ga_{0.8}N/In_yGa_{1-y}N$ Design

Finally, the optimization design of the number of $In_{0.2}Ga_{0.8}N$ QW layers is studied when the indium composition in InGaN barriers is varied from 0.02 to 0.08. As described in the above subsection, in most situations, DQW LDs have the lowest threshold current when the indium composition in InGaN barriers is increased and the thickness of well layers is narrower. However, it is found that when the thickness of the $In_{0.2}Ga_{0.8}N$ well layers is as narrow as 1.5 nm, SQW LD can have the best laser performance when the indium composition in InGaN barriers is varied from 0.02 to 0.06 in the analysis of $In_{0.2}Ga_{0.8}N/In_yGa_{1-y}N$ designs. When the indium composition in InGaN barriers is further increased to 0.07 and 0.08, DQW LD has the lowest threshold current, even though SQW LD still has the highest slope

efficiency.

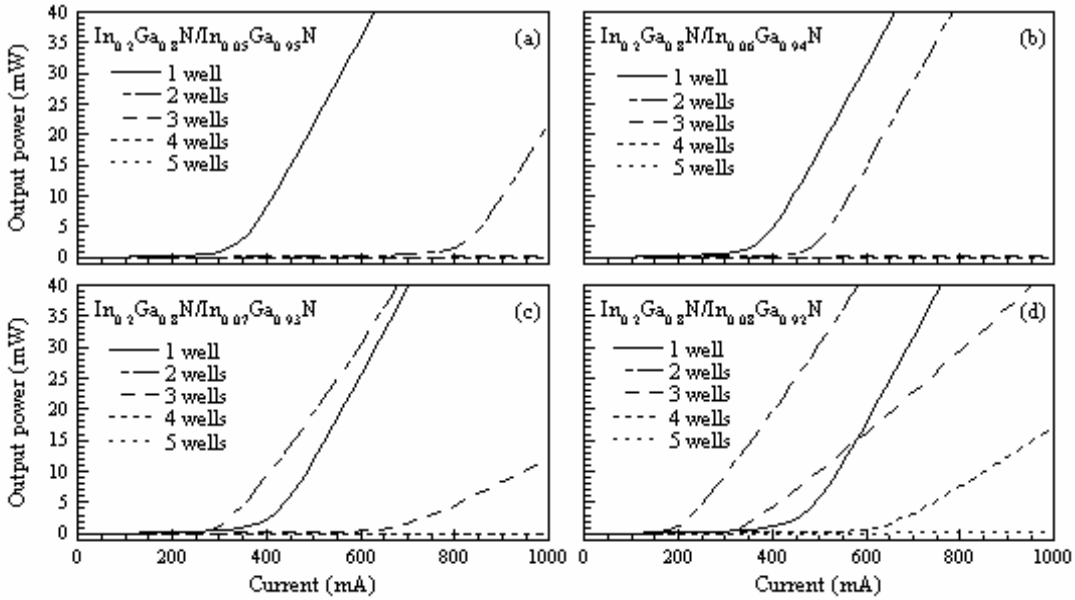


Fig. 2.16. Laser performance of $In_{0.2}Ga_{0.8}N$ well layers sandwiched between the InGaN barriers, of which the In composition is varied from 0.05 to 0.08, as a function of the number of well layers.

Figure 2.16 shows the laser performance of $In_{0.2}Ga_{0.8}N$ well layers sandwiched between InGaN barriers, of which the In composition is varied from 0.05 to 0.08, as a function of the number of well layers respectively. The laser emission wavelengths under these four designs are 446.8, 448.3, 450.0, and 451.7 nm, respectively. DQW LD has the lowest threshold current only when the indium composition in InGaN barriers is more than 0.07. The laser emission wavelength and optimization design of the number of $In_{0.15}Ga_{0.85}N$ well layers to obtain the lowest threshold current as functions of the thickness of $In_{0.2}Ga_{0.8}N$ well layers and the indium composition in InGaN barriers are listed in Table 2.3.

Table 2.3. Laser emission wavelength and optimization design of the number of well layers as functions of the thickness of $In_{0.2}Ga_{0.8}N$ well layers and the indium composition in InGaN barriers.

| $In_{0.2}Ga_{0.8}N$ / $In_yGa_{1-y}N$ | | y = 0.04 | y = 0.05 | y = 0.06 | y = 0.07 | y = 0.08 |
|---|---|---|---|---|---|---|
| Thickness of well layer (nm) | 1.5 | 445.3 nm (SQW) | 46.8 nm (SQW) | 448.3 nm (SQW) | 450.0 nm (DQW) | 451.7 nm (DQW) |
| | 2.0 | 456.2 nm (SQW) | 457.2 nm (SQW) | 458.2 nm (SQW) | 459.4 nm (SQW) | 460.6 nm (SQW) |
| | 2.5 | 463.7 nm (SQW) | 464.4 nm (SQW) | 465.1 nm (SQW) | 465.9 nm (SQW) | 466.8 nm (SQW) |
| | 3.0 | 469.0 nm (SQW) | 469.5 nm (SQW) | 470.0 nm (SQW) | 470.6 nm (SQW) | 471.3 nm (SQW) |
| | 3.5 | 472.9 nm (SQW) | 473.3 nm (SQW) | 473.7 nm (SQW) | 474.2 nm (SQW) | 474.6 nm (SQW) |
| | 4.0 | 475.9 nm (SQW) | 476.2 nm (SQW) | 476.5 nm (SQW) | 476.9 nm (SQW) | 477.2 nm (SQW) |
| | 4.5 | 478.2 nm (SQW) | 478.2 nm (SQW) | 478.7 nm (SQW) | 479.0 nm (SQW) | 479.3 nm (SQW) |

Undoubtedly, SQW LD always has the lowest threshold current and highest slope efficiency when the thickness of InGaN well layers is varied from 2.0 to 4.5 nm and the indium composition in InGaN barriers is varied from 0.04 to 0.08. It is worth to mention that SQW LD still has the best laser performance when the indium composition in InGaN barriers is 0.02 and 0.03, which are not listed in Table 2.3.

As discussed in last two subsections, in certain InGaN/InGaN LD structures the SQW and DQW LDs have similar laser performance. For examples, the SQW and DQW have similar threshold current and slope

efficiency under the situation when the 4.5-nm-thick $In_{0.1}Ga_{0.9}N$ well layers are sandwiched between 9.0-nm-thick $In_{0.04}Ga_{0.96}N$ barriers, and when the 2.5-nm-thick $In_{0.15}Ga_{0.85}N$ well layers are sandwiched between 5.0-nm-thick $In_{0.06}Ga_{0.94}N$ barriers. Notice that, it always appears when the indium composition in InGaN barriers is high, even though the thickness of InGaN well layers is uncertain. However, this phenomenon cannot be found in the analysis of $In_{0.2}Ga_{0.8}N/In_yGa_{1-y}N$ LD designs.

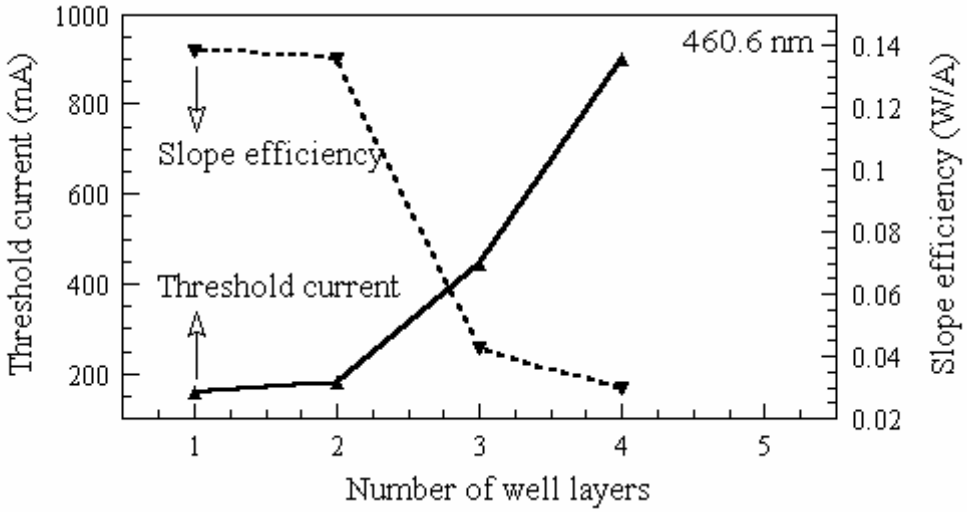


Fig. 2.17. Laser performance of 460.6-nm LD as a function of the number of well layers.

Laser performance of a 460.6-nm LD, corresponding to the design of the 2.0-nm-thick $In_{0.2}Ga_{0.8}N$ wells sandwiched between 4.0-nm-thick $In_{0.08}Ga_{0.92}N$ barriers, as a function of the number of well layers is discussed because the laser performance of SQW and DQW LDs are similar. Laser performance of a 460.6-nm LD as a function of the number

of well layers is shown in Fig. 2.17. The threshold currents and slope efficiencies of SQW and DQW LDs are 160 and 182 mA, which correspond to threshold current densities of 3.20 and 3.64 kA/cm$^2$, and 0.138 and 0.136 W/A, respectively. When the active region of 460.0-nm LD contains five periods of $In_{0.2}Ga_{0.8}N$ well layers, it cannot lase at an injection current of 1000 mA .

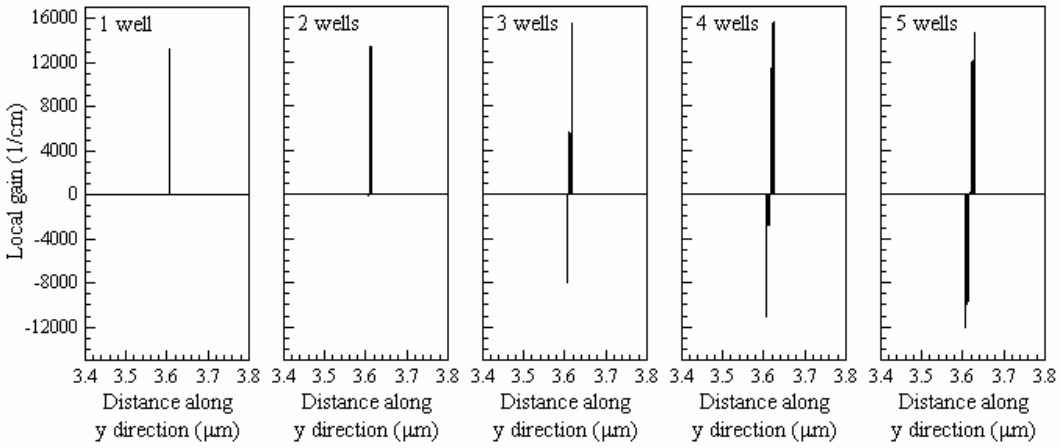


Fig. 2.18. Local gains of 460.6-nm LD for variant numbers of $In_{0.2}Ga_{0.8}N$ well layers.

The gains of 460.6-nm LD for variant numbers of $In_{0.2}Ga_{0.8}N$ well layers are shown in Fig. 2.18. P-side quantum well layers still have positive gain. However, the gain of n-side quantum well layers becomes negative when the number of well layers is more than three. Figure 2.19 shows the stimulated recombination rate of the 460.6-nm LD for variant numbers of $In_{0.2}Ga_{0.8}N$ well layers. The stimulated recombination rate of the most p-side quantum well layer drops vastly with increased number of well layers. Specifically, the stimulated recombination rate almost decreases to

zero when the number of well layers is five, which indicates that there is no laser action when the number of well layers is five at the injection current of 1000 mA.

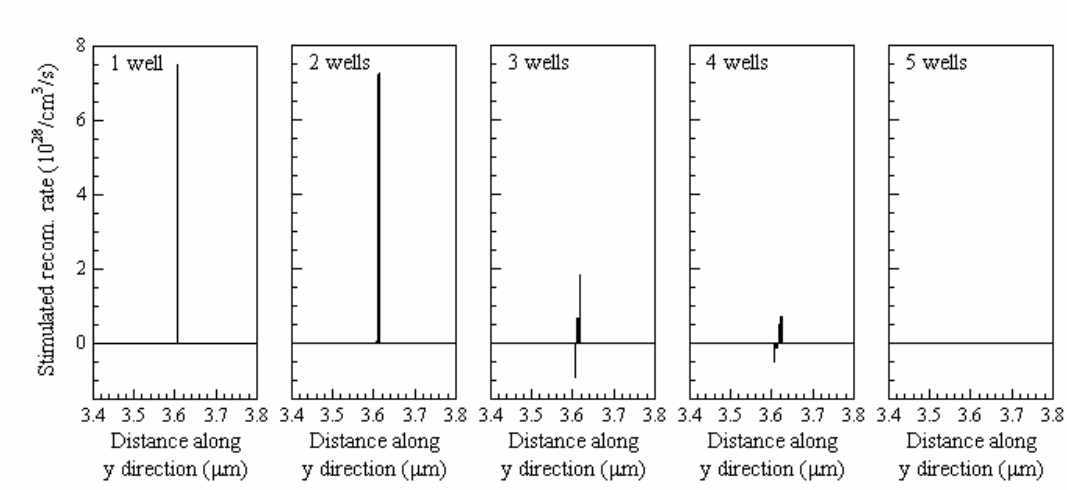


Fig. 2.19. Stimulated recombination rate of 460.6-nm LD for variant numbers of the $In_{0.2}Ga_{0.8}N$ well layers.

As depicted in Table 2.3, although lowest threshold current can be obtained in DQW LD when the indium compositions in InGaN barriers are 0.07 and 0.08 and the thickness of $In_{0.2}Ga_{0.8}N$ well layers is 1.5 nm, our simulation results are in good agreement with the experimental results demonstrated by Nakamura *et al*. Namely, when the emission wavelength is between 442.4 and 479.3 nm, the SQW LDs usually have the best laser performance when compared with DQW and other MQW LDs.

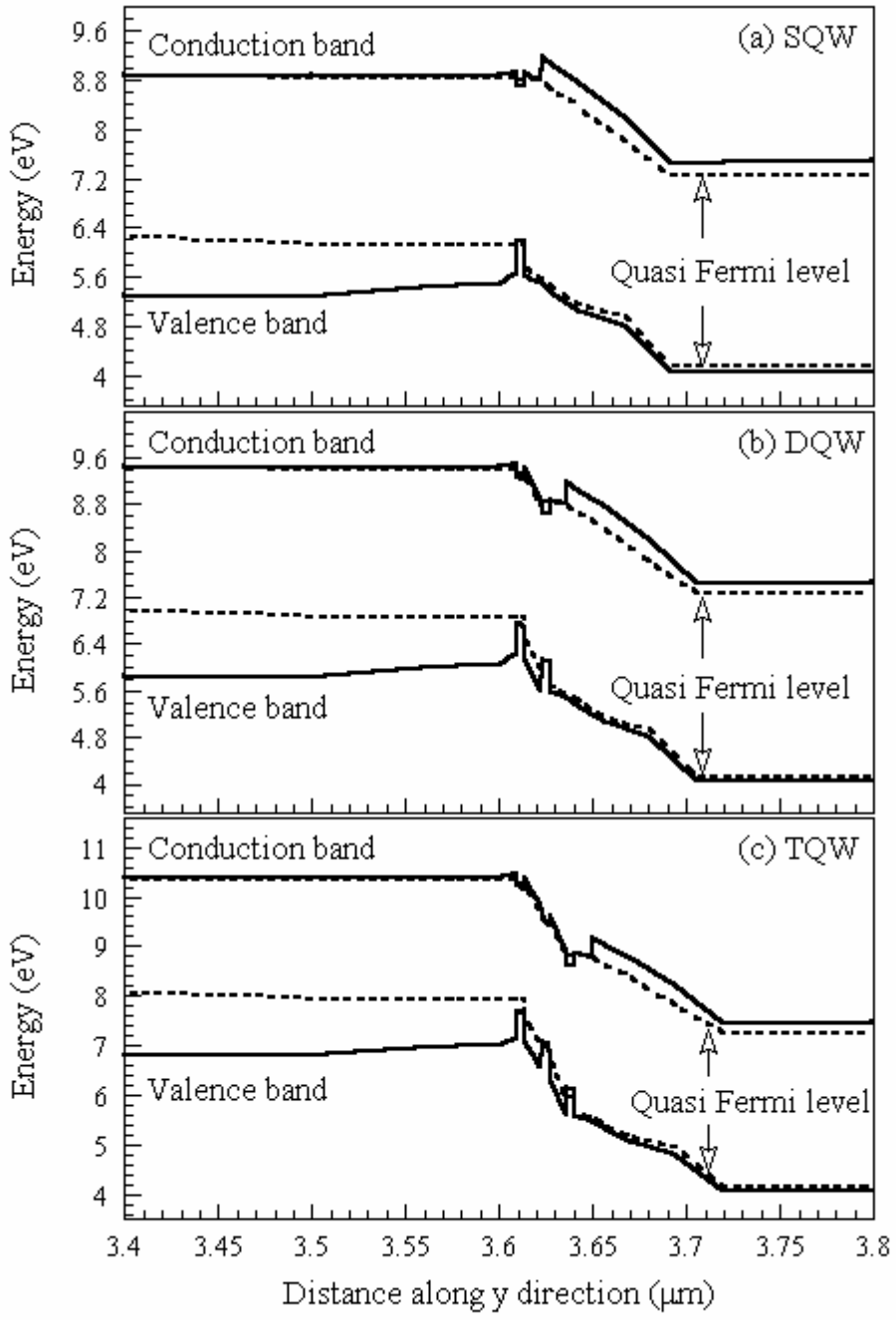


Fig. 2.20. Energy band diagrams of 477.8-nm SQW, DQW, and TQW LDs.

The phenomenon of inhomogeneous hole distribution is serious when

the indium composition in InGaN well layers is high. To discuss the phenomenon of inhomogeneous hole distribution of $In_{0.2}Ga_{0.8}N/In_yGa_{1-y}N$ laser structure, a 477.8-nm LD, which corresponds to the design of 4.5-nm-thick $In_{0.2}Ga_{0.8}N$ well layers sandwiched between 9.0-nm-thick $In_{0.02}Ga_{0.98}N$ barriers, is chosen. Figure 2.20 shows that the energy band diagrams of 477.8-nm SQW, DQW, and TQW LDs. It is evident that most electrons and holes are confined in the most p-side quantum well layers of 477.8-nm SQW, DQW, and TQW LDs. However, the lower quasi Fermi levels are above the valence band edge of the most n-side quantum well layer of DQW and TQW LDs. Therefore, there are few holes in the most n-side quantum well layers of 477.8-nm DQW and TQW LDs.

Comparing Fig. 2.20 with Fig. 2.14, it is found that the phenomenon of inhomogeneous hole distribution in Fig. 2.20 is more severe than that in Fig. 2.14. One of the reasons may be that the strain induced by the lattice mismatch between InN and GaN of InGaN well layers gets larger with the increase of the indium composition in well layers when the indium composition in InGaN barriers remains unchanged. A large value of strain will bend the conduction band and valence band apparently, and it may result in the phenomenon of inhomogeneous hole distribution. Another possible reason, which have been mentioned in Fig. 2.7, is that both valence band-offset value between InGaN and GaN hetero layers and hole effective mass are large. Therefore, when holes are confined in the most p-side quantum well layer, it is difficult for them to transport to the n-side

well layers. Therefore, there are relatively more holes confined in the most p-side quantum well layer and few holes confined in n-side well layers when the indium composition in well layers is increased at the same level of injection current. Laser performance of 477.8-nm SQW, DQW, and TQW LDs are shown in Fig. 2.21. As expected, the SQW LD still has the best laser performance when compared with MQW LDs. TQW LD is hard to lase at an injection current of 1000 mA due to the problem of inhomogeneous hole distribution.

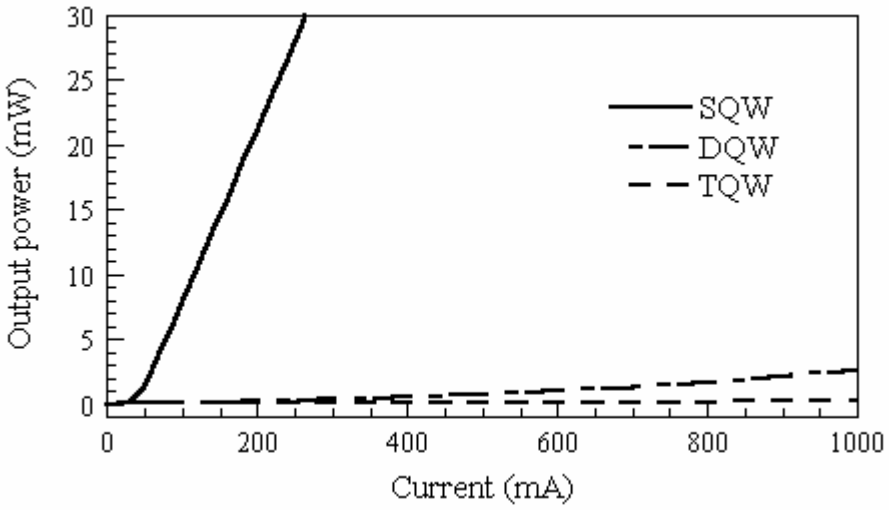


Fig. 2.21. Laser performance of 477.8-nm SQW, DQW, and TQW LDs.

In summary, the optimization design of the number of well layers in InGaN/InGaN LD as a function of emission wavelength in a range from 396.1 to 479.3 nm by varying the indium composition in InGaN well layers and barriers and the thickness of well layers is studied. Numerical simulation results suggest that when the indium composition in InGaN well

layer is less than 0.15, under most circumstances, the SQW LDs have the lowest threshold current when the indium composition in InGaN barriers is small and the thickness of well layers is increased.

In general, the numerical simulation results obtained in this work are in good agreement with the experimental results demonstrated by Nakamura *et al*. When the indium composition in InGaN well layers is 0.1, laser emission wavelength can be varied from 396.1 to 415.3 nm when the indium composition in InGaN barriers is in a range from 0.01 to 0.04, and the thickness of well layers is increased from 1.5 to 4.5 nm. The simulation results show that DQW LDs have the lowest threshold current when the indium composition in InGaN barriers is increased and the thickness of well layers is decreased. Nevertheless, it needs to be emphasized that 415.7-nm SQW and DQW LDs, which corresponds to the design of 4.5-nm-thick InGaN quantum well layers sandwiched between 9.0-nm-thick barriers, have the same lowest threshold current and highest slope efficiency. In other words, the $In_{0.1}Ga_{0.9}N/In_yGa_{1-y}N$ DQW LD have the lowest threshold current and highest slope efficiency when the indium composition in InGaN barriers is more than 0.04 for variant thickness of well layers.

When the indium composition in InGaN well layers is 0.15, the emission wavelength can be varied from 419.1 to 446.4 nm when the indium composition in InGaN barriers is in a range from 0.02 to 0.04, and the thickness of well layers is increased from 1.5 to 4.5 nm. It is concluded

that most $In_{0.15}Ga_{0.85}N/In_yGa_{1-y}N$ SQW LDs have the best laser performance. However, when the indium composition in InGaN barriers is increased to more than 0.04 and the thickness of well layers is decreased to less than 2.5 nm, DQW LDs can have the lowest threshold current.

Also, the 436.9-nm SQW and DQW LDs, which correspond to the design of 2.5-nm-thick $In_{0.15}Ga_{0.85}N$ quantum well layers sandwiched between 5.0-nm-thick $In_{0.06}Ga_{0.94}N$ barriers, have similar laser performance. When the thickness of InGaN well layers is fixed at 2.5 nm, the DQW LDs can have the lowest threshold current when the indium composition in InGaN barriers is more than 0.06. However, the laser performance of SQW LDs is better than that of DQW LDs when the emission wavelength is increased in the analysis of the $In_{0.15}Ga_{0.85}N/In_yGa_{1-y}N$ designs.

When the indium composition in InGaN well layers is 0.2, the emission wavelength can be varied from 442.4 to 479.3 nm when the indium composition in InGaN barriers is in a range from 0.02 to 0.08, and the thickness of well layers is increased from 1.5 to 4.5 nm. Numerical simulation results suggest that the SQW LDs have the best laser performance when the emission wavelength becomes longer than 454.3 nm. Nevertheless, the DQW LDs have the lowest threshold current when the indium composition in InGaN barriers is beyond 0.07, and the thickness of $In_{0.2}Ga_{0.8}N$ well layers is 1.5 nm.

The phenomenon of inhomogeneous hole distribution becomes more severe when the indium composition in InGaN well layers is increased

from 0.1 to 0.2. In the following section, the phenomenon of inhomogeneous hole distribution of InGaN/InGaN MQW LDs is further studied.

## 2.4 Inhomogeneous Hole Distribution of InGaN/InGaN MQW LDs

Nakamura *et al.* demonstrated that the lowest threshold current was obtained when the number of InGaN well layers was two with an emission wavelength of 390 – 420 nm, and when the laser emission wavelength was increased beyond 435 nm, the lowest threshold current was obtained when the number of InGaN well layers was one. They believed that a high indium composition in InGaN well layers for the purpose of obtaining long emission wavelength would degrade the crystal quality of InGaN quantum well layers. An increase of the internal loss of LDs is resulted. In addition to the dissociation of InGaN well layers at a high growth temperature during crystal growth, simulation results also suggest that the cause of the above phenomena is attributed to the inhomogeneous hole distribution in quantum well layers. In other words, the phenomenon of inhomogeneous hole distribution plays an important role in the design of the number of InGaN well layers in InGaN/InGaN QW LDs, and it becomes more severe when the indium composition in InGaN well layers is increased to obtain long emission wavelengths.

The electron and hole concentration distribution along the junction plane of 414.7-nm, 445.3-nm, and 477.8-nm QW LDs are discussed in this section. In these three LDs the thickness of InGaN well layers and barriers are equal to 4.5 and 9.0 nm respectively. The indium compositions in InGaN/InGaN active region are 0.1/0.01, 0.15/0.02, and 0.2/0.02,

respectively. Figure 2.22 depicts the electron and hole concentration distributions of 414.7-nm, 445.3-nm, and 477.8-nm SQW LDs. The electron and hole concentrations in each quantum well layer are all higher than those in other regions, which indicates that most electrons and holes are confined in the active region effectively. However, one can find that there is a peak appearing in the right side of the active region in each of the three plots of electron concentration distributions. It is found that a portion of the electrons is confined in that region. As indicated in the energy band diagrams of 414.7-nm, 445.3-nm, and 477.8-nm SQW LDs, a dip between p-side InGaN barrier and AlGaN blocking layer is observed. Therefore, a portion of the electrons may pile up in this dip. The amount of electrons piled up in this dip is decreased when the emission wavelength is increased. The depth of quantum well is deeper when the indium composition in quantum well layer is increased to obtain long laser emission wavelength and the indium composition in InGaN barriers remains unchanged. Therefore, the amount of electrons confined in the quantum well layer is increased, and that piled up in this dip is decreased. Note that, the indium composition in 414.7-nm SQW InGaN barrier is 0.01 lower than that of 445.3-nm and 477.8-nm SQW LDs. There may be more electron piling up in this dip if the indium composition in 414.7-nm InGaN barrier is 0.02.

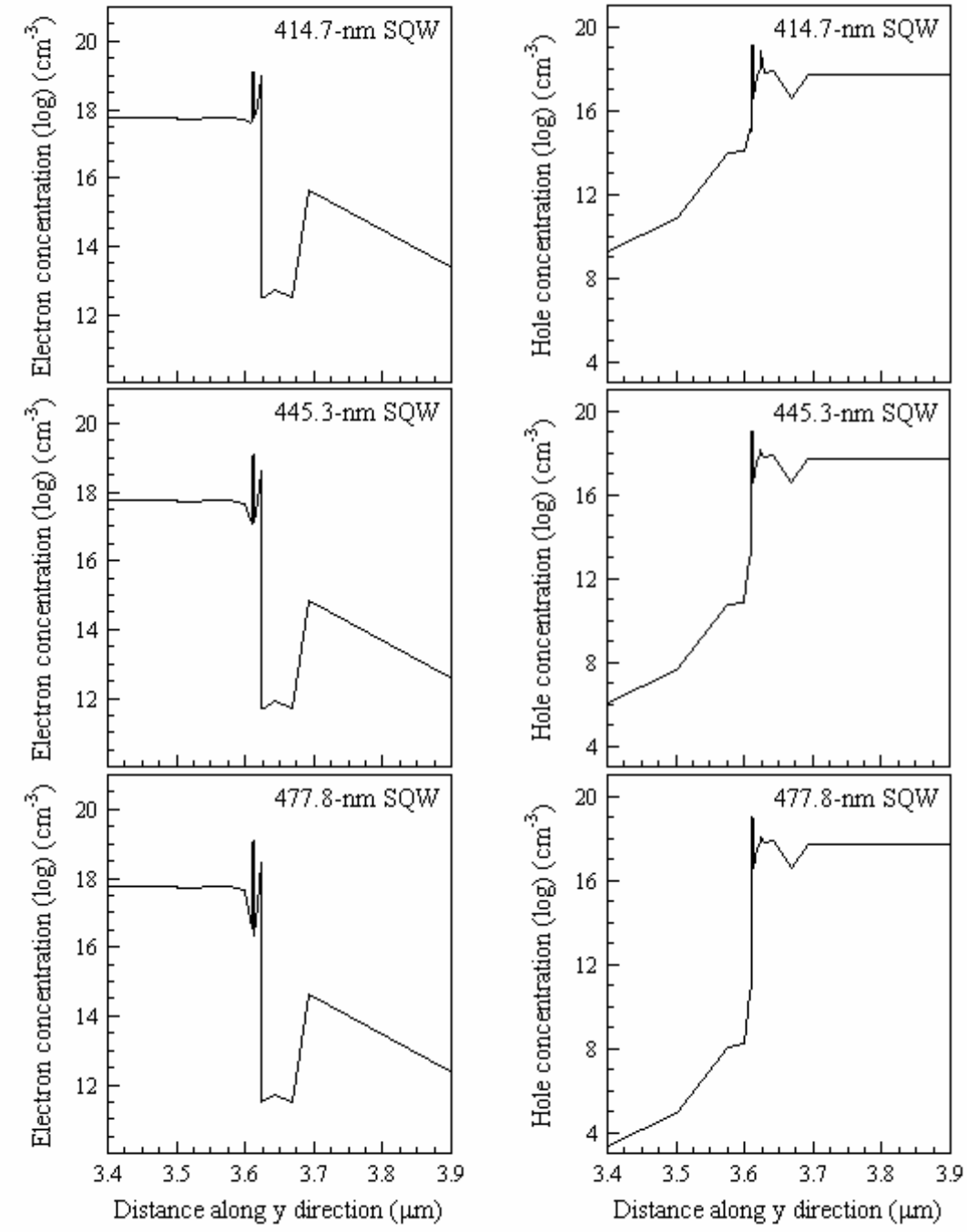


Fig. 2.22. Electron and hole concentration distributions of 414.7-nm, 445.3-nm, and 477.8-nm SQW LDs.

A peak appearing in the right side of the active region in each of the three plots of hole concentration distribution, especially in the plot of 414.7-nm SQW LD, can be found as well. As shown in the energy band diagram of 414.7-nm SQW LD, the lower quasi Fermi level almost touches the valence band at the position of the interface between p-side InGaN barrier and AlGaN blocking layer. Therefore, a portion of the holes may appear in this region. However, fewer holes are confined in this region when the emission wavelength is increased.

As depicted in Fig. 2.22, a dip can be found in each plot of electron and hole concentration distribution as well. Undoubtedly, this dip is corresponding to the position of AlGaN blocking layer in plot of electron concentration distribution, because the bandgap energy of AlGaN is higher than that of GaN and InGaN. There are few electrons confined in AlGaN blocking layer. However, the relatively shallow dip in each plot of hole concentration distribution does not correspond to the position of AlGaN blocking layer. It corresponds to the interface between the AlGaN blocking layer and the GaN cladding layer. This may be due to that there is only one data point to plot the hole concentration in this region.

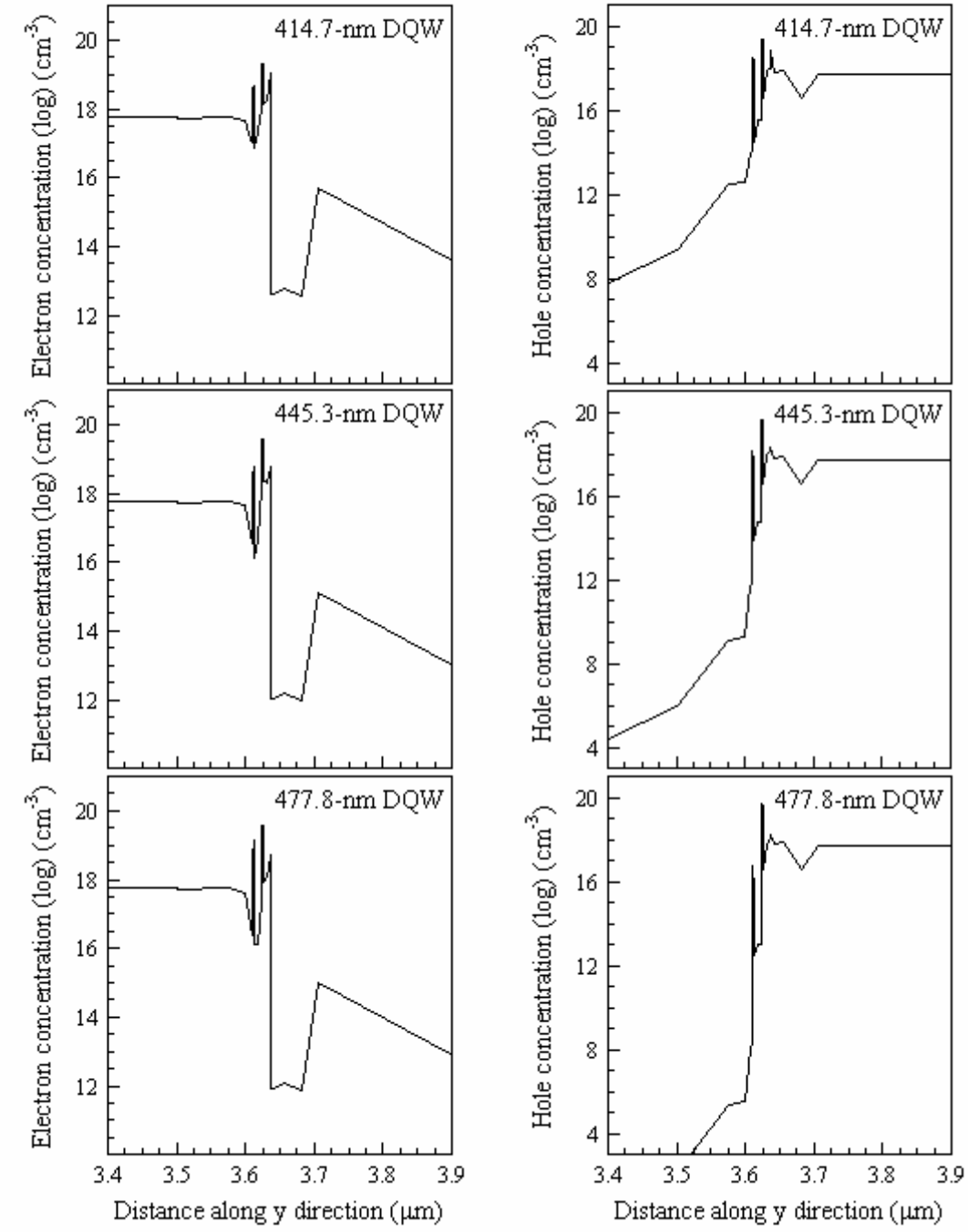


Fig. 2.23. Electron and hole concentration distributions of 414.7-nm, 445.3-nm, and 477.8-nm DQW LDs.

Figure 2.23 shows the electron and hole concentration distribution of 414.7-nm, 445.3-nm, and 477.8-nm DQW LDs. Simuilar phenomena are observed. One finds that more electrons are confined in p-side quantum well layer than that in n-side quantum well layer. Because the AlGaN blocking layer can block most electrons that tend to overflow to the p-side layers, more electrons pile up in p-side quantum well layer. Therefore, the electron concentration of p-side quantum well layer is higher than that of n-side quantum well layer. The amount of electrons confined in p-side quantum well layer is near decuple higher than that in n-side quantum well layer.

The phenomenon of inhomogeneous hole distribution is observed in each plot of hole concentration distribution. The inhomogeneous hole distribution of 414.7-nm DQW LD is not so severe. Nevertheless, the phenomenon becomes much serious when the emission wavelength is increased to 445.3 and 477.8 nm. The amount of holes confined in p-side quantum well layer is near half decuple higher than that in n-side quantum well layer for 414.7-nm DQW LD. When the emission wavelengths are 445.3 and 477.8 nm, the amount of holes confined in p-side quantum well layer is near thirty times and 1000 times higher than those in n-side quantum well layer, respectively. The value of hole concentration of 414.7-nm n-side quantum well layer is still higher than that of p-side layer. However, the value of hole concentration of 445.3-nm n-side quantum well layer is almost the same as that of p-side layers ($5\times10^{17}$ $cm^{-3}$), and the value

of hole concentration of 477.8-nm n-side quantum well layer drops apparently and is less than that of p-side layers. Note that, 445.3-nm DQW LD can still lase even though its threshold current is as high as 874 mA and its slope efficiency is as low as 0.03. However, 477.8-nm DQW LD cannot lase at an injection current of 1000 mA.

The electron and hole concentration distribution of 414.7-nm, 445.3-nm, and 477.8-nm TQW LDs are shown in Fig. 2.24. More electrons are confined in the most p-side quantum well layer in each plot of the electron concentration distribution. The amount of electrons confined in the most p-side quantum well layer is near decuple higher than that in another two quantum well layers in each plot of electron concentration distribution. The value of electron concentration of each quantum well layer in each plot of electron concentration distribution is higher than that of n-side layers ($1.0\times10^{18}$ $cm^{-3}$).

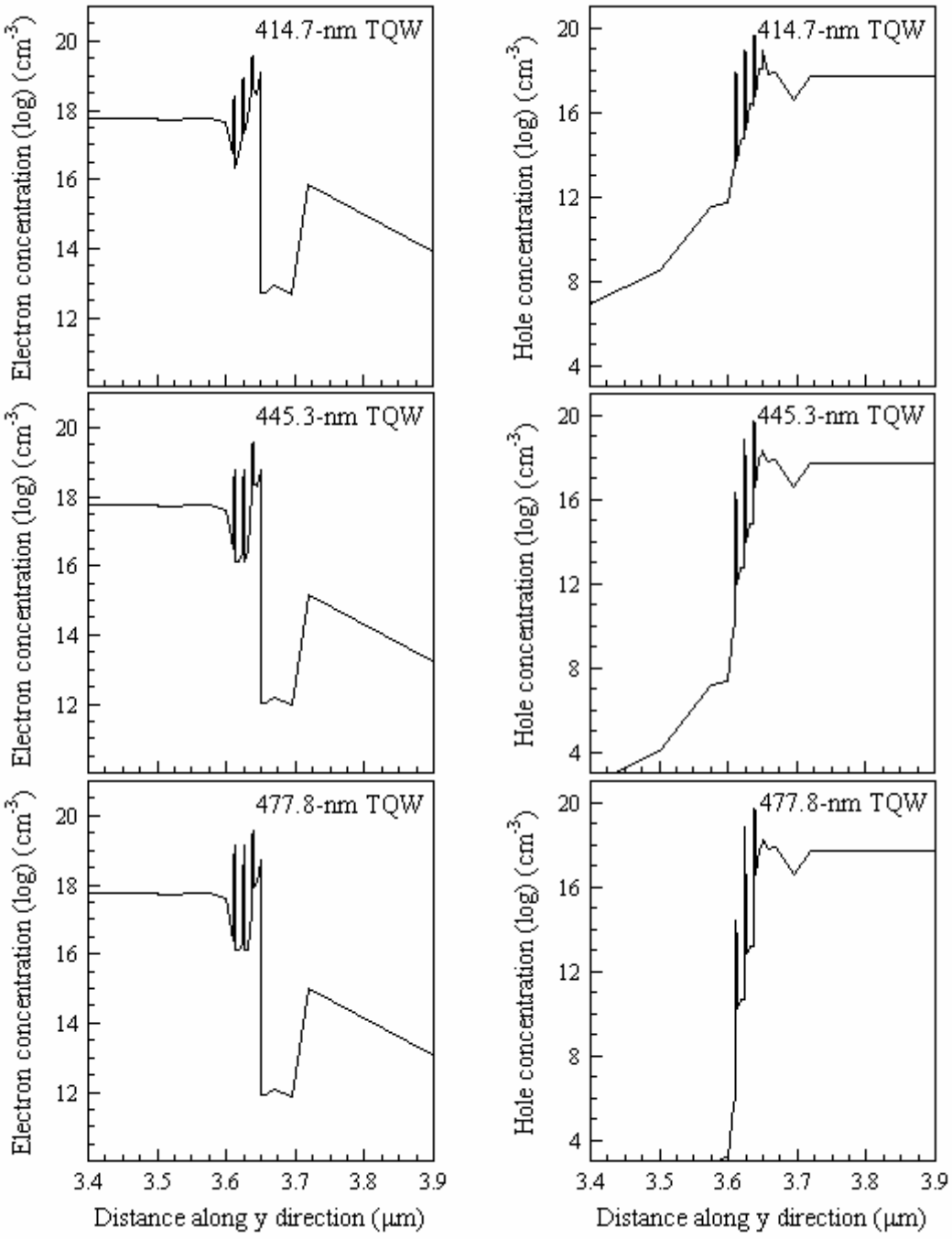


Fig. 2.24. Electron and hole concentration distributions of 414.7-nm, 445.3-nm, and 477.8-nm TQW LDs.

As shown in Fig. 2.24, the phenomenon of inhomogeneous hole distribution becomes much more severe in each plot of hole concentration distribution, when compared with those in Fig. 2.22 and Fig. 2.23. The amount of holes confined in the most p-side quantum well layer is much higher than that in the most n-side quantum well layer. The value of hole concentration of the most n-side quantum well layer of 414.7-nm TQW LD is still a little higher than that of p-side layers. As shown in Fig. 2.9, the threshold current and slope efficiency of 414.7-nm TQW LD are 703 mA and 0.016, respectively. However, both 445.3-nm and 477.8-nm TQW LDs cannot lase at an injection current of 1000 mA, because the hole inhomogeneity becomes much more serious.

# Chapter 3. Electronic Current Overflow and Laser Characteristics of a 405-nm LD

In recent years, III-nitride semiconductor materials play an important role in the development of ultraviolet/violet/blue/green LDs and LEDs. InGaN/InGaN-based violet-blue LDs with emission wavelength of 400 – 410 nm are favorable for high-density optical storage systems. High-performance, high-relaibility 400 – 410-nm LDs with fundamental mode are required. In this chapter, the electronic current overflow of a 405-nm InGaN LD as functions of the number of InGaN well layers, the Al composition in AlGaN blocking layer, and the doping concentration of p-type layers is discussed. Laser performance of the 405-nm DQW LD is studied. Moreover, the optical and electrical properties such as L-I, I-V characteristics, energy band diagram, and so on of 405-nm DQW LD are discussed as well.

## 3.1 Electronic Current Overflow

The phenomenon of electronic current overflow is always an important issue in the development of III-nitride LDs. Ideally, if the amount of electronic overflow current can be reduced, which means that more electrons can be confined in the active layers, laser performance may probably be enhanced. In the growth of III-nitride LDs, a 20-nm-thick $Al_{0.2}Ga_{0.8}N$ layer is usually required to prevent the indium from evaporating out of the InGaN active region at high temperature growth of p-type layers. This idea was first proposed by Nakamura *et al.*; however, the $Al_{0.2}Ga_{0.8}N$ layer also played an important role in blocking electrons from overflowing to the p-type layers. Because the bandgap energy of $Al_{0.2}Ga_{0.8}N$ blocking layer is higher than that of InGaN quantum well layers, AlGaN layer can block most electrons from overflowing to the p-type layers effectively.

The cause of electronic current overflow of III-nitride LDs has been verified. Small conduction band-offset value, low-concentration and high-resistivity p-type layers of III-nitride LDs, large hole effective mass, narrow well width, and high threshold current density are the main reasons to cause the phenomenon of electronic current overflow.

The band-offset value is dependent on each semiconductor material. One can imagine that there may be more electrons overflowing to the p-side layers if the conduction band-offset value is smaller. As shown in

Fig. 3.1, two different kinds of band alignments are plotted to investigate the phenomenon of electronic current overflow as a function of the band-offset value. The band-offset value plotted in Fig. 3.1(a) is larger than that in Fig. 3.1(b). Several researchers believe that the ratio of conduction band-offset value to valence band-offset value ($\Delta E_c$ : $\Delta E_v$) is roughly 30 : 70 for InN-GaN, which indicates that the depth of InGaN well layers in conduction band may be too shallow to confine the electrons. As a result, the phenomenon of electronic current overflow is so evident that it cannot be neglected in III-nitride LDs.

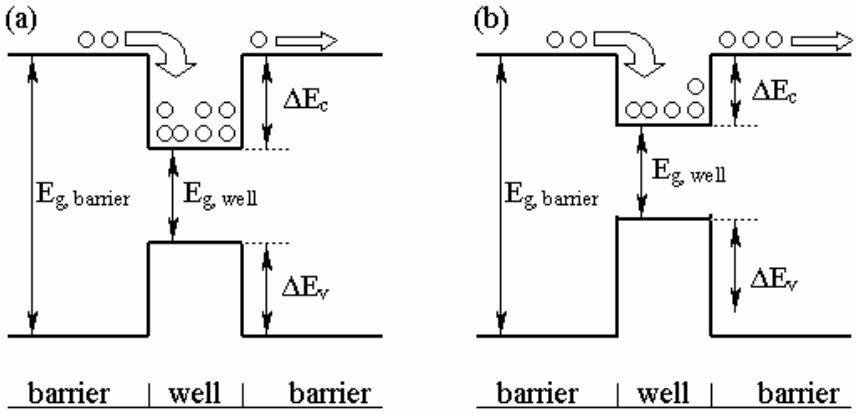


Fig. 3.1. A schematic illustration of (a) large, (b) small conduction band-offset value.

One of the bottlenecks of the development of III-nitride LDs, as mentioned in chapter 1, is to obtain high-quality, high-concentration, and low-resistivity p-type layers. Even though this problem has almost been solved in recent years, very pure, high-concentration, low-resistivity p-type layers are still too difficult to be realized in III-nitride LDs. In the

low-concentration p-type layers the electrons can have better chance to overflow to p-type layers, while high resistivity of p-type layers tend to obstruct holes from transporting to the active region. Also, large hole effective mass and low hole mobility make holes difficult to migrate to the active region. Under these circumstances, more electrons are attracted to flow to the p-type layers, and population inversion is hard to achieve. Therefore, the phenomenon of electronic current overflow is too important to be ignored.

Unfortunately, there also exists large lattice mismatch in III-nitride materials. The active region of III-nitride LDs is usually designed as superlattice layer to prevent defects caused by strain. In general, the thickness of InGaN well layers is always less than 4.0 nm, with which the first quantized level (n = 1) is farther away from the conduction band edge of quantum well layers. Therefore, it is easier for the electrons to climb over the barriers to overflow to the p-type layers.

III-nitride LDs usually needs a higher injection current density to lase due to high-density dislocation, high resistivity, poor mirror facets, etc. The threshold current density of III-nitride LDs is so high that the temperature of the devices is increased under high current injection. Hence, electrons confined in the active region possess more energy to overflow to the p-type layers. It also makes the phenomenon of electronic current overflow a severe problem in III-nitride LDs.

For the main portion of this section, the percentage of electronic

overflow current density as functions of the number of well layers, the p-doping concentration, and the Al composition in AlGaN blocking layer of 405-nm LD are discussed. First of all, the structure of a 404.5-nm LD is investigated.

### 3.1.1 405-nm LD Structure

As mentioned in section 2.3, several designs of the active region of III-nitride LDs with emission wavelength of 400 – 410 nm can be found. Among these, a 405-nm LD is chosen for further investigation, because its emission wavelength is almost at the middle of this spectral range. Most importantly, the emission wavelength of the laser pick-up head for the next generation high-density optical storage system has been chosen to be 405 nm. Therefore, the design of 405-nm LDs is relatively important for this application. The 405-nm LD structure under study, which is schematically depicted in Fig. 3.2, consists of a 3.0-μm-thick layer of n-type GaN, a 0.1-μm-thick layer of n-type $In_{0.1}Ga_{0.9}N$, a 0.4-μm-thick cladding layer of n-type $Al_{0.14}Ga_{0.86}N$, a 0.1-μm-thick layer of n-type GaN, an $In_{0.1}Ga_{0.9}N/In_{0.03}Ga_{0.97}N$ DQW active region, a p-type AlGaN blocking layer, a 0.05-μm-thick layer of p-type GaN, a 0.4-μm-thick cladding layer of p-type $Al_{0.14}Ga_{0.86}N$, and a 0.1-μm-thick layer of p-type GaN. The doping value of all n-type layers is equal to $1\times10^{18}$ $cm^{-3}$, and that of all p-type layers is equal to $5\times10^{17}$ $cm^{-3}$. The n-contact and p-contact are

directly on the bottom and top of the LD structure. The width of the LD is 10 μm and the cavity length is 500 μm. The reflectivities of front and rear facets are assumed to be 30%. The MQW active region consists of two 2.0-nm-thick $In_{0.1}Ga_{0.9}N$ well layers sandwiched between 4.0-nm-thick $In_{0.03}Ga_{0.97}N$ barrier layers. The DQW structure is used for this study because it can have the lowest threshold current as discussed in section 2.3.

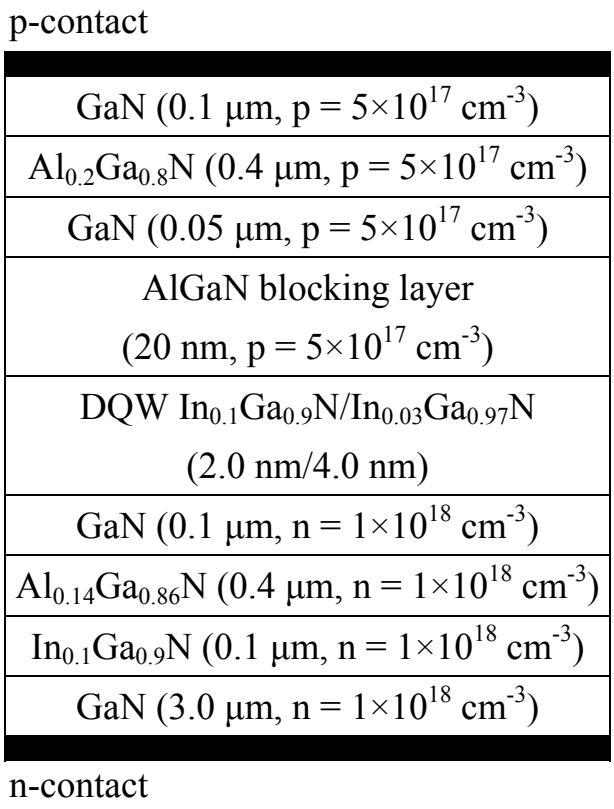


Fig. 3.2. Schematic structure of preliminary 405-nm LD.

For this preliminary laser diode structure, it was assumed that the value of p-type doping ($5\times10^{17}$ $cm^{-3}$) is twice lower than that of n-type doping. This is due to the fact that it is relatively difficult to obtain high p-type

doping value in InGaN/InGaN LDs. The material parameters for the simulation of 405-nm LD are the same as those used in section 2.2. In the following subsections, the percentage of electronic overflow current density as functions of the number of well layers, the p-doing concentration, and the aluminum composition in AlGaN blocking layer is discussed separately.

### 3.1.2 Number of Well Layers

One may expect that the electronic current overflow may be improved with the increase of the number of InGaN well layers, because more well layers in the active region may confine more electrons when the injection current density remains unchanged. In the analysis of electronic overflow current density as a function of the number of well layers, the structure of 405-nm LD is almost unchanged in spite of the Al composition in AlGaN layer is set to zero. As referred to section 2.3, more electrons can be confined in the active region when a 20-nm-thick $Al_{0.2}Ga_{0.8}N$ layer is located on top of the active region. In other words, the electronic overflow current density can be reduced greatly. In this specific study, it is assumed that the Al composition in AlGaN blocking layer is set to zero for the discussion of the electronic overflow current density as a function of the number of well layers.

Table 3.1. Percentage of electronic overflow current density as a function of the number of well layers at variant injection current density.

| Total current density (kA/cm$^2$) | Number of well layers | | | | |
|---|---|---|---|---|---|
| | 1 | 2 | 3 | 4 | 5 |
| | Overflow percentage (%) | | | | |
| 2.0 | 28.96 | 27.35 | 26.94 | 26.83 | 26.79 |
| 4.0 | 45.86 | 44.38 | 44.17 | 44.14 | 44.14 |
| 6.0 | 54.90 | 53.33 | 53.25 | 53.42 | 53.47 |
| 8.0 | 60.64 | 59.07 | 59.03 | 59.25 | 59.39 |
| 10.0 | 64.68 | 63.15 | 63.14 | 63.35 | 63.57 |
| 12.0 | 67.69 | 66.24 | 66.24 | 66.44 | 66.68 |
| 14.0 | 70.05 | 68.69 | 68.70 | 68.88 | 69.12 |
| 16.0 | 71.96 | 70.69 | 70.70 | 70.87 | 71.11 |
| 18.0 | 73.54 | 72.36 | 72.38 | 72.54 | 72.77 |
| 20.0 | 74.89 | 73.79 | 73.81 | 73.96 | 74.18 |

The percentage of electronic overflow current density as a function of the number of well layers at variant total injection current density is listed in Table 3.1. When a 405-nm LD is under low injection current density, the amount of electron overflow current density is low, as expected. There are fewer electrons that overflow when the number of well layers is increased. However, when the number of well layer is set to four or five, the percentage of electronic overflow current density is almost the same when the total injection current density is equal to 4.0 kA/cm$^2$. As the injection current density is increased to as high as 12.0 kA/cm$^2$, electronic overflow

current density is almost the same for DQW and TQW LDs. However, the overflow percentage is always the highest at each value of injection current density when the number of well layers is one. When the total injection current density is further increased, the distinction of the percentage of electronic overflow current density between variant designs of the number of well layers becomes smaller. Note that, the overflow percentage of DQW LD is the lowest when the injection current density is higher than 14.0 kA/cm$^2$, even though the distinction is tiny.

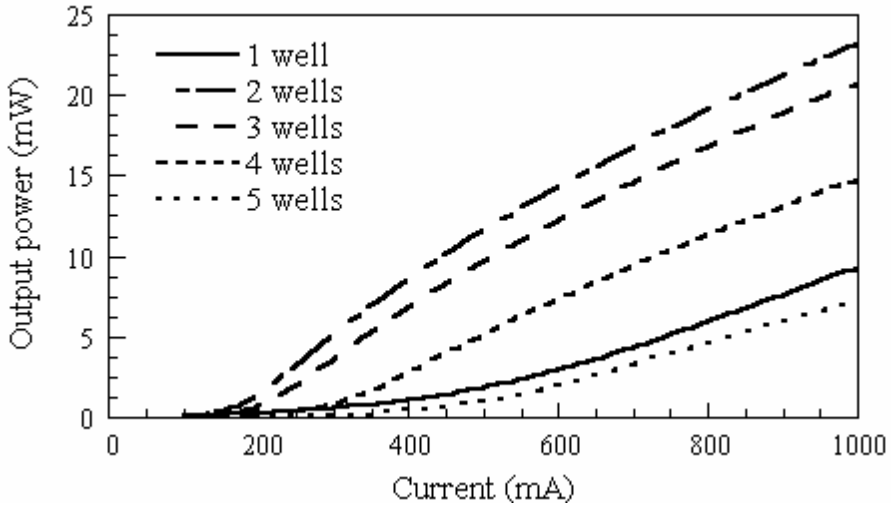


Fig. 3.3. Laser performance as a function of the number of well layers when the Al composition in the AlGaN layer is set to zero.

Figure 3.3 depicts the laser performance of 405-nm LD as a function of the number of well layers when the Al composition in AlGaN layer is set to zero. It is noteworthy that, the best laser performance can be obtained when the number of well layers is two. The simulation result is the same as that

obtained when the Al composition in AlGaN layer is equal to 0.2. The threshold current densities are 9.1, 3.3, 3.6, 5.3, and 8.7 kA/cm$^2$. The percentages of electronic overflow current density are 60.8%, 38.4%, 40.7%, 50.2%, and 60.9% at threshold current density when the number of well layers is one to five, respectively.

### 3.1.3 P-doping Concentration

Another approach to blocking electrons from overflowing to the p-side layers is to increase the value of p-type doping level of p-type layers. It is reasonable that a higher p-doping level can make electrons difficult to overflow to p-side layers, and more electrons may pile up in the undoped active region. As a consequence, the laser performance may be enhanced. In previous simulations, the p-doping level of each p-type layer for the discussion of the optimization design of the number of InGaN well layers to obtain the lowest threshold current in section 2.3 is set to $5.0\times10^{17}$ cm$^{-3}$. This value is relatively low for the purpose of conforming to the difficulty in obtaining a higher p-doping level in the growth of III-nitride LDs. In the analysis of the percentage of electronic overflow current density as a function of the p-doping concentration of p-type layers, the Al composition in AlGaN layer is still set to zero for the same purpose in last subsection. In addition, the number of $In_{0.1}Ga_{0.9}N$ well layers is set to two, and each p-type layer has the same p-doping concentration. Five different values of

p-doping concentration are discussed, namely, $2.5\times10^{17}$, $5.0\times10^{17}$, $1.0\times10^{18}$, $2.0\times10^{18}$, and $4\times10^{18}$ $cm^{-3}$.

Table 3.2. Percentage of electronic overflow current density as a function of the p-doping level at variant injection current density.

| Total current density ($kA/cm^2$) | P-doping concentration ($10^{18}$ $cm^{-3}$) | | | | |
|---|---|---|---|---|---|
| | 0.25 | 0.5 | 1.0 | 2.0 | 4.0 |
| | Overflow percentage (%) | | | | |
| 2.0 | 38.35 | 27.35 | 15.67 | 5.35 | 1.23 |
| 4.0 | 53.34 | 44.38 | 34.17 | 21.24 | 8.25 |
| 6.0 | 60.93 | 53.33 | 44.86 | 33.59 | 19.21 |
| 8.0 | 65.68 | 59.07 | 51.89 | 42.24 | 28.61 |
| 10.0 | 69.04 | 63.15 | 56.91 | 48.54 | 35.98 |
| 12.0 | 71.58 | 66.24 | 60.70 | 53.33 | 41.80 |
| 14.0 | 73.60 | 68.69 | 63.70 | 57.10 | 46.48 |
| 16.0 | 75.26 | 70.69 | 66.13 | 60.16 | 50.32 |
| 18.0 | 76.64 | 72.36 | 68.15 | 62.70 | 53.53 |
| 20.0 | 77.83 | 73.79 | 69.87 | 64.85 | 56.26 |

Table 3.2 lists the percentage of electronic overflow current density as a function of the p-doping concentration at variant injection current density. As the same results in last subsection, the percentage of electronic overflow current density is proportional to the total injection current density for each value of p-doping concentration. When the total injection current density is high, a large amount of electrons may overflow to the p-type layers.

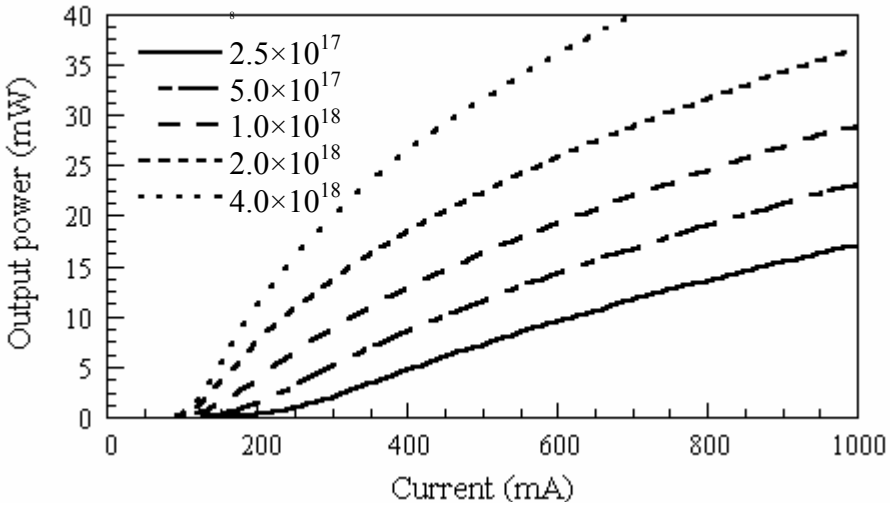


Fig. 3.4. Laser performance as a function of the p-doping concentration when the Al composition in AlGaN layer is set to zero.

Table 3.3. Threshold current density, slope efficiency above the threshold current density, threshold voltage, and percentage of the overflow current density at threshold as a function of the doping concentration.

| P-doping concentration ($10^{18}$ $cm^{-3}$) | 0.25 | 0.5 | 1.0 | 2.0 | 4.0 |
|---|---|---|---|---|---|
| Threshold current density ($kA/cm^2$) | 4.30 | 3.23 | 2.37 | 2.15 | 2.05 |
| Slope efficiency (W/A) | 0.026 | 0.037 | 0.048 | 0.082 | 0.116 |
| Threshold voltage (V) | 4.10 | 3.93 | 3.78 | 3.64 | 3.51 |
| Overflow percentage at threshold (%) | 54.48 | 29.30 | 19.09 | 6.54 | 1.41 |

The laser performance as a function of the p-doping concentration when the Al composition in AlGaN layer is zero is shown in Fig. 3.4. The threshold current density, slope efficiency near the threshold current density, threshold voltage, and percentage of electronic overflow current density at

threshold as a function of the doping concentration are listed in Table 3.3. The laser performance can be enhanced with the increase of the p-doping concentration. Furthermore, the threshold voltage is reduced, and the overflow percentage at the threshold current density can be obviously decreased as well.

### 3.1.4 Al Composition in AlGaN Blocking Layer

Due to the small conduction band-offset value in InGaN active region, the phenomenon of electronic current overflow is a crucial issue of III-nitride LDs. In the growth of III-nitride LDs, it always requires an AlGaN electron-blocking layer above the InGaN/InGaN active region. However, several groups use different Al composition in AlGaN layer in the growth of III-nitride LDs. For example, Nakamura *et al*. often used 20% Al composition in AlGaN layer, and that of InGaN/InGaN LDs of Sony Corporation was 18% [131], [132]. Therefore, it is interesting to investigate what level of Al composition in AlGaN blocking layer is enough to block most electrons from overflowing to the p-side layers.

In the analysis of the percentage of electronic overflow current density as a function of the Al composition in AlGaN blocking layer, the p-type doping value is still set to $5\times10^{17}$ $cm^{-3}$, and the thickness of AlGaN blocking layer is fixd at 20 nm. An extreme situation is that the Al composition in AlGaN blocking layer is set to zero, which means that the

20-nm-thick AlGaN layer is exchanged with 20-nm-thick GaN layer. The electronic overflow current density and active current density, defined as electronic current confined in quantum well layers, as a function of the total current density are shown in Fig. 3.5(a).

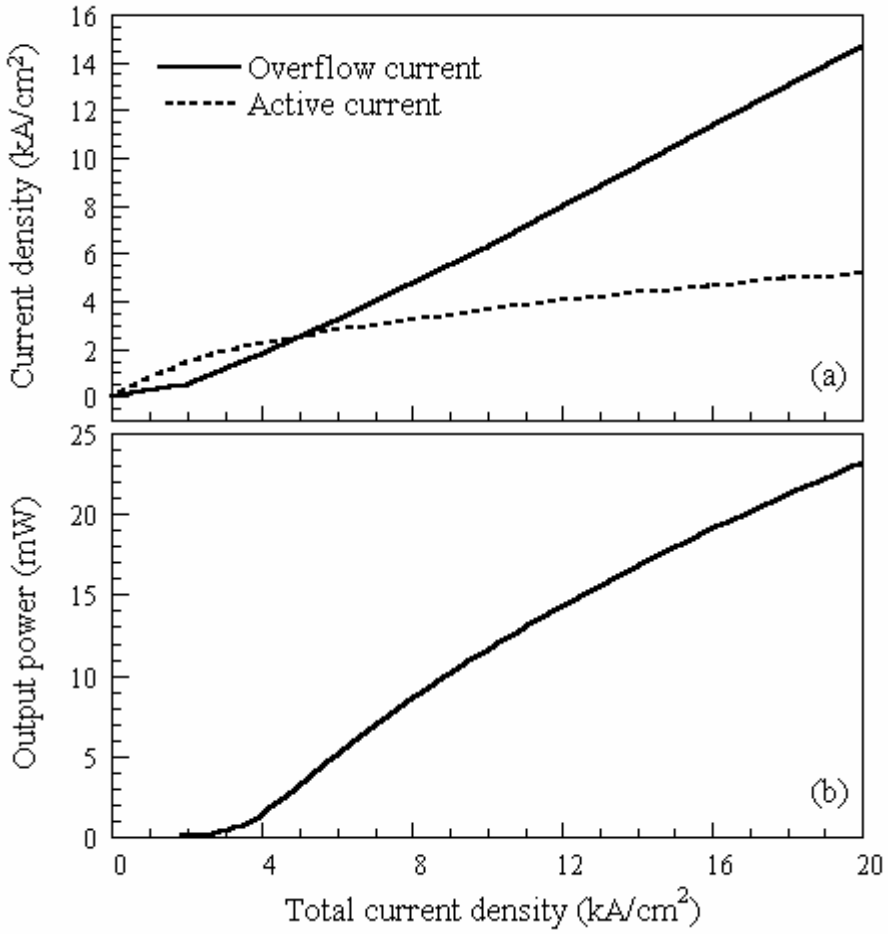


Fig. 3.5. (a) Electronic overflow current density and active current density as a function of total current density. (b) Laser performance of 404.5-nm LD without AlGaN blocking layer.

When the LD is under low injection current density, the active current

density is larger than the electronic overflow current density. In other words, more electrons can be confined in the active layers effectively. The amount of active current density is equal to overflow current density when the total current density is about 4.8 kA/cm$^2$. Laser performance of 405-nm LD without AlGaN blocking layer is shown in Fig. 3.5(b). The threshold current density and slope efficiency are 3.26 kA/cm$^2$ and 0.038 W/A, respectively. When the total current density is equal to the threshold current density, only 40% current density can be confined in the active layers. However, the other 60% current density overflows to p-side layers.

Table 3.4. Percentages of electronic overflow current density and active current density as a function of the total current density.

| Current density (kA/cm$^2$) | 2.0 | 4.0 | 6.0 | 8.0 | 10.0 | 12.0 | 14.0 | 16.0 | 18.0 | 20.0 |
|---|---|---|---|---|---|---|---|---|---|---|
| Overflow percentage (%) | 27.4 | 44.4 | 53.3 | 59.1 | 63.1 | 66.2 | 68.7 | 70.7 | 72.4 | 73.8 |
| Active percentage (%) | 72.6 | 55.6 | 46.7 | 40.9 | 36.9 | 33.8 | 31.3 | 29.3 | 27.6 | 26.2 |

The percentages of electronic overflow current density and active current density as a function of total current density are listed in Table 3.4. It can be found that there are more electrons overflowing to the p-side layer when the total current density is increased. When the total current density is equal to 20.0 kA/cm$^2$, corresponding to an injection current of 1000 mA, 73.8% current density becomes electronic overflow current density, and the output power is only 23.2 mW, which is less than 30 mW.

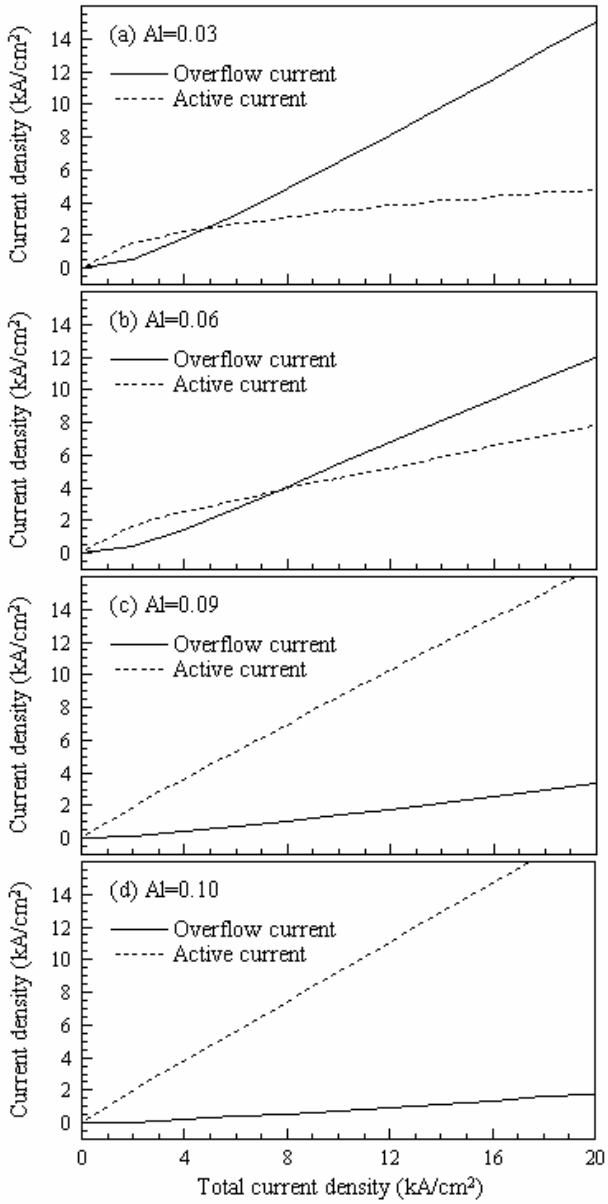


Fig. 3.6. Electronic overflow current density and active current density as a function of the total current density when the Al mcomposition is equal to (a) 0.03, (b) 0.06, (c) 0.09, and (d) 0.10.

The amount of electronic overflow current density and active current

density as a function of the total current density when the Al composition is equal to 0.03, 0.06, 0.09, and 0.10 are listed in Fig. 3.6. The active current density is increased when the Al composition in AlGaN layer is increased. The active current density is equal to the electronic overflow current density when the total current density is 5.0 kA/cm$^2$ for Al=0.03, and 7.8 kA/cm$^2$ for Al=0.06, respectively. However, when the Al composition in AlGaN layer is equal to 0.09 and 0.10, the active current density is always higher than the electronic overflow current density at variant injection current density, which means that most electrons can be confined in the active layers when the total current density is below 20 kA/cm$^2$.

Laser performance of 405-nm LD with an AlGaN blocking layer, in which the Al composition are equal to 0.03, 0.06, 0.09, and 0.10, is shown in Fig. 3.7. The threshold current densities are equal to 3.15, 2.66, 2.30, and 2.22 kA/cm$^2$ when the Al composition in AlGaN layer are 0.03, 0.06, 0.09, and 0.10, respectively. The threshold current density has been reduced because most electrons can be confined in quantum well layers. It is noteworthy that, when the Al composition in AlGaN layer is equal to 0.03, the output power is still less than 30 mW at an injection current density of 20 kA/cm$^2$. Nevertheless, when the Al composition is increased to as high as 0.06, the slope efficiency can be enhanced and the 405-nm LDs can operate with an output power of over 30 mW. For Al=0.06, 0.09, and 0.10, the injection current densities are as high as 15.2, 7.2, and 6.8 kA/cm$^2$ for the purpose of obtaining an output power of 30 mW, respectively.

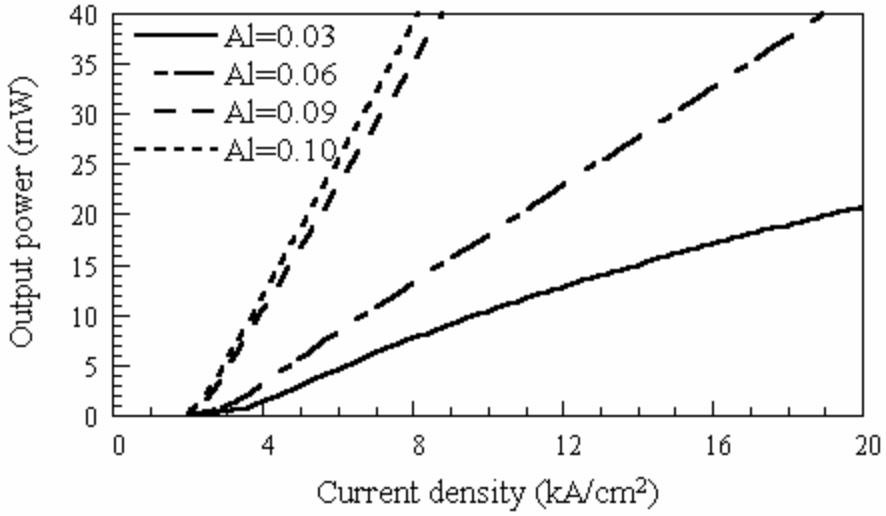


Fig. 3.7. Laser performances of 405-nm LD with AlGaN blocking layer, in which the Al composition are equal to 0.03, 0.06, 0.09, and 0.10.

The percentage of electronic overflow current density and active current density as a function of the total current density when the Al compositions in AlGaN layer are equal to 0.03, 0.06, 0.09, and 0.10 are listed in Table 3.5. When the LDs are operated at threshold current density, the percentages of electronic overflow current density are 39% and 27% for Al=0.03 and Al=0.06, respectively. When the Al composition is further increased to 0.09 and 0.10, the percentages of electronic overflow current density become 5% and 0.5% at threshold current density, respectively.

Table 3.5. Percentage of electronic overflow current density and active current density as a function of the total current density when the Al compositions in AlGaN layer are equal to 0.03, 0.06, 0.09, and 0.10.

| Current density ($kA/cm^2$) | 2.0 | 4.0 | 6.0 | 8.0 | 10.0 | 12.0 | 14.0 | 16.0 | 18.0 | 20.0 |
|---|---|---|---|---|---|---|---|---|---|---|
| Al = 0.03 | | | | | | | | | | |
| Overflow percentage (%) | 25.5 | 44.7 | 54.5 | 60.6 | 64.9 | 68.0 | 70.4 | 72.4 | 74.0 | 75.4 |
| Active percentage (%) | 74.5 | 55.3 | 45.5 | 39.4 | 35.1 | 32.0 | 29.6 | 27.6 | 26.0 | 24.6 |
| Al =0.06 | | | | | | | | | | |
| Overflow percentage (%) | 18.7 | 36.7 | 45.8 | 51.1 | 54.3 | 56.5 | 57.9 | 59.0 | 59.8 | 60.5 |
| Active percentage (%) | 81.3 | 63.3 | 54.2 | 48.9 | 45.7 | 43.5 | 42.1 | 41.0 | 40.2 | 39.5 |
| Al =0.09 | | | | | | | | | | |
| Overflow percentage (%) | 6.3 | 10.7 | 12.4 | 13.5 | 14.2 | 14.9 | 15.5 | 16.1 | 16.6 | 17.2 |
| Active percentage (%) | 93.7 | 89.3 | 87.6 | 86.5 | 85.8 | 85.1 | 84.5 | 83.9 | 83.4 | 82.8 |
| Al =0.10 | | | | | | | | | | |
| Overflow percentage (%) | 3.4 | 5.5 | 6.4 | 7.0 | 7.4 | 7.8 | 8.1 | 8.5 | 8.8 | 9.2 |
| Active percentage (%) | 96.6 | 94.5 | 93.6 | 93.0 | 92.6 | 92.2 | 91.9 | 91.5 | 91.2 | 90.8 |

As mentioned previously, a 405-nm LD with an output power of more than 30 mW is required. However, only when the Al composition in AlGaN layer is beyond 0.06 can an output power of more than 30 mW be obtained. Another significant issue is to estimate how many percents of the total current density becomes electronic overflow current density when the

405-nm LD is at the injection current density for obtaining an output power of 30 mW. For Al = 0.06, 58.7% of the total current density (15.2 kA/cm$^2$) becomes electronic overflow current density. For Al = 0.09 and 0.10, 12.7% of 7.2 kA/cm$^2$ and 6.1% of 6.8 kA/cm$^2$ become electronic overflow current density, respectively.

Table 3.6. Percentages of electronic overflow current density at the injection current of threshold and that for obtaining an output power of 30 mW when the Al composition is at a range from 0.11 to 0.20

| Al composition | Threshold current density (kA/cm$^2$) | Overflow percentage (%) | 30-mW current density (kA/cm$^2$) | Overflow percentage (%) |
|---|---|---|---|---|
| 0.11 | 2.190 | 1.85 | 6.449 | 3.25 |
| 0.12 | 2.177 | 0.98 | 6.341 | 1.61 |
| 0.13 | 2.171 | 0.56 | 6.292 | 0.86 |
| 0.14 | 2.168 | 0.36 | 6.269 | 0.47 |
| 0.15 | 2.167 | 0.26 | 6.258 | 0.30 |
| 0.16 | 2.167 | 0.22 | 6.253 | 0.22 |
| 0.17 | 2.166 | 0.22 | 6.251 | 0.18 |
| 0.18 | 2.166 | 0.22 | 6.250 | 0.17 |
| 0.19 | 2.166 | 0.22 | 6.249 | 0.16 |
| 0.20 | 2.166 | 0.22 | 6.249 | 0.16 |

When the Al composition in AlGaN blocking layer is equal to 0.10, it is obvious that the threshold current density can be reduced to an acceptable value (2.22 kA/cm$^2$). However, the percentage of electronic overflow current density at the threshold current density and that for obtaining an output power of 30 mW still can be reduced. The laser performance can be enhanced if the overflow current density is reduced.

The percentages of electronic overflow current density at the threshold current density and that for obtaining an output power of 30 mW when the Al composition is in a range from 0.11 to 0.20 are listed in Table 3.6. When the Al composition in AlGaN layer is increased from 0.11 to 0.16, the threshold current density can be reduced from 2.190 to 2.167 kA/cm$^2$. The percentage of electronic overflow current density at the threshold current density can be reduced from 1.85% to 0.22%, and the percentage of electronic overflow current density can further be reduced from 3.25% to 0.22% at the injection current density for obtaining an output power of 30 mW, when the Al composition in AlGaN layer is increased from 0.11 to 0.16.

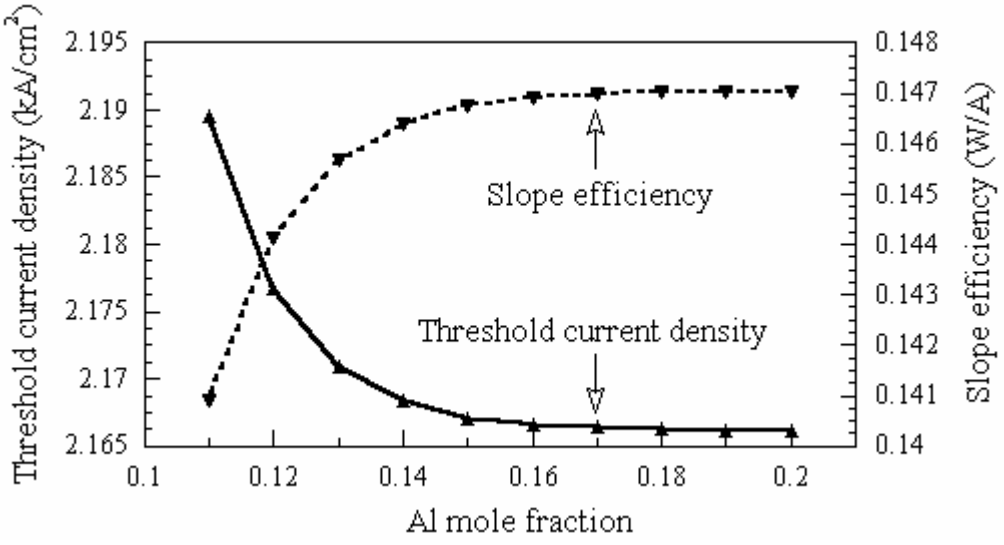


Fig. 3.8. Laser performance of 404.5-nm LD as a function of the Al composition in AlGaN layer.

The laser performance of 405-nm LD as a function of the Al composition in AlGaN layer is shown in Fig. 3.8. It is obvious that the threshold current density and slope efficiency remain unchanged when the Al composition is beyond 0.16. The electronic overflow current density can further be reduced to 0.16% when the Al composition is equal to 0.20 at the injection current density for obtaining an output power of 30 mW.

## 3.2 Laser Characteristics of 405-nm LD

As discussed in prior section, low threshold current density and high slope efficiency can be obtained when the Al composition in AlGaN blocking layer is equal to 0.16. Most electrons can be confined in quantum well layers at the threshold current density or at the injection current for obtaining an output power of 30 mW. The percentage of electronic overflow current density almost decreases to zero when the Al composition in AlGaN blocking layer is 0.16. In other words, good laser performance and low electronic overflow current density can be obtained when the Al composition in AlGaN layer in 405-nm LD is equal to 0.16. The optical and electrical characteristics of a 405-nm LD when the Al composition in AlGaN layer is 0.16 are investigated in this section.

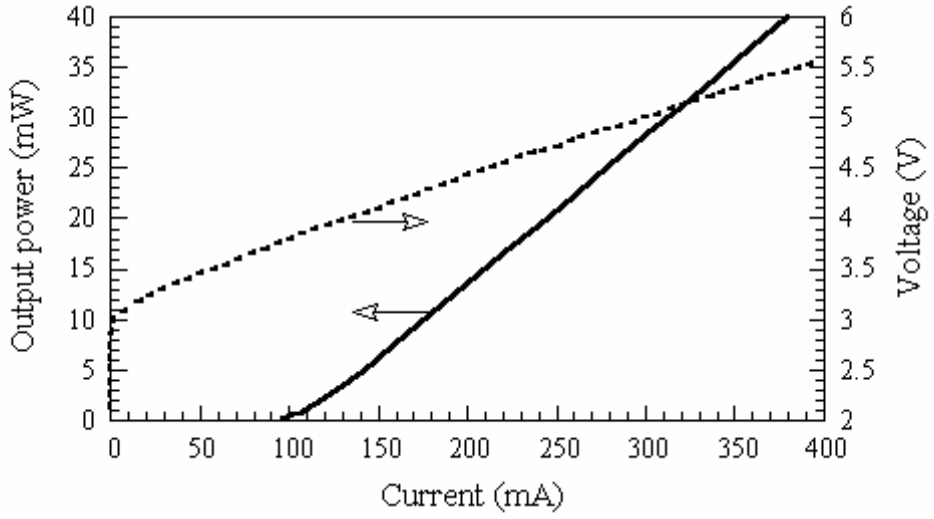


Fig. 3.9 L-I and I-V characteristics of 405-nm DQW LD under study.

Figure 3.9 shows the L-I and I-V characteristics of the 405-nm DQW LD under study. The threshold current and the voltage at threshold current are 108 mA and 3.85 V, respectively. When the injection current and voltage are equal to 312.7 mA and 5.1 V, an output power of 30 mW can be obtained. The slope efficiency near the threshold current is approximately 14.6%.

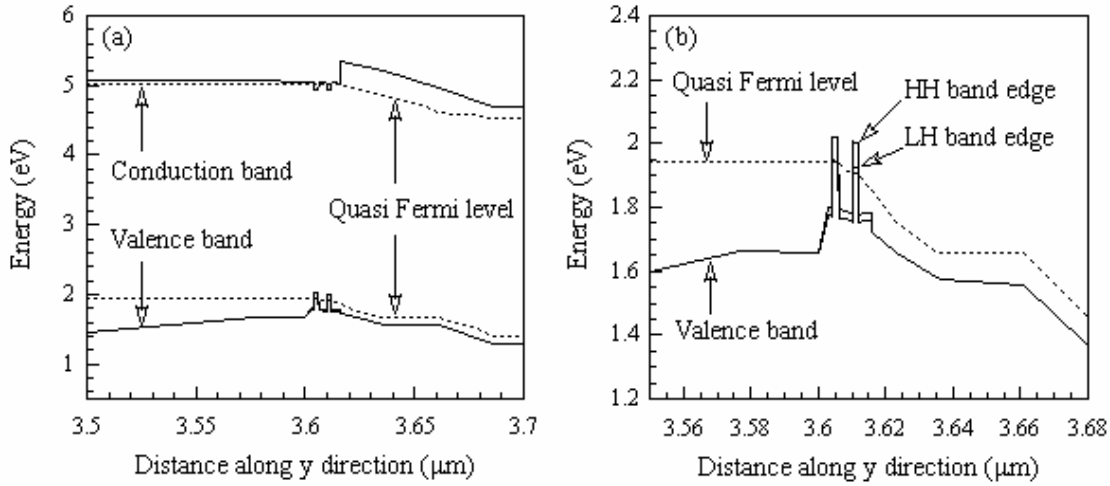


Fig. 3.10. (a) Energy band diagram of 405-nm DQW LD at the injection current to obtain an output power of 30 mW. (b) is the expanded picture of (a) near the active region of valence band.

Figure 3.10 (a) shows the energy band diagram of the 405-nm DQW LD at the injection current to obtain an output power of 30 mW. The lower quasi Fermi level is below the band edge of two quantum well layers of valence band, which indicates that the hole distribution of two quantum well layers may be homogeneous. As shown in Fig. 3.10(b), which is the

expanded picture of Fig. 3.10(a) near the active region of valence band, the HH and LH band edges appear. It is evident that the lower quasi Fermi level touches the LH band edge of n-side quantum well layer and the lower quasi Fermi level is below the HH and LH band edges of p-side quantum well layer.

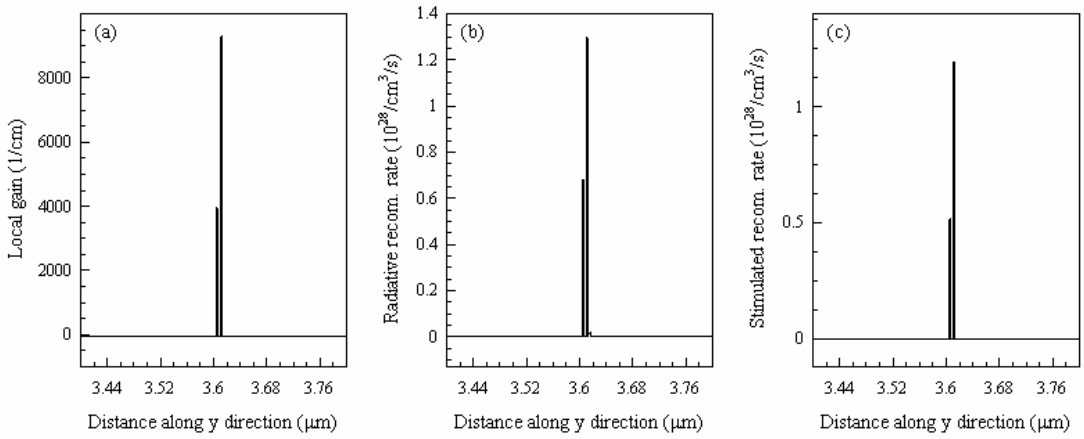


Fig. 3.11. (a) Local gain, (b) radiative recombination rate, (c) stimulated recombination rate near the active region of 405-nm DQW LD at the injection current to obtain an output power of 30 mW.

Figures 3.11(a), 3.11(b), 3.11(c) show the local gain, radiative recombination rate, and stimulated recombination rate near the active region of 405-nm DQW LD at the injection current to obtain an output power of 30 mW, respectively. The n-side quantum well layer can contribute to laser light emission, and the p-side quantum well layer always has better performance than the n-side quantum well layer. Nevertheless, the local gain, radiative recombination rate, and stimulated recombination

rate of the n-side quantum well layer drop apparently when the injection current is increased to obtain a higher output power. This may be due to that high injection current results in band bending, and more holes are confined in the p-side quantum well layer. Therefore, the performance of the p-side quantum well layer arises and that of n-side quantum well layer drops when the injection current is increased to obtain higher output power.

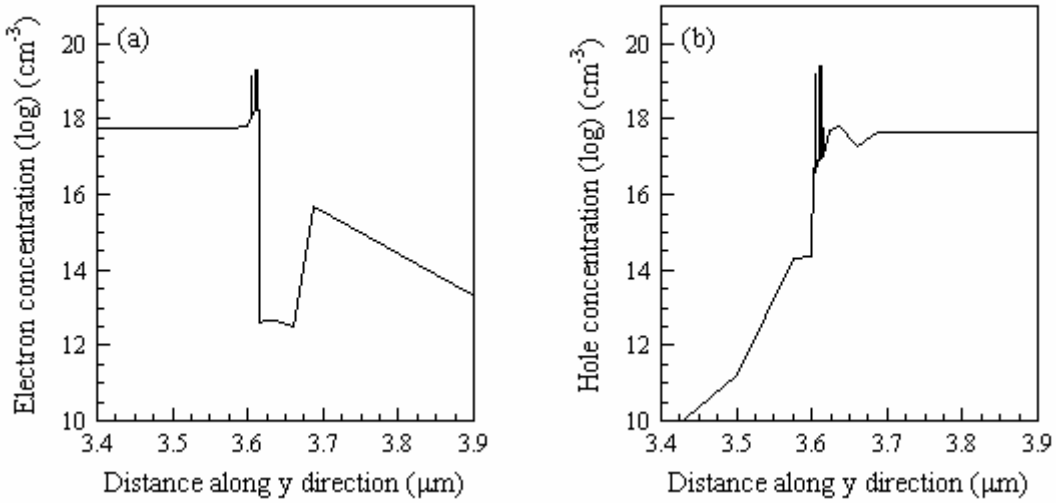


Fig. 3.12. (a) Electron and (b) hole concentration distribution near the active region at the injection current to obtain an output power of 30 mW.

Figures 3.12(a) and 3.12(b) show the electron and hole concentration distribution near the active region at the injection current to obtain an output power of 30 mW. The electron concentration of p-side quantum well layer is higher than that of n-side quantum well layer, because a 20-nm-thick $Al_{0.16}Ga_{0.84}N$ layer can block most electrons from overflowing to the p-type layers. As shown in Fig. 3.12(b), the hole concentration of

p-side quantum well layer is also higher than that of n-side quantum well layer, which may be due to that the valence band-offset value and hole effective mass are large. When holes move into the p-side quantum well layers, it is hard for holes to further transport to the n-side quantum well layer. Therefore, there are more electrons and holes confined in p-side quantum well layer, and the performance of p-side quantum well layer is superior to that of n-side quantum well layer, as indicated in Fig. 3.11.

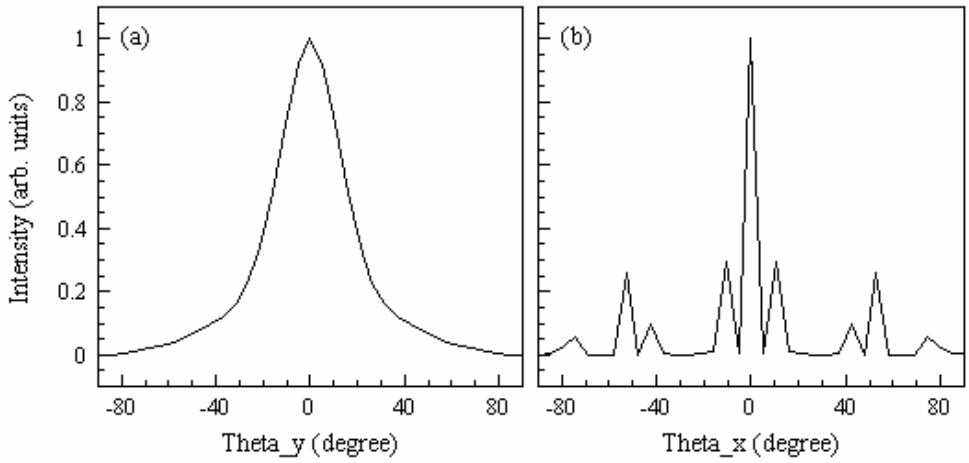


Fig. 3.13. Far-field patterns of 405-nm DQW LD in the planes (a) perpendicular (y), and (b) parallel (x) to the junction of the LD at an output power of 30 mW.

The far-field patterns (FFPs) of 405-nm DQW LD in the planes perpendicular (y) and parallel (x) to the junction of the LD at an output power of 30 mW are shown in Fig. 3.13. The FFP in the direction perpendicular to the epitaxial layers is estimated to be 31.6º and the FFP in the direction parallel to the epitaxial layer is about 5.3º, corresponding to an aspect ratio of about 6.0 for the fundamental mode. However, the real

aspect ratio is difficult to determine because several other laser modes can be found, as indicated in Fig. 3.13(b). The far-field pattern laser spot profile of 405-nm DQW LD at an output power of 30 mW is shown in Fig. 3.14, in which several lateral modes can be observed.

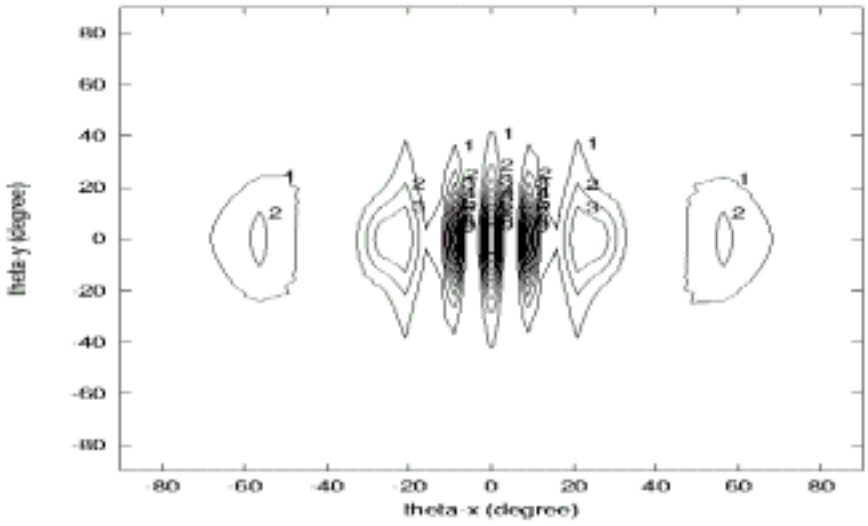


Fig. 3.14. Far-field pattern laser spot profile of 405-nm DQW LD at an output power of 30 mW.

Note that the width of the prior 405-nm LD under study was set to 10 μm. However, to achieve single-mode operation, the width of 405-nm LD must be decreased. From the simulation results we find that single-mode operation can be achieved when the width of 405-nm LD is as narrow as 2 μm. The FFPs of 405-nm DQW LD in the planes perpendicular (y) and parallel (x) to the junction of the LD when the width of the LD is 2 μm are shown in Fig. 3.15. The far-field pattern laser spot profile of 405-nm DQW LD when the width of the LD is 2 μm is shown in Fig. 3.16. The aspect

ratio can be reduced to about 2.5 for fundamental mode in this situation.

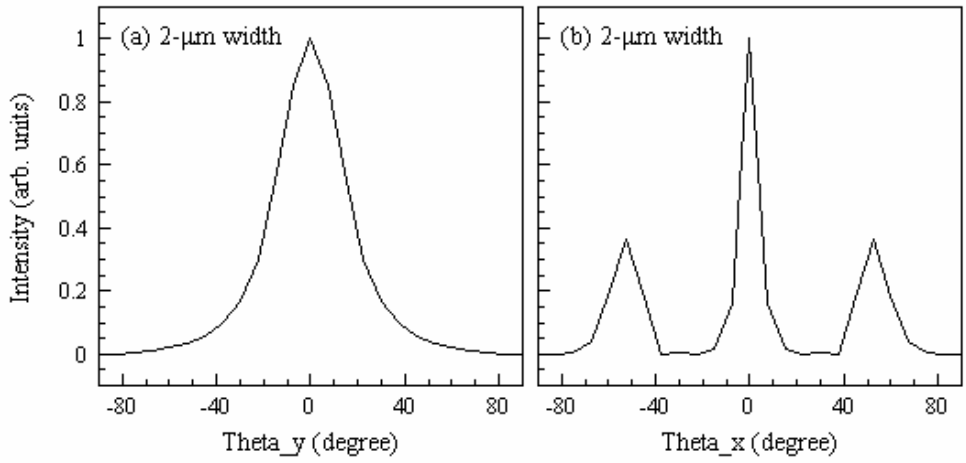


Fig. 3.15. Far-field patterns of 405-nm DQW LD in the planes (a) perpendicular (y), and (b) parallel (x) to the junction of the LD when the width of the LD is 2 μm.

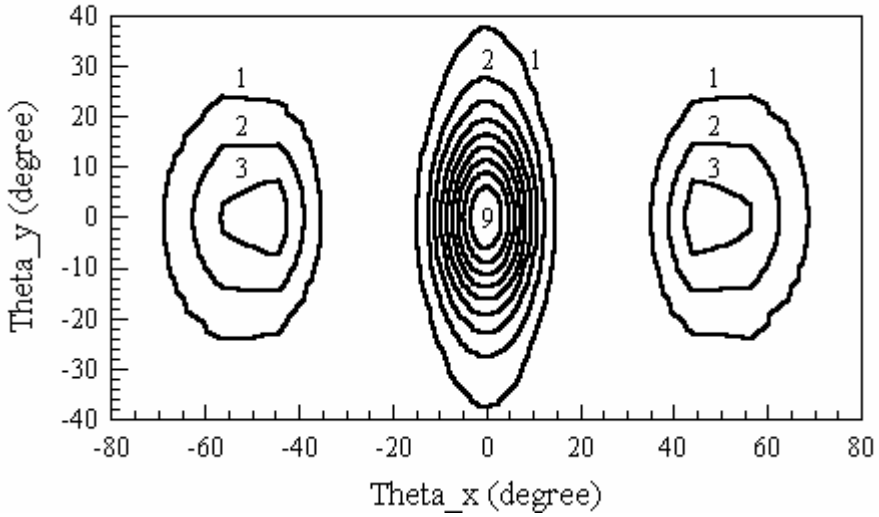


Fig. 3.16. Far-field pattern laser spot profile of 405-nm DQW LD when the width of the LD is 2 μm.

# Chapter 4. Conclusion

In this thesis, the laser performance of several laser diode structures with an emission wavelength of 396.1-479.3 nm as a function of the number of InGaN well layers are numerically studied with a LASTIP simulation program. Specifically, the effects of electronic current overflow and inhomogeneous hole distribution on the laser performance of the InGaN laser diodes operating at different wavelengths are investigated. Simulation results suggest that the use of an $Al_xGa_{1-x}N$ blocking layer with an aluminum composition of more than 0.16 can help reduce the electronic current overflow under normal operation conditions. Inhomogeneous hole distribution in multi-quantum-well structures is found in the violet-blue laser diodes under study, which deteriorates with the increase of quantum-well number and emission wavelength for the spectral range under study. This problem happens due to the difficulty for the holes to transport from one quantum well to another.

Simulation results conclude that, in general, the lowest threshold current density is obtained when the number of InGaN well layers is two if the emission wavelength is shorter than 435 nm and one if the emission wavelength is longer than 435 nm, which are in good agreement with the results observed by Nakamura *et al.* in their experiments. Simulation results also suggest that, in addition to the dissociation of the InGaN well layer at a high growth temperature during crystal growth, the

inhomogeneous hole distribution in the quantum wells also plays an important role in the laser performance as a function of the number of InGaN well layers.

Specifically, when the emission wavelengths are designed as 415.7 nm and 436.9 nm, which correspond to the design of 4.5-nm-thick $In_{0.1}Ga_{0.9}N$ well layers sandwiched between 9.0-nm-thick $In_{0.04}Ga_{0.06}N$ barriers and 2.5-nm-thick $In_{0.15}Ga_{0.85}N$ well layers sandwiched between $In_{0.06}Ga_{0.94}N$ barriers, both SQW and DQW LDs can have similar, best laser performance.

Moreover, the percentage of electronic overflow current density as functions of the number of InGaN well layers, the p-doping concentration, and the Al composition in 20-nm-thick AlGaN layer of a 405-nm $In_{0.1}Ga_{0.9}N/In_{0.03}Ga_{0.97}N$ DQW LD are also discussed in this thesis. When the Al composition in AlGaN layer is 0.16, the percentages of electronic overflow current density at the threshold current density and for obtaining an output power of 30 mW are below 0.22%, which indicates that a 20-nm-thick $Al_{0.16}Ga_{0.84}N$ layer can prevent most electrons from overflowing to the p-side layers. In the mean time, the optical and electrical characteristics of the 405-nm DQW LD, when the Al composition in AlGaN is 0.16, are also investigated in detail. When the width of the 405-nm DQW LD is 2 μm, single-mode operation with an aspect ratio of as low as 2.5 can be obtained.

The numerical simulation results obtained in this thesis may be used as

references for the design of III-nitride LDs. The quality of this work may be further improved if some important issues, such as the thermal effect and the piezo-electric effect, can be taken into consideration.

## References


[1] Govind P. Agrawal, and Niloy K. Dutta, "*Semiconductor Lasers*", 2nd, Van Nostrand Reinhold, New York (1993).

[2] R. N. Hall, G. E. Fenner, J. D. Kingsley, T. J. Soltys, and R. O. Carlson, *Phys. Rev. Lett.*, vol. 9, pp. 366 (1962).

[3] M. I. Nathan, W. P. Dumke, G. Burns, F. H. Dill, Jr., and G. Lasher, *Appl. Phys. Lett.*, vol. 1, pp. 62 (1962).

[4] T. M. Quist, R. H. Rediker, R. J. Keyes, W. E. Krag, B. Lax, A. L. McWhorter, and H. J. Zeiger, *Appl. Phys. Lett.*, vol. 1, pp. 91 (1962).

[5] N. Holonyak, Jr., and S. F. Bevacqua, *Appl. Phys. Lett.*, vol. 1, pp. 82 (1962).

[6] H. Kressel, and H. Nelson, *RCA Rev.*, vol. 30, pp. 106 (1969).

[7] I. Hayashi, M. B. Panish, and P. W. Foy, *IEEE J. Quantum Electron.*, vol. QE-5, pp. 211 (1969).

[8] Zh. I. Alferov, V. M. Andreev, E. L. Portnoi, and M. K. Trukan, *Sov. Phys. Semicond.*, vol. 3, pp. 1107 (1970).

[9] A. P. Bogatov, L. M. Dolginov, P. G. Eliseev, M.G. Mil'vidskii, B. N. Sverdlov, and E. G. Shevchenko, *Sov. Phys. Semicond.*, vol. 9, pp. 1282 (1975).

[10] J. J. Hsieh, J. A. Rossi, and J. P. Donnelly, *Appl. Phys. Lett.*, vol. 28, pp. 709 (1976).

[11] K. Oe, S. Ando, and K. Sugiyama. *Jpn. J. Appl. Phys.*, vol. 16, pp. 1273 (1977).

[12] M. Horiguchi, and H. Osani, *Electron. Lett.*, vol. 12, pp. 310 (1976).

[13] G. B. Stringfellow, and M. G. Craford, "*High Brightness Light Emitting Diodes: Semiconductors and Semimetals Volume 48*",

Academic Press, San Diego, California, USA (1997).

[14] S. Nakamura, and G. Fasol, "*The Blue Laser Diode*", Springer-Verlag, Heidelberg (1997).

[15] Joseph T. Verdeyen, "*Laser Electronics*", 2nd, Prentice-Hall International, Inc. (1989).

[16] J. I. Pankove, and T. D. Moustakas, "*Gallium Nitride (GaN) I - Semiconductors and Semimetals Volume 50*", Academic Press, San Diego, California, USA (1998).

[17] T. Yoshikawa, Y. Sugimoto, H. Hotta, K. Tada, K. Kobayashi, F. Miyasaka, and K. Asakawa, *Electron. Lett.*, vol. 30, pp. 2035 (1994).

[18] A. Shima, H. Tada, K. Ono, M. Fujiwara, T. Utakouji, T. Kimura, M. Takemi, and H. Higuchi, *IEEE Photon. Tech. Lett.*, vol. 9, no.4, pp. 413 (1997).

[19] T. Tanaka, H. Yanagisawa, M. Takimoto, S. Yano, and S. Minagawa, *Electron. Lett.*, vol. 29, no. 8, pp. 772 (1993).

[20] P. O. Kellermann, A. Golshani, A. Kőck, and E. Gornik, *Appl. Phys. Lett.*, vol. 70, pp. 2374 (1997).

[21] M. Ishikawa, H. Shiozawa, Y. Tsuburai, Y. Uematsu, *Electron. Lett.*, vol. 26, pp. 211 (1990).

[22] I. Hino, S. Kawata, A. Gomyo, K. Kobayashi, and T. Suzuki, *Appl. Phys. Lett.*, vol. 48, pp. 557 (1986).

[23] S. Yoshida, S. Misawa, and S. Gonda, *Appl. Phys. Lett.*, vol. 42, pp. 427 (1983).

[24] H. Amano, N. Sawaki, I. Akasaki, Y. Toyoda, *Appl. Phys. Lett.*, vol. 48, pp. 353 (1986).

[25] S. Nakamura, Y. Harada, and M. Seno, *Appl. Phys. Lett.*, vol. 58, pp. 2021 (1991).

[26] S. D. Lester, F. A. Ponce, M. G. Craford, and D. A. Steigerwald,

*Appl. Phys. Lett.*, vol. 66, pp. 1249 (1995).

[27] S. Chichibu, T. Azuhata, T. Sota, and S. Nakamura, *Appl. Phys. Lett.*, vol. 69, pp. 4188 (1996).

[28] F. A. Ponce, B. S. Krusor, J. S. Major, Jr., W. E. Plano, and D. F. Welch, *Appl. Phys. Lett.*, vol. 67, pp.410 (1995).

[29] T. W. Weeks, Jr., M. D. Bremser, K. S. Aliey, E. Carlson, W. G. Perry, and R. F. David, *Appl. Phys. Lett.*, vol. 67, pp. 401 (1995).

[30] S. Nakamura, M. Senoh, S. Nagahama, N. Iwasa, T. Yamada, T. Matsushita, H. Kiyoku, Y. Sugimoto, Y. Kozaki, H. Umemoto, M. Sano, K. Chocho, *Jpn. J. Appl. Phys.*, vol. 36, p. L1568 (1997).

[31] S. Nakamura, M. Senoh, S. Nagahama, N. Iwasa, T. Yamada, T. Matsushita, Y. Sugimoto, and H. Kiyoku, *Appl. Phys. Lett.*, vol. 69, pp. 1568 (1996).

[32] S. Nakamura, *IEEE J. Sel. Top. Quantum. Electron.*, vol. 4, pp. 483 (1998).

[33] S. Nakamura, T. Mukai, and M. Seno, *Jpn. J. Appl. Phys.*, vol. 31, pp. 2883 (1992).

[34] H. Amano, M. Kito, K. Hiramatsu, and I. Akasaki, *Jpn. J. Appl. Phys.*, vol. 28, p. L2112 (1989).

[35] S. Nakamura, N. Isawa, M. Senoh, and T. Mukai, *Jpn. J. Appl. Phys.*, vol. 31, pp. 1258 (1992).

[36] S. Nakamura, T. Mukai, M. Senoh, and N. Iwasa, *Jpn. J. Appl. Phys.*, vol. 31, p. L139 (1992).

[37] S. Nakamura, M. Senoh, and T. Mukai, *Jpn. J. Appl. Phys.*, vol. 30, p. L1708 (1991).

[38] Y. P. Varshni, *Physica*, vol. 34, pp. 149 (1967).

[39] H. Morkoc S. Strite, G. B. Gao, M. E. Lin, B. Sverdlov, and M. Burns, *J. Appl. Phys.*, vol. 76, no. 3, pp. 1363 (1994).

[40] S. Strite, M. E. Lin, and H. Morkoc, *Thin Solid Films*, vol. 231, pp.

197 (1993).

[41] H. P. Maruska, and J. J. Tietjen, *Appl. Phys. Lett.*, vol. 15, pp. 327 (1996).

[42] H. Teisseyre, P. Perlin, T. Suski, I. Grzegory, S. Porowski, J. Jun, A. Pietraszko, and T. D. Moustakas, *J. Appl. Phys*, vol. 76, pp. 2429 (1994).

[43] M. O. Manasreh, *Phys. Rev. B*, vol. 53, pp. 16425 (1996).

[44] B. Monemear, *Phys. Rev. B*, vol. 10, pp. 676 (1974).

[45] J. Petalas, S. Logothetidis, and S. Boultadakis, M. Alouani, and J. M. Wills, *Phys. Rev. B*, vol. 52, pp. 8082 (1995).

[46] S. N. Mohammad, A. A. Salvador, and H. Morkoc, *Proc. of the IEEE*, vol. 83, no. 10, pp. 1306 (1995).

[47] Q. Guo, and A. Yoshida, *Jpn. J. Appl. Phys.*, vol. 33, pp. 2453 (1994).

[48] W. M. Yim *et al.*, *J. Appl. Phys.*, vol. 44, pp. 292 (1973).

[49] P. B. Perry, and R. F. Rutz, *Appl. Phys. Lett.*, vol. 33, pp. 319 (1978).

[50] T. Matsuoka, H. Okamoto, M. Nakao, H. Harima, and E. Kurimoto, *Appl. Phys. Lett.*, vol. 81, pp. 1246 (2002).

[51] T. Matsuoka, M. Nakao, H. Okamoto, H. Harima, and E. Kurimoto, *Jpn. J. Appl. Phys.*, vol. 42, pp.2288 (2003).

[52] S. Strite *et al.*, *J. Cryst. Growth*, vol. 127, pp. 204 (1993).

[53] S. Yoshida, S. Misawa, and S. Gonda, *J. Appl. Phys.*, vol. 53, pp. 6844 (1982).

[54] J. Hagen, R. D. Metcalfe, D. Wickenden, and W. Clark, *J. Phys. C*, vol. 11, p. L143 (1978).

[55] Y. Kiode, H. Itoh, M. R. H. Khan, K. Hiramatu, N. Sawaki, and I. Akasaki, *J. Appl. Phys.*, vol. 61, pp. 4540 (1987).

[56] M. A. Khan, R. A. Scogmam, R. G. Schulze, and M. Gershenzon,

*Appl. Phys. Lett.*, vol. 43, pp. 492 (1983).

[57] D. K. Wickenden, C. B. Bargeron, W. A. Bryden, and J. Miragliotta, *Appl. Phys. Lett.*, vol. 65, pp. 2024 (1994).

[58] S. R. Lee, A. F. Wright, M. H. Crawford, G. A. Petersen, J. Han, and R. M. Biefeld, *Appl. Phys. Lett.*, vol. 74, pp. 3344 (1999).

[59] A. F. Wright, and J. S. Nelson, *Appl. Phys. Lett.*, vol. 66, pp. 3051 (1995).

[60] G. Steude, B. K. Meyer, A. Göldner, A. Hoffmann, F. Bertram, J. Christen, H. Amano, and I. Akasaki, *Appl. Phys. Lett.*, vol. 74, pp. 2456 (1999).

[61] H. Angerer, D. Brunner, F. Freudenberg, O. Ambacher, M. Stutzmann, R. Höpler, H. Metzger, E. Born, G. Dollinger, A. Bergmaier, S. Karsch, and H. -J. Körner, *Appl. Phys. Lett.*, vol. 71, pp. 1504 (1997).

[62] D. Brunner, H. Angerer, E. Bustarret, F. Freudenberg, R. Höpler, R. Dimitrov, O. Ambacher, and M. Stutzmann, *J. Appl. Phys.*, vol. 82, pp. 5090 (1997).

[63] S. Nakamura M. Senoh, and T. Mukai, *Appl. Phys. Lett.*, vol. 62, pp. 2390 (1993).

[64] S. Nakamura, T. Mukai, and M. Senoh, *J. Appl. Phys.*, vol. 76, pp. 8189 (1994).

[65] S. Nakamura, M. Senoh, N. Iwasa, and S. Nagahama, *Appl. Phys. Lett.*, vol. 67, pp. 1868 (1995).

[66] K. Osamura, K. Nakajima, and Y. Murakami, *Solid State Commun.*, vol. 11, pp. 617 (1972).

[67] K. Osamura, S. Naka, and Y. Murakami, *J. Appl. Phys.*, vol. 46, pp. 3432 (1975).

[68] T. Nagatomo, K. Kuboyama, H. Minamino, and O. Omoto, *Jpn. J. Appl. Phys.*, vol. 28, p. L1334 (1989).

[69] N. Yoshimoto, T. Matsuoka, and A. Katsui, *Appl. Phys. Lett.*, vol. 59, pp.2251 (1991).

[70] W. Shan, W. Walukiewicz, E. E. Haller, B. D. Little, J. J. Song, M. D. McCluskey, N. M. Johnson, Z. C. Feng, M. Schurman and R. A. Stall, *J. Appl. Phys.*, vol.84, pp. 4452 (1998).

[71] H. P. D. Schenk, P. de Mierry, M. Laugt, F. Omnes, M. Leroux, B. Beaumont and P. Gibart, *Appl. Phys. Lett.*, vol. 75, pp. 2587 (1999).

[72] T. Takeuchi, H. Takeuchi, S. Sota, H. Sakai, H. Amano and I. Akasaki, *Jpn. J. Appl. Phys.*, vol. 36, p. L177 (1997).

[73] J. Y. Chang, and Y. K. Kuo, *J. Appl. Phys.*, vol. 93, pp. 4992 (2003).

[74] C. Wetzel, T. Takeuchi, S. Yamaguchi, H. Katoh, H. Amano and I. Akasaki, *Appl. Phys. Lett.*, vol. 73, pp. 1994 (1998).

[75] C. A. Parker, J. C. Roberts, S. M. Bedair, M. J. Reed, S. X. Liu, N. A. El-Masry and L. H. Robins, *Appl. Phys. Lett.*, vol. 75, pp. 2566 (1999).

[76] G. Martin, S. Strite, A. Botchkarev, A. Agarwal, A. Rockett, H. Morkov, W. R. L. Lambrecht, and B. Segall, *Appl. Phys. Lett.*, vol. 65, pp. 610 (1994).

[77] G. Martin, A. Botchkarev, A. Rockett, and H. Morkov, *Appl. Phys. Lett.*, vol. 68, pp. 2541 (1996).

[78] J. Baur, K. Maier, M. Kunzer, U. Kaufmann, and J. Schneider, *Appl. Phys. Lett.*, vol. 65, pp. 2211 (1994).

[79] J. R. Waldrop, and R. W. Grant, *Appl. Phys. Lett.*, vol. 68, pp. 2879 (1996).

[80] S. -H. Wei, and A. Zunger, *Appl. Phys. Lett.*, vol. 69, pp. 2719 (1996).

[81] S. -H. Wei, and A. Zunger, *Appl. Phys. Lett.*, vol. 72, pp. 2011

(1998).

[82] Kuech *et al.*, *J. Appl. Phys.*, vol. 67, pp. 2650 (1990).

[83] J. I. Pankove, and T. D. Moustakas, "*Gallium Nitride (GaN) II - Semiconductors and Semimetals Volume 57*", Academic Press, San Diego, California, USA (1999).

[84] J. A. Majewski, M. Stadele, and P. Vogl, *MRS Internet J. Nitride Semicond. Res.*, vol. 1, pp. 30 (1999).

[85] J. H. Edgar, "*Properties of Group III Nitrides*", Electronic Materials Information Service, London (1994).

[86] K. Shimada, T. Sota, and K. Suzuki, *J. Appl. Phys.*, vol. 84, pp. 4951 (1998).

[87] H. Morkoc, S. Strite, G. B. Gao, M. E. Lin, B. Sverdlov, and M. Burns, *J. Appl. Phys.*, vol. 76, pp. 1363 (1994).

[88] K. Kim, W. R. L. Lambrecht, and B. Segall, *Phys. Rev. B*, vol. 53, pp. 16310 (1996).

[89] A. F. Wright, and J. S. Nelson, *Phys. Rev. B*, vol. 50, pp. 2159 (1994).

[90] D. Vogel, P. Kruger, and J. Pollmann, *Phys. Rev. B*, vol. 55, pp. 12836 (1997).

[91] K. Miwa, and A. Fukumoto, *Phys. Rev. B*, vol. 48, pp. 7897 (1993).

[92] M. Suzuki, and T. Uenoyama, *Appl. Phys. Lett.*, vol. 69, pp. 3378 (1996).

[93] A. S. Barker, Jr. and M. Ilegems, *Phys. Rev. B*, vol. 7, pp. 743 (1973).

[94] M. Suzuki, and T. Uenoyama, *Jpn. J. Appl. Phys.*, vol. 34, pp. 3442 (1995).

[95] Y. C. Yeo, T. C. Chong, and M. F. Li, *J. Appl. Phys.*, vol. 83, pp. 1429 (1998).

[96] C. P. Foley, and T. L. Tansley, *Phys. Rev. B*, vol. 33, pp. 1430

(1986).

[97] 史光國編著 “現代半導體發光及雷射二極體材料技術” 全華科技圖書股份有限公司 (2002)。

[98] S. Nakamura, *Jpn. J. Appl. Phys.*, vol. 30, pp. 1620 (1991).

[99] S. Nakamura, M. Senoh, N. Iwasa, S. Nagahama, T. Yamada, T. Mukai1, *Jpn. J. Appl. Phys.*, vol. 34, p. L1332 (1995).

[100] T. Mukai, *IEEE J. on Sel. Top. in Quantum Electron.*, vol. 8, pp. 264 (2002).

[101] S. Miyoshi, H. Yaguchi, K. Onabe, and R. Ito, *Appl. Phys. Lett.*, vol. 63, pp. 3506 (1993).

[102] J. N. Baillargeon, K. Y. Cheng, *J. Appl. Phys.*, vol. 70, pp. 1841 **(**1991).

[103] J. N. Baillargeon, K. Y. Cheng, G. E. Hofler, P. J. Pearch, and K. C. Hsieh, *Appl. Phys. Lett.*, vol. 60, pp. 2540 (1992).

[104] T. Egawa, B. Zhang, N. Nishikawa, H. Ishikawa, and T. Jimbo, *IEEE IDEM*, pp. 205 (2001).

[105] T. Mukai, H. Narimatsu, and S. Nakamura, *Jpn. J. Appl. Phys.*, vol. 37, p. L479 (1998).

[106] T. Mukai, M. Yamada, and S. Nakamura, *Jpn. J. Appl. Phys.*, vol. 38, pp. 3976 (1999).

[107] J. K. Sheu, S. J. Chang, C. H. Kuo, Y. K. Su, L. W. Wu, Y. C. Lin, W. C. Lai, J. M. Tsai, G. C. Chi, and R. K. Wu, *IEEE Photonic. Tech. Lett.*, vol. 15, pp. 18 (2003).

[108] A. Kinoshita, H. Hirayama, M. Ainoya, Y. Aoyagi, and A. Hirata, *Appl. Phys. Lett.*, vol. 77, pp. 175 (2000).

[109] T. Wang, Y. H. Liu, Y. B. Lee, J. P. Ao, J. Bai, and S. Sakai, *Appl. Phys. Lett.*, vol. 81, pp. 2502 (2002).

[110] T. Nishida, H. Saito, and N. Kobayashi, *Appl. Phys. Lett.*, vol. 79, pp. 711 (2001).

[111] J. Han, M. H. Crawford, R. J. Shul, J. J. Figiel, L. Zhang, Y. K. Song, H. Zhou, and A. V. Nurmikko, *Appl. Phys. Lett.*, vol. 73, pp. 1688 (1998).

[112] S. Nakamura, M. Senoh, S. Nagahama, N. Iwasa, T. Yamada, T. Matsushita, H. Kiyoku, and Y. Sugimoto, *Jpn. J. Appl. Phys.*, vol. 35, p. L74 (1996).

[113] S. Nakamura, M. Senoh, S. Nagahama, N. Iwasa, T. Yamada, T. Matsushita, H. Kiyoku, and Y. Sugimoto, *Jpn. J. Appl. Phys.*, vol. 35, p. L217 (1996).

[114] S. Nakamura, M. Senoh, S. Nagahama, N. Iwasa, T. Yamada, T. Matsushita, H. Kiyoku, and Y. Sugimoto, *Appl. Phys. Lett.*, vol. 68, pp. 2105 (1996).

[115] S. Nakamura, M. Senoh, S. Nagahama, N. Iwasa, T. Yamada, T. Matsushita, H. Kiyoku, and Y. Sugimoto, *Appl. Phys. Lett.*, vol. 68, pp. 3269 (1996).

[116] S. Nakamura, M. Senoh, S. Nagahama, N. Iwasa, T. Yamada, T. Matsushita, Y. Sugimoto, and H. Kiyoku, *Appl. Phys. Lett.*, vol. 69, pp. 1477 (1996).

[117] S. Nakamura, M. Senoh, S. Nagahama, N. Iwasa, T. Yamada, T. Matsushita, Y. Sugimoto, and H. Kiyoku, *Appl. Phys. Lett.*, vol. 69, pp. 4056 (1996).

[118] S. Nakamura, M. Senoh, S. Nagahama, N. Iwasa, T. Yamada, T. Matsushita, Y. Sugimoto, and H. Kiyoku, *Appl. Phys. Lett.*, vol. 70, pp. 1417 (1997).

[119] S. Nakamura, M. Senoh, S. Nagahama, N. Iwasa, T. Yamada, T. Matsushita, Y. Sugimoto, and H. Kiyoku, *Jpn. J. Appl. Phys.*, vol. 36, p. L1059 (1997).

[120] S. Nakamura, M. Senoh, S. Nagahama, N. Iwasa, T. Yamada, T. Matsushita, H. Kiyoku, Y. Sugimoto, T. Kozaki, H. Umemoto, M. Sano, and K. Chocho, *Appl. Phys. Lett.*, vol. 72, pp. 211 (1998).

[121] S. Nakamura, M. Senoh, S. Nagahama, N. Iwasa, T. Yamada, T. Matsushita, H. Kiyoku, Y. Sugimoto, T. Kozaki, H. Umemoto, M. Sano, and K. Chocho, *Jpn. J. Appl. Phys*., vol. 36, p. L1568 (1997).

[122] S. Nakamura, N. Iwasa, M. Senoh, T. Matsushita, Y. Sugimoto, H. Kiyoku, T. Kozaki, M. Sano, H. Matsumura, H. Umemoto, K. Chocho, and T. Mukai, *Jpn. J. Appl. Phys.*, vol. 39, p. L647 (2000).

[123] S. Nakamura, M. Senoh, S. Nagahama, N. Iwasa, T. Yamada, T. Matsushita, H. Kiyoku, Y. Sugimoto, T. Kozaki, H. Umemoto, M. Sano, and K. Chocho, *Jpn. J. Appl. Phys.*, vol. 37, p. L1020 (1998).

[124] S. Nakamura, M. Senoh, S. Nagahama, N. Iwasa, T. Matsushita, and T. Mukai, *Appl. Phys. Lett.*, vol. 76, pp. 22 (2000).

[125] S. L. Chuang, and C. S. Chang, *Semiconductor Science and Technology*, vol. 12, pp. 252 (1997).

[126] G. Martin, A. Botchkarev, A. Rockett, and H. Morkoc, *Appl. Phys. Lett.*, vol. 68, pp. 2541 (1996).

[127] J. H. Edgar ed., "*Properties of Group III nitrides*", IEE/ INSPEC, London (1994).

[128] K. Domen, R. Soejima, A. Kuramata, and T. Tanahashi, *MRS Internet J. Nitride Semicond. Res.*, vol. 3, pp. 2 (1998).

[129] H. Y. Zhang, X. H. He, Y. H. Shih, M. Schurman, Z. C. Feng, and R. A. Stall, *Optics Lett.*, vol. 21, pp. 1529 (1996).

[130] R. K. Sink, Ph.D. Thesis, Electrical and Computer Engineering, Univeristy of California at Santa Barbara (2000).

[131] T. Asano, M. Takeya, T. Tojyo, T. Mizuno, S. Ikeda, K. Shibuya, T. Hino, S. Uchida, and M. Ikeda, *Appl. Phys. Lett.*, vol. 80, pp. 3497 (2002).

[132] T. Asano, T. Tojyo, T. Mizuno, M. Takeya, S. Ikeda, K. Shibuya, T. Hino, S. Uchida, and M. Ikeda, *IEEE J. Quantum Electron.*, vol. 39, pp. 135 (2003).

# Appendix A.　User Guides of LASTIP

*LASTIP* 軟體的全名為 LASer Technology Integrated Program，其出品公司為加拿大的 Crosslight 公司，它是一套能夠模擬二維半導體相關元件的商用套裝軟體。此一軟體在操作上可經由輸入已知的材料參數及結構，就可以獲得多項關於雷射的光電特性。因此只要建立足夠且適當的物理模式（physical models），並且輸入正確的材料參數，這一套軟體將可以作為一套設計最佳化半導體元件或者是評估新穎的系統結構相當有用的工具。接下來將針對此一模擬軟體的各項功能及特性作一些基本的說明。

## A.1、材料系統與參數設定

*LASTIP* 軟體可提供使用者模擬之各項材料與其材料參數（包含塊材與量子井結構）均設定在 crosslight.mac 的巨集檔案中。通常在安裝完成 *LASTIP* 模擬軟體後，此一巨集檔會出現在 C:\crosslig\lastip 的資料夾裡，雖然軟體本身內建的材料參數已經相當完整，但是在有需要的情況下仍然可以經由自行修改或線上下載的方式對其進行更新，使用者必須注意的是在模擬一系統材料時，其有關此一材料之所有參數如能帶計算公式、折射率…等最好都必須有論文提供依據，以便於投稿時有參考文獻。軟體內建的材料系統相當多元化，使用者只需在軟體已經建構好的架構下進行修改即可，然而其語法必須與原程式相

同，且較新之材料如以 InGaAsN 做為光纖通訊用 1.3 μm 之半導體雷射量子井材料；舊有之巨集檔並沒有提供，因此使用者必須自行收集有關此一材料之所有參數，建立新的材料系統便可模擬。

## A.2、程式所能模擬的系統、結構

*LASTIP* 所能模擬的原件結構相當開放，使用者可以利用圖形操作介面（graphic user interface）或者是直接撰寫程式的方式建立所需模擬的結構，再利用程式內建的轉檔功能將建立好的結構轉換成程式的內部語言，依固定的模擬程序就可以得到所設計之雷射原件相關特性；然而較複雜之原件結構如三五族氮化物之 p 型與 n 型電極必須都在上方的脊狀結構(ridge)，程式目前還無法模擬。原則上 *LASTIP* 所能模擬的元件系統結構如下（不限波長與材料）：

(1) Fabry-Perot（FP）雷射；
(2) Distributed Feedback（DFB）雷射；
(3) Gain-Coupled DFB 雷射；
(4) Distributed Bragg Reflector（DBR）雷射；
(5) Multielectrode Distributed Feedback（MEDFB）雷射；
(6) Semiconductor Optical Amplifiers；
(7) Light Emitting Diodes（LEDs）；

## A.3、理論計算與原理

*LASTIP* 軟體的計算方式是利用各種的特性方程式（物理模型）來

架構出模擬的各項特性與結果；所包含的式子包括基本的 Poisson 方程式、連續方程式、光場分佈方程式以及雷射腔內的光子分佈等等，以及一些描述載子特性、邊界特性…等的理論公式。上述的理論公式與模型在使用手冊中均有概略的介紹，但是由於其內容敘述的不夠詳盡，因此尚需搭配半導體物理相關書籍一併閱讀。各方程式彼此之間的關聯及其相關的參數系統如下圖所示。

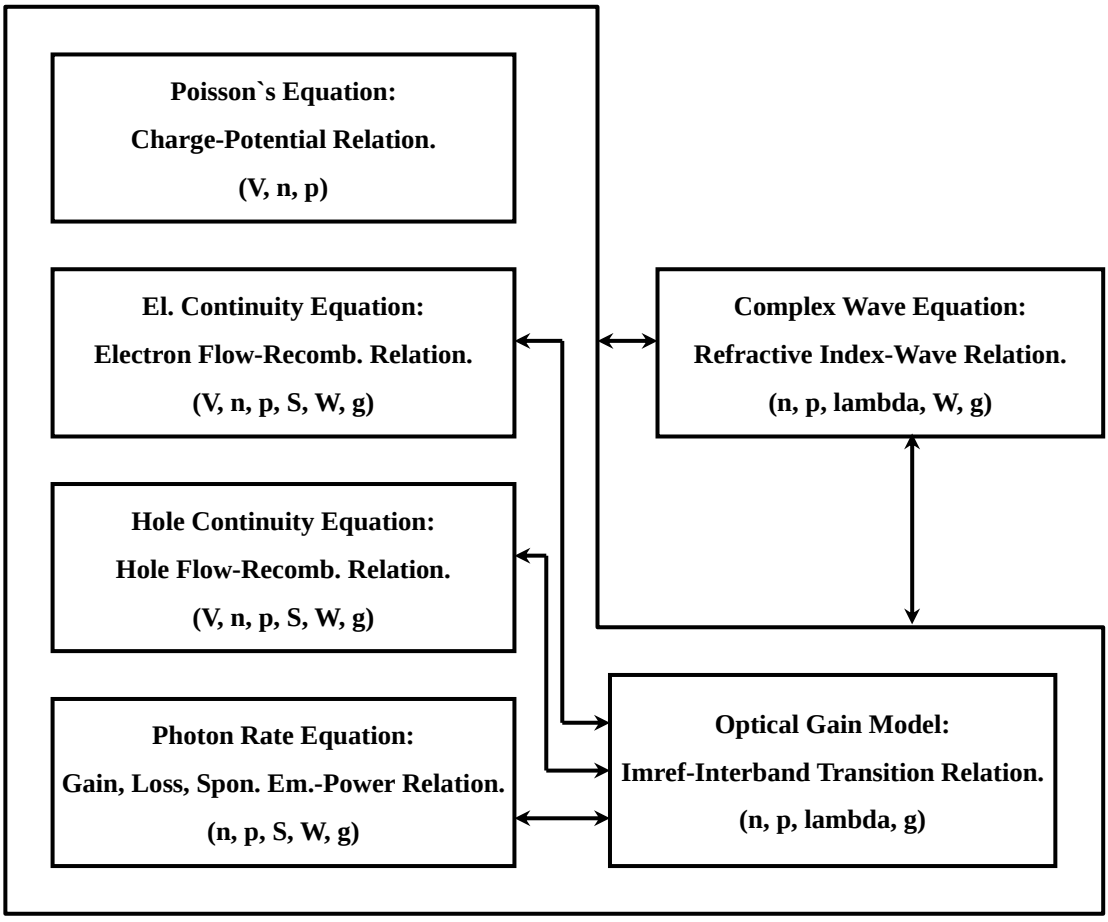


其中 V 代表電位，n 與 p 則代表電子與電洞之濃度。光子數目與光場強度分別以 S 與 W 來表示，lambda 代表波長，增益值則表示為 g。

## A.4、模擬所能獲得的結果與資料

在輸入合適的材料參數與結構設定, 並且經由上述的理論計算過程後，我們可以獲得下列的模擬結果與資料：

(1) 輸出能量與電流之關係；
(2) 電流與電壓之關係；
(3) 二維的電位、電場與電流分佈；
(4) 二維的電子與電洞濃度分佈；
(5) 不同電壓下之能帶結構；
(6) 價電帶混合模式下之量子井次能帶結構；
(7) 二維的深層能階所捕獲載子之分佈；
(8) 二維的光場分佈；
(9) 二維的區域性光增益分佈；
(10) 不同電流輸入下之增益頻譜；
(11) 不同電流輸入下之自發輻射頻譜；
(12) 遠場分佈；
(13) 上述所有資料隨時間之變化；
(14) 上述所有資料在不同溫度下之變化；

以上所有的模擬結果均可以利用圖檔或純文字檔案的方式輸出，以利於更一步的分析、處理。

## A.5、主要操作程序與流程

*LASTIP* 軟體主要的操作程序是利用輸入元件的材料系統、結構設定以及一些初始參數，再經過檔案轉換的過程將原始的輸入檔轉成程

式內部計算用的語言後，便可以執行模擬。詳細的操作流程如下圖所示，其中方框內的文字敘述與軟體面板上操作按鈕的文字均一致。直得注意的是，在操作 *LASTIP* 軟體模擬元件之主要發光波長時，.gain 檔是可先行獨立被操作，亦即使用者可執行有關於.gain 檔的步驟，來決定元件在此發光波長下活性層該如何設計，而後再將此一活性層設計(包含量子井寬度與材料各成分比濃度)輸入至.layer 檔內，再依如下所示步驟進行模擬，即可得到模擬結果。

**附註：**

斜線方框指的是模擬所必備的步驟。白色方框則是執行與否均不會影響到最後模擬結果的步驟。

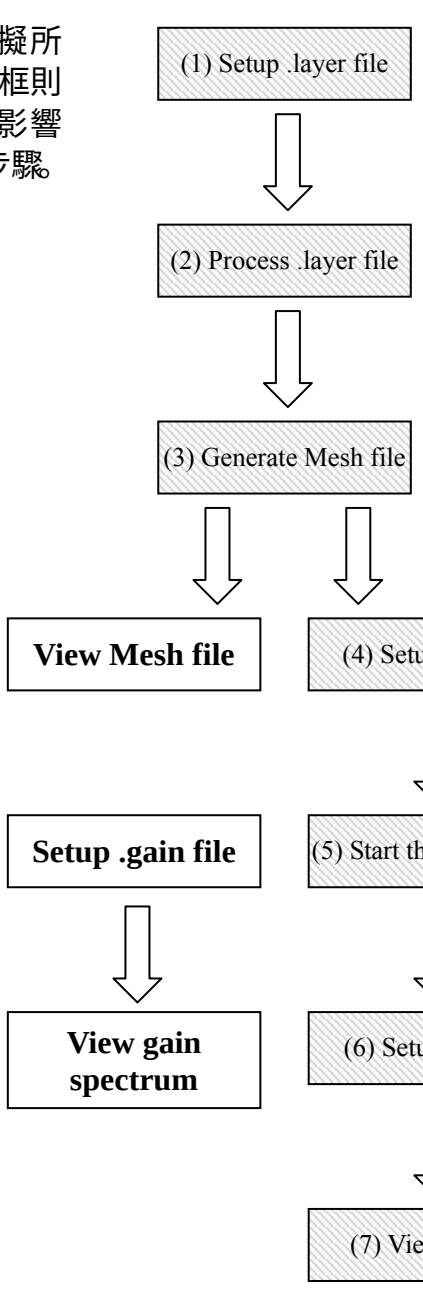


利用圖形操作介面或是直接撰寫的方式建立最初始的輸入檔：.layer 檔。

將.layer 檔轉換成程式內部計算用的語言。此一步驟將產生四個與材料以及結構有關的檔案：.geo、.mater、.doping、.mplt。

執行.geo 檔，以建立微方程計算時的分隔區域。此一步驟會產生.msh 檔。

以圖檔的方式顯示出.msh 檔所建立的區域。此一步驟可以省略。

建立.sol 檔。設定元件模擬的初始參數以及運算方式。

設定元件的增益檔，.gain 檔。

正式開始模擬，產生.out_i 檔；這些檔案是所有模擬結果之數據所在。

執行.gain 檔，輸出該材料系統之增益頻譜以及自發輻射頻譜。

將所要輸出的圖形或數據建立在.plt 檔中。

執行.plt 檔，輸出所需要結果的圖形或數據。

### A.5.1 步驟一：建立.layer 檔

利用簡單的程式語言架構起元件的結構、材料成份，是最初始的輸入檔。建立.layer 檔的方法常用的有兩種，一種是先利用程式內建的圖形操作介面（直接執行〝Draw GUI〞，就會開啟此一介面。）架構起整個結構，再轉換檔案成.layer 檔；另外一種方式則是直接撰寫.layer 檔。一般而言，如果是要建立新的結構，往往會使用前者的方式；如果只是要對舊結構作稍許的修改或調變材料成份，則直接修改.layer 檔會比較方便（在 *LASTIP* 軟體中，所有參數的單位均設定為 MKS 制）。

#### A.5.1.1 直接撰寫.layer 檔

程式中以 column 代表元件的縱向橫截面特性；大部份的光電半導體元件只需要一個 column 即足以描述其系統結構，但是在某些特殊結構的情況下（如氮化物元件的脊狀結構）則需要用到兩個或以上的 column。其中 w 指的是 column 的寬度，mesh_num 與 r 則是指電腦在進行差分計算時所區分的網目數目以及網目分佈的等比級數，網目的數目越多則模擬結果越準確，但所需要的計算時間也就越多，而且有時設定過大的網目數目時，在執行程式時有時會因為記憶體不足而無法進行模擬，一般而言網目數目大多設定在 10 以下。在.layer 檔第一行指令內 column 這一段中所輸入的網目數值代表整個 column 橫向的網目分佈，而在元件中各結構層中所輸入的數值(如 n = 3)則代表各層縱向的網目分佈。程式會依據我們所輸入的 mesh_num 與 r 值來對網

目進行等比分佈（由下到上、由左至右），因此若輸入的 r 值為 1，則代表網目均勻分佈，若 r 值小於 1，則表示網目分佈越來越密。一般來說，我們常將活性區下方薄膜的 r 值設定為小於 1，活性區上方薄膜的 r 值則設為大於 1，以增加活性區邊界區域的計算（其他區域，包括活性區，都將 r 值設定為 1。）。

程式中的電極設定以 bottom_contact 以及 top_contact 表示；我們可以在這裡設定電極的橫向範圍（from、to），邊界參數（contact_num）以及電極型式（contact_type）等等，其中電極型式可以設定為 ohmic 以及 schottky 兩種。

*LASTIP* 程式在設定結構時主要是依據由下到上、由左至右的原則，將整體結構分成各層（layer）來加以個別設定。在各層中可以輸入材料名稱（macro_name)、成份比例（var1、var2…）以及該層厚度（d)、摻雜濃度（n_doping1 或 p_doping1）等參數；由於程式會依據所輸入的材料名稱自動至 crosslight.mac 檔案中載入所有的材料參數，因此這裡所輸入的材料名稱必須跟巨集檔內該檔案中的名稱設定一致，如以巨集檔名稱 ingaasp_xy 為例，於.layer 中使用此一結構層時，就必須輸入 var1 =, var2 =，其中 var1 與 var2 分別表示 ga 與 as 的成分比濃度，否則在執行程式轉檔時就會出現錯誤訊息，使用者必須熟練程式，當程式出現各種錯誤訊息時要有能力找出錯誤所在加以修正。

此外，在某些層中會特別設定 xp1 以及 xp2 兩個參數，其所代表意義是指對邊界進行額外更詳細的計算（extr_mesh_point）；其中 xp1 代

表的是此一層的下邊界，xp2 則為上邊界。將此一數值設定為 1 則代表開啟此一額外計算功能，設定為 0 或者根本不設定此一參數則代表不使用額外計算功能。在正常的情況下，我們只在活性區以及最靠近活性區的邊界使用此一功能。

活性層的設定跟上述各層的設定極為相似，只是要多設定活性材料（active_macro）及其成份比例（avar1、avar2…）。其中活性材料若為塊材，則直接輸入其材料名稱；活性材料若為量子井結構，則需以 A/B 的形式輸入，A 為活性層材料(well)，B 為披覆層材料(barrier)。相關的材料名稱可參考 crosslight.mac 檔或使用手冊之說明。

以上就是.layer 檔的概略介紹以及參數說明，完整的檔案內容可參考附錄 B 之資料。如果還有任何不夠詳盡的地方，請直接參考 *LASTIP* 軟體之使用手冊或請教資深學長姐。

#### A.5.1.2 圖形操作介面

由於圖形操作介面相當簡單明瞭，只需要在程式所指定的空格中輸入參數即可，再加上使用手冊中也有清楚的說明，因此接下來的部份將只針對其轉檔過程中所會產生的兩個錯誤進行說明。

當我們在圖形操作介面建立好元件的結構及參數設定後，只要存檔就會自動產生三個同檔名的檔案：.layer 檔、.ascii 檔、.gui 檔，其中所產生的.layer 檔中會出現兩個程式錯誤：

(1) extr_mesh_point 設定錯誤：凡是 xp2 均會被誤設為 xp1。

(2) 活性材料的成份比例之參數名稱錯誤：原本應為 avar1、avar2…，但經轉檔後卻誤為 var1、var2…。

因此使用者需在轉檔完成後手動更正這些錯誤。

### A.5.2 步驟二：Process .layer file

此一步驟是將初始的輸入檔（.layer 檔）轉換成 *LASTIP* 內部所使用的語言，經由此一步驟會產生.geo 檔、.mater 檔、.doping 檔以及.mplt 檔四個檔案。這些檔案個別描述元件的結構、材料、摻雜濃度…等特性，並且會被使用在之後的正式模擬中。

### A.5.3 步驟三：Generate Mesh file

此一步驟是將上述的.geo 檔轉換成.msh 檔，也就是將網目分佈的資料轉換成電腦所能運算的檔案。完成後還可以利用〝View Mesh file〞的步驟來觀看元件的網目分佈（此一步驟的完成與否並不會影響到模擬結果，因此往往被省略掉）。

### A.5.4 步驟四：Setup .sol file

此一檔案是模擬過程中最主要的輸入檔，大部份的計算時間都會花費在這裡。.sol 檔的建立可以利用程式內建的交談式介面（直接執行〝Setup .sol file〞即可開啟此一介面），依其指示一步一步輸入，或者是直接撰寫的方式。由於.sol 檔的內容比較簡單且沒有變化，因此我們大部份都利用舊有的檔案來直接加以修改，再變更檔案名稱即可。

檔案的一開始是在載入之前已經設定好的結構與參數，如.msh 檔、.mater 檔以及.doping 檔，並將模擬結果資料設定為以.out 檔的型式輸出。接著再設定牛頓法的非線性參數（newton_par），如 damping_step、max_iter 等；除非特殊需要，否則這些參數不會被改變。

init_wave 的設定則是在輸入解波方程時的一些初始值，其中 point_ll 與 point_ur 代表解波方程時所要計算的方形區域（point_ll 為下方、左邊的邊界點，point_ur 則為上方、右邊的邊界點），此一區域必須小於或等於之前所輸入的元件大小；fld_center 則是預計的光學模式中心（optical mode center），此一數值僅僅只是一個初始值，程式在執行的過程中會自動調整至之正確的數值；length 指的是雷射腔長度，由於之前的結構設計與參數設定均是二維的（因為 *LASTIP* 是一個二維的模擬軟體），因此加上此一參數後，就能夠架構成完整的三度空間元件；backg_loss 則為系統的背景損失參數（background loss coefficient），各層的吸收…等效應都包含在此一參數內；init_wavel 與 wavel_range 分別代表預估的雷射輸出波長以及可能的雷射波長範圍，程式會從 init_wavel 的數值開始計算波方程，並在 wavel_range 的範圍中尋找真正的增益波峰；front_back 則是在設定雷射前後反射鏡的反射率，如果此一參數改成 mirror_ref，則表示前後反射鏡的反射率均一致。

接下來所要設定的則是程式作運算時之電壓或電流條件（scan）。如果我們選擇的是電壓，則程式會從初始電壓依不定的間隔（bias step 或 bias interval）增加至最終電壓，並在每一個指定間隔均輸出模擬資

料。value_to 指的是計算過程中的運算終點；print_step 則是上述所謂的指定間隔（電壓間隔或電流間隔…等），程式會在每個指定間隔將模擬所得的資料輸出至電腦中（以.out 檔的型式輸出）；min_step 以及 max_step 則是模擬所允許的最小與最大的條件間隔。

跟 A.5.1 小節一樣，本小節的內容是選擇較常用在.sol 檔中的參數來加以說明，如果需要用到其他的參數或指令，可以在使用手冊中找到相關的說明。

### A.5.5 步驟五：Start the simulation

在執行此一步驟後，*LASTIP* 程式開始正式進行模擬，並將模擬所得的結果以.out 檔的型式紀錄在硬碟中。當程式進行運算的時候，所有的運算進度會以及時顯示或存成 report 檔的方式顯示出來，因此如果程式執行的過程中有任何的錯誤、問題都可以從其中看出端倪，再依 report 黨所告知之錯誤或原因對.layer 或.sol 檔進行修改即可。Crossligh 公司也額外提供當使用者遇到模擬上的困難而無法解決時的線上詢問功能，不過只要使用者熟悉此一軟體，任何問題必可自行解決。

### A.5.6 步驟六：Setup .plt file

此一步驟是在設定欲輸出模擬結果的輸入檔。在上一步驟中我們已經獲得全部的模擬結果資料（.out 檔），而在這裡則是要設定哪些資訊是我們所想要的，然後在下一個步驟將這些選定的資訊從.out 檔中解析出來，並以圖形或資料點的方式呈現在我們面前。

要設定.plt 檔仍然有兩種主要方式，一種就是直接執行程式中的 Setup .plt file 以開啟程式內建的交談式介面，並依其指示一步步輸入；另外一種方式則是手動撰寫.plt 檔。跟.layer 檔一樣，如果是要建立新的.plt 檔，則建議使用前者的方式；相反的，如果所要取得的資訊都一樣，則建議以直接修改.plt 檔的方式會比較方便。

### A.5.7 步驟七：View results

執行上述的.plt 檔以取得.out 檔中所紀錄的資料。

## A.6、405-nm 雙量子井雷射之模擬原始檔

### A.6.1、.layer檔

```
begin_layer
$
column column_num=1 w=5.0 mesh_num=3 r=1
$
bottom_contact column_num=1 from=0.0 to=5.0 contact_num=1 &&
  contact_type=ohmic
$
top_contact column_num=1 from=0.0 to=5.0 contact_num=2 &&
  contact_type=ohmic
$
layer_mater macro_name=gan column_num=1
layer d=3 n=3 r=1.0 n_doping1=1.0e+024
$
layer_mater macro_name=ingan column_num=1 var1=0.1
layer d=0.1 n=3 r=1.0 n_doping1=1.0e+024
$
```

```
layer_mater macro_name=algan column_num=1 var1=0.14
layer d=0.4 n=3 r=1.0 n_doping1=1.0e+024
$
layer_mater macro_name=gan column_num=1
layer d=0.1 n=3 r=0.3 xp2=1 n_doping1=1.0e+024
$
layer_mater macro_name=ingan column_num=1 var1=0.03
layer d=0.004 n=3 r=1.0 xp1=1 xp2=1
$
layer_mater macro_name=ingan column_num=1 var1=0.1 &&
   active_macro=InGaN/InGaN &&
   avar1=0.1 avar2=0.03 avar3=300
layer d=0.002 n=3 r=1.0 xp1=1 xp2=1
$
layer_mater macro_name=ingan column_num=1 var1=0.03
layer d=0.004 n=3 r=1.0 xp1=1 xp2=1
$
layer_mater macro_name=ingan column_num=1 var1=0.1 &&
   active_macro=InGaN/InGaN &&
   avar1=0.1 avar2=0.03 avar3=300
layer d=0.002 n=3 r=1.0 xp1=1 xp2=1
$
layer_mater macro_name=ingan column_num=1 var1=0.03
layer d=0.004 n=3 r=1.0 xp1=1 xp2=1
$
layer_mater macro_name=algan column_num=1 var1=0.16
layer d=0.02 n=3 r=1.7 xp1=1 p_doping1=0.5e+024
$
layer_mater macro_name=gan column_num=1
layer d=0.05 n=3 r=1.0 p_doping1=0.5e+24
$
layer_mater macro_name=algan column_num=1 var1=0.14
layer d=0.4 n=3 r=0.3 xp2=1 p_doping1=0.5e+24
$
layer_mater macro_name=gan column_num=1
```

```
layer d=0.1 n=3 r=1.0 p_doping1=0.5e+24
$
end_layer
```

### A.6.2、.gain 檔

```
$file:A0526a.gain
begin_gain
plot_data plot_device=data_file
$ plot_data plot_device=postscript
get_active_layer name=InGaN/InGaN &&
   var1=0.100E+00 &&
   var2=0.03 &&
   var3=0.30E+03 &&
   mater=1
active_reg type=macro &&
   mode=te &&
   thickness=0.002 &&
   tau_scat=0.1000E-12 &&
   exch_coef=0.e-10 mater=1
gain_wavel wavel_range=[ 0.3 0.5] &&
   conc_range=[    0.1000E+23    0.1000E+27] &&
   curve_number= 5      data_file=gain.txt
sp.rate_wavel wavel_range=(0.3 0.5) &&
   conc_range=(1.e20 1.e20)    curve_number=1 &&
   data_point=1000      data_file=spon.txt
end_gain
```

### A.6.3、.sol 檔

```
$file:A0526a.sol
begin
load_mesh mesh_inf=A0526a.msh
include file=A0526a.mater
include file=A0526a.doping
output sol_outf=A0526a.out
```

```
newton_par damping_step=5. max_iter=100 print_flag=3
sor_par    max_iter=000 print_sor=noprint
init_wave point_ll=[    0.0000E+00    0.0000E+00] &&
   point_ur=[5 4.186] &&
   fld_center=[2.5 3.605] &&
   length= 500    backg_loss=4200 &&
   boundary_type=[2 2 1 1] init_wavel= 0.405E+00 &&
front_back=[0.3 0.3] &&
   wavel_range=[    0.3E+00    0.5E+00]
equilibrium
newton_par damping_step=3 var_tol=1e-7 res_tol=1e-7 &&
max_iter=50 opt_iter=15 stop_iter=17 print_flag=3
scan var=voltage_1 value_to= -0.2840E+01 print_step=0.2840E+01 &&
   init_step=    0.5679E+00 min_step=1.e-5 max_step=0.5
scan var=current_1 value_to=1000 print_step=100 &&
   init_step=    0.2000E+01 min_step=2.e-5 max_step=    0.2000E+02
$
multimode mode_num=4 boundary_type1=(2 1 1 1) &&
   boundary_type2=(1 1 1 1)
$
end
```

### A.6.4、.plt 檔

```
$file:A0526a.plt
begin_pstprc
plot_data plot_device=postscript
get_data    main_input=A0526a.sol &&
   sol_inf=A0526a.out &&
   xy_data=[ 12 12] scan_data=[1 12]
plot_1d variable=elec_conc &&
   from=[    0.5000E+01    0.0000E+00] &&
   to=[    0.5000E+01    0.41680E+00] &&
   xrange=[    0.0000E+00    0.41680E+00]
plot_1d variable=potential &&
```

```
   from=[    0.5000E+01    0.0000E+00] &&
   to=[    0.5000E+01    0.41680E+00] &&
   xrange=[    0.0000E+00    0.41680E+00]
plot_1d variable=band &&
   from=[    0.5000E+01    0.0000E+00] &&
   to=[    0.5000E+01    0.41680E+00] &&
   xrange=[    0.0000E+00    0.41680E+00]
plot_1d variable=total_curr_y &&
   from=[    0.5000E+01    0.0000E+00] &&
   to=[    0.5000E+01    0.41680E+00] &&
   xrange=[    0.0000E+00    0.41680E+00]
plot_1d variable=field_y &&
   from=[    0.5000E+01    0.0000E+00] &&
   to=[    0.5000E+01    0.41680E+00] &&
   xrange=[    0.0000E+00    0.41680E+00]
plot_1d variable=elec_energy &&
   from=[    0.5000E+01    0.0000E+00] &&
   to=[    0.5000E+01    0.41680E+00] &&
   xrange=[    0.0000E+00    0.41680E+00]
plot_1d variable=acceptor_conc &&
   from=[    0.5000E+01    0.0000E+00] &&
   to=[    0.5000E+01    0.41680E+00] &&
   xrange=[    0.0000E+00    0.41680E+00]
plot_1d variable=recomb_rad &&
   from=[    0.5000E+01    0.0000E+00] &&
   to=[    0.5000E+01    0.41680E+00] &&
   xrange=[    0.0000E+00    0.41680E+00]
plot_1d variable=local_gain &&
   from=[    0.5000E+01    0.0000E+00] &&
   to=[    0.5000E+01    0.41680E+00] &&
   xrange=[    0.0000E+00    0.41680E+00]
plot_1d variable=recomb_st &&
   from=[    0.5000E+01    0.0000E+00] &&
   to=[    0.5000E+01    0.41680E+00] &&
   xrange=[    0.0000E+00    0.41680E+00]
```

```
plot_scan scan_var=voltage_1 &&
   variable=total_curr_1
plot_scan scan_var=current_1 &&
   variable=laser_power
get_data    main_input=A0526a.sol &&
   sol_inf=A0526a.out &&
   xy_data=[1 12] convert_data=yes
end_pstprc
```

# Appendix B.　User Guides of PICS-3D

*PICS-3D*的全名為：Photonic Integrated Circuit Simulator in 3D，是一套可以模擬立體雷射結構的軟體，這套軟體目前實驗室的學長姐主要是用來模擬面射型雷射(VCSEL)元件，模擬所能得到的結果與LASTIP軟體大同小異，只不過要注意的是面射型雷射大致上是屬於圓柱型，雖然在軟體核心程式對於元件的運算方式大致上與*LASTIP*軟體大同小異，對於模擬結果的解釋與其涵蓋的物理意義卻比側射型雷射來的豐富。使用者在模擬前必須先對有關於面射型雷射的半導體物理有相當認識，以及熟練軟體操作，以便遇到問題或是有一新想法時有能力自行解決與模擬。

*PICS-3D*軟體可提供使用者模擬之各項材料與其材料參數（包含塊材與量子井結構）同樣設定在crosslight.mac的巨集檔案中。通常在安裝完成*PICS-3D*模擬軟體後，此一巨集檔會出現在C:\crosslig\pics3d的資料夾裡，雖然軟體本身內建的材料參數已經相當完整，但是在有需要的情況下仍然可以經由自行修改或線上下載的方式對其進行更新，使用者必須注意的是在模擬一系統材料時，其有關此一材料之所有參數如能帶計算公式、折射率…等最好都必須有論文提供依據，以便於投稿時有參考文獻。程式的主要操作程序如下：

**步驟一、建立.layer 檔(Setup layer file)**

這個檔案是將元件架構轉換為程式語言，包含元件中各結構層的厚度、折射率、材料與成分比濃度、摻雜濃度、與損失等。這個檔案通常會配合.well 與.barrier 檔一起使用，其主要目的在於設計元件時，於活性層部分通常為多量子井結構，為節省軟體的運算時間，於計算上會將活性層部分視為單一材料層，再利用 include 指令將 well 和 barrier 結構層納入計算。檔案中以 column 來描述元件長晶面的大小，由於面射型雷射的外觀是屬於圓柱型，因此 w 的值代表元件的半徑(w 值於 *LASTIP* 內代表元件寬度)，如果元件有同心圓（crrent spreading）的結構，第二個 column 的起點就是第一個 column 的終點，各區塊（section）的厚度皆以 d 來表示，top contact 與 bottom contact 來代表上、下的電極（可做成環狀電極），每一層的材料名稱（macro name）與變數（var）必需參照 crosslight.macro 的設定。活性層中的量子井部份（.well 檔）的材料名稱與變數與其他層不同，而且變數的代號變成 avar。

就一個面射型半導體雷射而言，我們可以直接定出 DBR 的材料、折射率、各層的厚度，以及 DBR 的總厚度（各層厚度乘上所設計之對數），而共振腔是由活性層與 spacer 共同組成；活性層部份決定發光的波長，所以我們必需先找出適當的活性層材料、well 與 barrier 的厚度、量子井數目之後，才能進一步定義 spacer 的材料與厚度，因此初步模擬時，在.layer 檔可以先不要建立 spacer 層，待活性層定義出來後再回來補建；或是從舊有的檔案進行改寫，spacer 厚度可先不必計算。一般

而言，DBR 由兩層不同的材料構成，如 GaAs/AlAs，在建立 DBR 的區塊時，會先定義各層的折射率與厚度，材料的變數必需以平均材料來代表，也就是 $Al_{0.5}Ga_{0.5}As$，而此時區塊的厚度則是整個 DBR 的總厚度，必需注意的是，程式每一行的描述不能超過 80 個字元，指令要換行時必須在行末加上“ &&”，否則將被視為另一個指令或是不被程式接受。在每個區塊中，以 n 來表示計算時的網線數目，r 表示網線與網線間的距離比值（距離公比），在運算時電腦會依照公比 r 把一個區塊切成 n 塊。

**步驟二、轉.layer 檔(Process layer)**

經過這個轉換之後會產生 5 個檔案，即.mater、.doping、.geo、.mplt 和.vcsel 等 5 個檔，這個步驟的目的在於把.layer 檔的敘述轉換成程式內部計算用的語言，比如各層的材料、摻雜濃度、幾何形狀、與顯示出網點圖(但此功能在我們目前的程式不提供)等。

**步驟三、轉.geo 檔(Generate mash)**

這個步驟的功用是再進一步把元件的結構告訴電腦，轉完之後會多一個.msh 檔，就是把各網點中的資訊轉給電腦以讓電腦能做運算。

**步驟四、執行.gain 檔(Process gain file)**

這個指令的目的在於測試量子井的設計是否恰當，包括：發光波長是否符合需要、在不同載子濃度下的增益、自發輻射速率等。這個檔

所產生的資料在之後的運算會用得到，檔案中必需輸入想觀察的波長範圍（wave_range）、載子濃度範圍（conc_range）、電子電洞的比例（pn_ratio）與在載子濃度範圍內要觀察的線條數目。如果結果顯示自發輻射的波長不符合要求或是增益太小，就必需回到.well 檔去修改。使用 *PICS-3D* 軟體模擬面射型雷射時，.gain 檔的步驟必須在執行前幾項步驟後才可執行，不同於 *LASTIP* 軟體可先執行.gain 檔決定發光波長，另一項變通的方式是可先以 *LASTIP* 軟體決定所要設計發光波長下，面射型雷射之量子井寬度與成分比濃度，再將量子井寬度與成分比濃度輸入至所要模擬之.layer 檔內，以節省嘗試時間。然而必須注意的是兩套模擬軟體於個別 crosslight.macro 巨集檔內對於活性層材料之參數設定必須一致。

**步驟五、執行.sol 檔(Run simulation)**

跑*.sol 檔，也就是開始解元件物理的部份，包括電性與光學特性，跑*.sol 檔時可以在跑完 rtgain_phase 之後加上 stop 先終止程式，去跑 rtgain 檢查 DBR 的反射率夠不夠高、共振腔的相位對不對、光子與電子是否重疊等，如果結果發現不理想就再回去改*.layer 檔，然後重覆以上的步驟（可以不用再跑*.gain 檔）；如果檢查的結果合乎要求就可以把 stop 去除，繼續跑之後的程式。程式中的 init_step 表示給定的初始值，也就是計算的起點，min_step（max_step）是數值運算時所取的最小（大）間距，value_to 是運算終點，如果運算過程出現任何錯誤或

警告訊息，或者有收斂困難的問題，就必需遵照電腦所提供的指示去修改計算初始值或是計算間距，程式執行的過程可以即時觀測（view log 按鈕，看完後就可關閉視窗不需存檔）。如果遇到程式無法執行而且無任何錯誤訊息，可能是程式內部出了問題，此時必需按 Ctrl+Alt+Delete，然後將 ppmon 全部刪除，再執行一次程式。

# Example：1.55-μm VCSEL with oxidation confined layer

## 1.55-μm 面射型半導體雷射概要結構圖

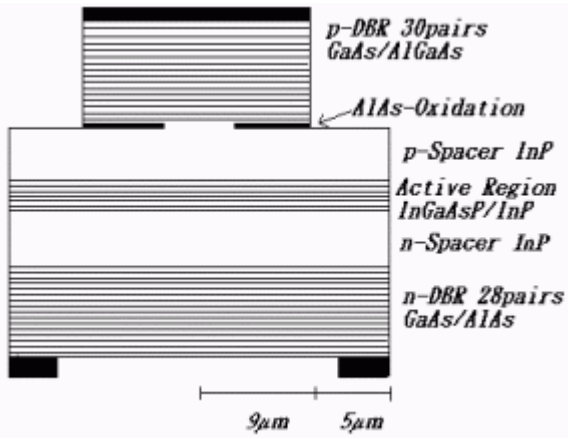


## 1.55-μm 面射型半導體雷射之模擬原始檔

### .layer檔

```
$file:new.layer
$===A simple VCSEL structure===
begin_layer
$
column column_num=1 w=4.0 mesh_num=5 r=1 xp2=1
column column_num=2 w=5.0 mesh_num=5 r=1 xp1=1
column column_num=3 w=5.0 mesh_num=5 r=1 xp1=1
$
bottom_contact column_num=3 from=4.0 to=5.0 contact_num=1
$
vcsel_section vcsel_type=n-dbr &&
   grating_model=layer active=no section_loss=500 &&
   layer1 =0.1145e-6 layer2 =0.131e-6 index1 =3.34 index2 = 2.92 &&
```

```
   mesh_points=5
layer_mater macro_name=algaas.temp var1=0.5 var2=300
column_num=1
layer_mater macro_name=algaas.temp var1=0.5 var2=300
column_num=2
layer_mater macro_name=algaas.temp var1=0.5 var2=300
column_num=3
layer d=6.874    n=6    r=1.0 &&
   n_doping1=2.e24 n_doping2=2.e24 n_doping3=2.e24 vcsel_type=n-dbr
$
vcsel_section vcsel_type=n-spacer &&
   grating_model=layer0 active=no &&
   section_loss=800 section_index=3.167 &&
   mesh_points=5
layer_mater macro_name=inp.temp var1=300 column_num=1
layer_mater macro_name=inp.temp var1=300 column_num=2
layer_mater macro_name=inp.temp var1=300 column_num=3
layer d=0.2126    n=6    r=0.7 xp1=1 &&
   n_doping1=2.e24 n_doping2=2.e24 n_doping3=2.e24
vcsel_type=n-spacer
$
$ MQW system:x5
$
vcsel_section vcsel_type=mqw_active &&
   grating_model=layer0 active=yes &&
   section_loss=5400 section_index=3.277 &&
   mesh_points=10
include file=new.bar
include file=new.well
include file=new.bar
include file=new.well
include file=new.bar
include file=new.well
include file=new.bar
include file=new.well
```

```
include file=new.bar
include file=new.well
include file=new.bar
$
vcsel_section vcsel_type=p-spacer    &&
   grating_model=layer0 active=no    &&
   section_loss=2500 section_index=3.167 &&
   mesh_points=5
layer_mater macro_name=inp.temp var1=300 column_num=1
layer_mater macro_name=inp.temp var1=300 column_num=2
layer_mater macro_name=inp.temp var1=300 column_num=3
layer d=0.2126    n=6    r=1.3 xp2=1 &&
   p_doping1=3.e24 p_doping2=3.e24 p_doping3=3.e24
vcsel_type=p-spacer
$ oxidation confinement layer
vcsel_section vcsel_type=p-dbr-1 &&
   grating_model=layer active=no section_loss=2500 &&
   layer1 =0.1284e-6 layer2 =0.1145e-6 index1 =2.98 index2 =3.34 &&
   mesh_points=5
layer_mater macro_name=algaas.temp var1=0.425 var2=300
column_num=1
layer_mater macro_name=alas_oxide column_num=2
layer_mater macro_name=air column_num=3
layer d=0.2429    n=6    r=1.0 xp1=1 &&
  p_doping1=3.e24 vcsel_type=p-dbr-1
$
vcsel_section vcsel_type=p-dbr-2 &&
   grating_model=layer active=no section_loss=2500 &&
   layer1 =0.1284e-6 layer2 =0.1145e-6 index1 =2.98 index2 =3.34 &&
   mesh_points=5
layer_mater macro_name=algaas.temp var1=0.425 var2=300
column_num=1
layer_mater macro_name=algaas.temp var1=0.425 var2=300
column_num=2
layer_mater macro_name=air column_num=3
```

```
layer d=7.0441    n=6    r=1.0 xp1=1 &&
  p_doping1=3.e24 p_doping2=3.e24 vcsel_type=p-dbr-2
$
top_contact column_num=1 from=0 to=4.0 contact_num=2
top_contact column_num=2 from=0 to=5.0 contact_num=2
$
end_layer
```

**.well 檔**

```
layer_mater macro_name=ingaasp_xy var1=0.24 var2=0.82    &&
   column_num=1 active_macro=InGaAsP/InP &&
   avar1=0.24 avar2=0.82 avar3=0.52 avar4=0.82 avar5=300.
layer_mater macro_name=ingaasp_xy var1=0.24 var2=0.82    &&
   column_num=2 active_macro=InGaAsP/InP &&
   avar1=0.24 avar2=0.82 avar3=0.52 avar4=0.82 avar5=300.
layer_mater macro_name=ingaasp_xy var1=0.24 var2=0.82    &&
   column_num=3 active_macro=InGaAsP/InP &&
   avar1=0.24 avar2=0.82 avar3=0.52 avar4=0.82 avar5=300.
layer d=0.004    n=3    r=1 xp1=1 xp2=1 vcsel_type=mqw_active
```

**.barrier 檔**

```
layer_mater macro_name=ingaasp_xy var1=0.52 var2=0.82 &&
   column_num=1
layer_mater macro_name=ingaasp_xy var1=0.52 var2=0.82 &&
   column_num=2
layer_mater macro_name=ingaasp_xy var1=0.52 var2=0.82 &&
   column_num=3
layer d=0.006    n=3    r=1 xp1=1 xp2=1 vcsel_type=mqw_active
```

**.gain 檔**

```
$file:new.gain
begin_gain
$plot_data plot_device=data_file
```

```
plot_data plot_device=postscript
temperature temp= 0.3E+03
include file=new.mater
gain_wavel wavel_range=(1.3 1.8) &&
   conc_range=[0.8E+24 2E+24]    curve_number=10
sp.rate_wavel wavel_range=(1.3 1.8) &&
   conc_range=[0.8E+24 2E+24]    curve_number=10
index_wavel wavel_range=(1.3 1.8) &&
   init_conc=1.0E+24 &&
   conc_range=[0.8E+24 2E+24]    curve_number=10
current_conc    conc_range=[0.8E+24 2E+24] &&
   data_point=30 &&
   use_macro=yes fit_outfile=tmp.data    data_file=current_conc.txt
end_gain
```

**.sol 檔**

```
$file:new.sol
begin
load_mesh mesh_inf=new.msh
include file=new.gain
include file=new.doping
output sol_outf=new.out
temperature temp=300
$ VCSEL parameters
z_segment zseg_num=1
cylindrical axis=y
vcsel_model index_core= 3.1 &&
   index_cladding=0.1E+01 &&
   core_radius=14.0 bessel_order=0
init_wave backg_loss= 0.5E+04 &&
   init_wavel=1.53 &&
   wavel_range=[1.3 1.8]
sor_par    max_iter=0    print_sor=noprint
$ Set Newton parameters for equilibrium solution
```

```
newton_par damping_step=3. var_tol=1.e-8 res_tol=1.e-8 &&
max_iter=100 opt_iter=15 stop_iter=50 print_flag=3
$ Solve equations at equilibrium
equilibrium
$
rtgain_phase density=1.e24
$ You may stop here to examine the round trip gain
$stop
$ Set Newton parameters for solution with bias
newton_par damping_step=1. var_tol=1.e-2 res_tol=1.e-2 &&
   max_iter=30 opt_iter=15 stop_iter=10 print_flag=3
scan var=voltage_1 value_to=-1.3 print_step=1.3 &&
   init_step=0.2 min_step=1.e-5 max_step=0.5
$
scan var=current_1 &&
   value_to=0.05E-02 print_step=0.05E-02 &&
   init_step=0.025E-03 min_step=0.05E-06 &&
   max_step=0.05E-03
$
scan3d current_from=0.0005 current_to=0.01    &&
   3d_points=20
$photon_scan=0.15
$
end
$ Longitudinal mode session:
begin_zsol
longitudinal ref_wavel=1.53d-06 &&
   left_f_refl=0.30 &&
   right_f_refl=0.30
include file=new.vcsel
mode_srch iter_num=20 &&
   wavel_xrange=[1.3E-06 1.8E-06]
bias3d step_num=20
end_zsol
```

**.rtgain 檔**

```
$file:new.rtgain
$====Round trip gain plot for VCSEL====
begin_rtgain
plot_rtgain rtgain_data=new.rtd standing_wave=new.stw &&
   plot_device=postscript
end_rtgain
```

**.plt 檔**

```
$file:vcsel.plt
$===standard plotting for VCSEL====
begin_pstprc
3dplot_data plot_device=postscript
3dget_data    main_input=new.sol    sol_inf=new.out &&
   3ddata_set=20
$ Plot at xy cross sections first
lplot_xy variable=band xy_from=(0.5 2.7)    xy_to=(0.5 3.35)
lplot_xy variable=hole_conc xy_from=(0.5 0.0)    xy_to=(0.5 6.9)
lplot_xy variable=elec_conc xy_from=(0.5 0.0)    xy_to=(0.5 6.9)
lplot_xy variable=potential xy_from=(0.5 0.0)    xy_to=(0.5 6.9)
lplot_xy variable=wave_intensity xy_from=(0.5 0.0)    xy_to=(0.5 6.9)
lplot_xy variable=local_gain xy_from=(0.5 0.0)    xy_to=(0.5 6.9)
lplot_xy variable=recomb_st xy_from=(0.5 0.0)    xy_to=(0.5 6.9)
lplot_xy variable=recomb_rad xy_from=(0.5 0.0)    xy_to=(0.5 6.9)
lplot_xy variable=recomb_aug xy_from=(0.5 0.0)    xy_to=(0.5 6.9)
lplot_xy variable=recomb_srh xy_from=(0.5 0.0)    xy_to=(0.5 6.9)
vplot_xy variable=total_curr grid_sizes=(35, 35) &&
   xrange=(0. 7.5) yrange=(0.0 6.9) &&
   point_ll=[0. 0.] point_ur=[7.5 6.9]
cplot_xy variable=wave_intensity grid_sizes=(35, 35) &&
   xrange=(0. 7.5) yrange=(0.0 6.9)
splot_xy variable=elec_conc grid_sizes=(35, 35) &&
  xrange=(0. 7.5) yrange=(0.0 6.9) view_xrot=-20 view_zrot=20
splot_xy variable=hole_conc grid_sizes=(35, 35) &&
```

```
   xrange=(0. 7.5) yrange=(0.0 6.9) view_xrot=-20 view_zrot=20
splot_xy variable=potential grid_sizes=(35, 35) &&
   xrange=(0. 7.5) yrange=(0.0 6.9) view_xrot=-20 view_zrot=20
splot_xy variable=donor_conc grid_sizes=(35, 35) &&
   xrange=(0. 7.5) yrange=(0.0 6.9) view_xrot=-20 view_zrot=20
splot_xy variable=acceptor_conc grid_sizes=(35, 35) &&
   xrange=(0. 7.5) yrange=(0.0 6.9) view_xrot=-20 view_zrot=20
splot_xy variable=wave_intensity grid_sizes=(35, 35) &&
   xrange=(0. 7.5) yrange=(0.0 6.9) view_xrot=-20 view_zrot=20
splot_xy variable=local_gain grid_sizes=(35, 35) &&
   xrange=(0. 7.5) yrange=(0.0 6.9) view_xrot=-20 view_zrot=20
$
end_pstprc
$
begin_zplot
$
plot_bias variable=delta_freq        data_file=delta_freq.txt
plot_bias variable=power_right       data_file=power_right.txt
plot_bias variable=sms_ratio      data_file=sms_ratio.txt
plot_bias variable=linewidth_spon &&
   data_file=linewidth_spon.txt
plot_bias variable=linewidth_carrier &&
   data_file=linewidth_carrier.txt
plot_bias variable=linewidth_cross &&
   data_file=linewidth_cross .txt
plot_bias variable=linewidth_sidemode &&
   data_file=linewidth_sidemode.txt
plot_bias variable=linewidth_total &&
   data_file=linewidth_total.txt
plot_bias variable=effective_alpha        data_file=effective_alpha.txt
plot_bias variable=power_right_1      data_file=power_right_1.txt
plot_bias variable=power_right_2      data_file=power_right_2.txt
plot_bias variable=sms_ratio      data_file=sms_ratio.txt
$ The delta_density here is the averaged elec. conc.
$      over the active region.
```

```
plot_z variable=delta_density data_set=20      data_file=delta_density.txt
plot_z variable=right_wave data_set=20      data_file=right_wave.txt
plot_z variable=left_wave data_set=20      data_file=left_wave.txt
plot_z variable=total_wave data_set=20 &&
   data_file=total_wave.txt
plot_z variable=sm_right_wave data_set=20 &&
   data_file=sm_right_wave.txt
plot_z variable=sm_left_wave data_set=20 &&
       data_file=sm_left_wave.txt
plot_z variable=sm_total_wave data_set=20 &&
         data_file=sm_total_wave.txt
plot_z var_num=2 2_variables=(right_wave left_wave) &&
   data_file=(right_wave left_wave).txt
plot_z var_num=2 2_variables=(sm_right_wave sm_left_wave) &&
     data_file=(sm_right_wave sm_left_wave)
plot_spec variable=mode_spectrum data_set=20 &&
     data_file=mode_spectrum.txt
plot_spec variable=mode_spectrum data_set=20 &&
   data_file=mode_spectrum.txt
end_zplot
```

# Appendix C. Publication List

1. Yen-Kuang Kuo and **Yi-An Chang**, 2002, "Numerical Study of Passive Q switching of a Tm:YAG Laser with a Ho:YLF Solid-state Saturable Absorber," Applied Optics, Vol. 42, pp. 1685-1691. (SCI)
2. Yen-Kuang Kuo and **Yi-An Chang**, 2003, "Effects of Electronic Current Overflow and Inhomogeneous Hole Distribution on InGaN Quantum-Well Laser Performance," 投稿至 IEEE Journal of Quantum Electronics. (SCI)
3. **Yi-An Chang** and Yen-Kuang Kuo, 2003, "Numerical Study on Electronic Current Overflow in 405-nm InGaN Laser Diodes," 即將投稿至 Japanese Journal of Applied Physics. (SCI)
4. Yen-Kuang Kuo, Jih-Yuan Chang, and **Yi-An Chang**, 2003, "Numerical Simulation of Tunable Cr:YSO Q-Switched Cr:LiCAF Laser," 即將投稿至 IEEE Journal of Quantum Electronics. (SCI)
5. Yen-Kuang Kuo and **Yi-An Chang**, 2003, "Numerical Study of Passive Q switching of a Tm:YAG laser with a Ho:$CaF_2$ Solid-state Saturable Absorber," 即將投稿至 Optical Engineering. (SCI)
6. **Yi-An Chang** and Yen-Kuang Kuo, 2003, "Numerical Study of Passive Q switching of a Tm:YAG laser with a Ho:$YVO_4$ Solid-state Saturable Absorber," 即將投稿至 Optics Communications. (SCI)
7. **Yi-An Chang** and Yen-Kuang Kuo, 2002, "Optical Performance of Ho:YLF Q-switched Tm:YAG Laser System," SPIE Proceedings, Vol. 4914, pp. 122 (High-Power Lasers and Applications), October 2002. (EI)
8. Yen-Kuang Kuo, Kuo-Kai Horng, Hsu-Ching Huang, Ya-Lien Huang, Jih-Yuan Chang, Yuni Chang, Wen-Wei Lin, **Yi-An Chang**, and Chih-Kang Chang, 2000, "Numerical Study on III-N and III-P Semiconductor Materials with LASTIP, PICS3D, and CASTEP," in the 2nd International Photonics Conference (IPC2000, National Chiao Tung University, Hsinchu, Taiwan), paper W-S1-A003, Proc. IPC 2000, pp. 17-19.
9. **Yi-An Chang**, Jih-Yuan Chang, Yen-Kuang Kuo, Jiann Lin, and Chung-I Chiang, 2001, "Optical Properties of InGaN Multi-Quantum Well Structures - Experimental Measurement and Numerical Simulation," 2001 年中華民國物理年會, paper PE14.
10. **張詒安**、黃雅蓮、郭艷光, 2001, "黃綠光磷化鋁鎵銦面射型半導體雷射之模擬分析," 2001 年台灣光電科技研討會, paper FA2-8.
11. 張志康、**張詒安**、郭艷光, 2001, "光纖通訊用 1.3-μm 面射型半導體雷射之模擬分析," 2001 年台灣光電科技研討會, paper P29.

12. **Yi-An Chang** and Yen-Kuang Kuo, 2002, "Design and Characterization of a 1.55-μm $In_{0.76}Ga_{0.24}As_{0.82}P_{0.18}/In_{0.48}Ga_{0.52}As_{0.82}P_{0.18}$ Vertical-Cavity Surface-Emitting Laser," 2002 年中華民國物理年會, paper E-069.
13. **張詒安**、陳秀芬、謝尚衛、吳佩璇、蔡孟倫、張誌原、郭艷光、劉柏挺, "415 nm 紫光氮化銦鎵量子井雷射電子溢流特性之探討," 2002 年台灣光電科技研討會.
14. **張詒安**、吳佩璇、吳育驊、屠嫚琳、郭艷光、劉柏挺, 2002, "使用 Dy:$CaF_2$ 被動 Q 開關於紅寶石雷射之模擬分析," 2002 年台灣光電科技研討會.
15. 楊勝州、**張詒安**、顏勝宏、黃詩瑋、蔡孟倫、劉冠良、陳俊榮、林漢威、何依萍、郭艷光, 2002, "紫光氮化銦鎵面射型半導體雷射之設計與分析," 2002 年台灣光電科技研討會.
16. **張詒安**、張志康、郭艷光, 2002, "使用可飽和吸收體 Ho:$YVO_4$ 於 2-μm Tm:$Y_3Al_5O_{12}$ 雷射系統的性能分析," 2002 年台灣光電科技研討會.
17. Pei-Hsuan Wu、**Yi-An Chang**、Yen-Kuang Kuo, 2003, "Optical Performance of Cr:YSO and Dy:$CaF_2$ Q-switched Ruby Laser Systems," 2003 年中華民國物理年會.
18. Hsiu-Fen Chen、Shang-Wei Hsieh、**Yi-An Chang**、Yen-Kuang Kuo、Man-Fang Huang、Hwei-Heng Wang、Pin-Hwei Liu, "Experimental and Numerical Investigation of 590-nm AlGaInP Light Emitting Liodes and Vertical-cavity Surface-emitting Lasers," 2003 年中華民國物理年會.
19. Meng-Lun Tsai、Sheng-Joue Young、**Yi-An Chang**、Sheng-Horng Yen、Shih-Wei Huang、Yen-Kuang Kuo, "Numerical Study of Violet InGaN Vertical-cavity Surface-emitting Laser," 2003 年中華民國物理年會.
20. Shang-Wei Hsieh、Hsiu-Fen Chen、**Yi-An Chang**、Yen-Kuang Kuo, "Numerical Study of Cr:LiSAF Passive Q-switching with a Cr:YSO Solid-state Saturable Absorber," 2003 年中華民國物理年會.